2018

Two-Electrode Measurements Of Electrostatic Double Layer Potentials With Atomic Force Microscopy

Jason Giamberardino
University of South Carolina

Two-Electrode Measurements Of Electrostatic Double Layer Potentials With Atomic Force Microscopy

by

Jason Giamberardino

Bachelor of Science
University of South Carolina 2010

Master of Science
University of South Carolina 2016

Submitted in Partial Fulfillment of the Requirements

for the Degree of Doctor Of Philosophy in

Physics

College of Arts and Sciences

University of South Carolina

2018

Accepted by:

Scott Crittenden, Major Professor

Brett Altschul, Committee Member

Thomas Crawford, Committee Member

Jamie Lead, Committee Member

Cheryl L. Addy, Vice Provost and Dean of the Graduate School

Dedication

To my mom, who never gave up and always stood by me.

Acknowledgments

I would like to take this opportunity to thank those who made this accomplishment possible.

First and foremost, thank you to my wife, Lauren, for all of the sacrifices you made in the name of my academic pursuits. Neither you nor I could have foreseen what lay ahead when we met in my first year of graduate school. Nonetheless, through seemingly countless trials and tribulations, you stuck by my side and had faith. You were solid when I needed support and delicate when I needed comforting. Thank you and I love you.

Thank you to my parents, who taught me the value of knowledge, inquisition, and hard work. I know it wasn't always the easiest thing to do, but you somehow always found a way to give me another chance and continued to support me.

Also, I owe a great deal to my two brothers, Charles and Keith. You two showed me how to be a man and more importantly a decent person, not just by telling me, but through example. Charles, your curiosity and work ethic helped guide my approach to science and life in general. Keith, your determination and spirit have always inspired me to remain positive and focused even in difficult times.

Finally, thank you to my advisor, Scott Crittenden, for having a great deal of patience and for teaching me how to properly do science.

Abstract

In this dissertation, I provide a thorough description of my development of theoretical, analytical, and experimental techniques pertaining to novel measurements of the electrostatic double layer (EDL) using atomic force microscopy (AFM), among other techniques. The EDL refers to the structure formed by ions that exists at the interface between a solid and a liquid. The EDL is an important physical element of many systems and its behavior has been of interest to scientists for many decades. Because many areas of science and engineering are moving to test, build, and understand systems at smaller and smaller scales, this work focuses on nanoscopic experimental investigations of the EDL. In that vein, AFM will be introduced and discussed as a tool for making high spatial resolution measurements of the solid-liquid interface, culminating in a description of the development of a method for completely characterizing the EDL using direct force measurements with AFM.

I first explore, in a historical fashion, the development of the various models and theories that are used to describe the electrostatic double layer. Later, various experimental techniques and ideas are addressed as ways to make measurements of interesting characteristics of the EDL. Finally, I will introduce a newly developed approach to measuring the EDL system with AFM. Using this approach, AFM measurements were made of the diffuse double layer potentials using a two-electrode system consisting of a metal coated atomic force microscopy cantilever and a metal substrate.

The variation in the diffuse layer potential was measured as a function of probe-sample potential difference, ΔV. From these measurements, values of the bulk solu-

tion potential were inferred using a model of two capacitive elements in series. The expected variation of diffuse layer potential was obtained for a model of the bulk solution potential varying linearly with ΔV in 0.1 mM, 0.5 mM, and 1 mM solutions of NaCl. It was found that the diffuse layer potentials varied roughly linearly with applied sample bias up to 100 mV. The values of the diffuse layer potentials varied from -46 mV to -11 mV, -89 mV to -8 mV, and from -71 mV to -13 mV for the 0.1 mM, 0.5 mM, and 1 mM solutions, respectively, for applied biases ranging from 0 to +400 mV. The results suggest that measurements of electrostatic double layer potentials can be made with atomic force microscopy without the need for a reference electrode.

Specifically, I show that AFM can be used to measure the two most commonly referenced potential drops in a solid-liquid interface system, referred to as the diffuse layer potential and the Stern potential. Also, in concert with the aforementioned model, the potential of the solution itself with respect to an external measurement point can be calculated. Experimental data validates the implementation of such a model and, together, the results indicate that AFM can be used to fully characterize the electrostatic environment of certain solid-liquid interface systems.

Table of Contents

Dedication iii

Acknowledgments iv

Abstract v

List of Figures x

List of Symbols xvi

List of Abbreviations xviii

Chapter 1 Introduction 1

Chapter 2 Models of the EDL 4

2.1 Helmholtz Model 5

2.2 Gouy-Chapman Model 7

2.3 Stern's Modification of the Gouy-Chapman Model 15

2.4 Grahame's Contribution 18

2.5 Further Refinement of Models 20

2.6 Forces Due to Double Layer Interactions: DLVO Theory 20

Chapter 3 Atomic Force Microscopy 22

3.1 How AFM Works 23

3.2 Operational Modes Of AFM 26

Chapter 4 Previous Nanoscopic Measurements of the EDL . . . 36

4.1 Executive Summary 36

4.2 Unique Methods For Making In-Liquid Electrical Measurements With AFM 39

4.3 The Surface Force Apparatus 42

4.4 Measuring Double Layer Forces with AFM 43

4.5 Measuring Interfacial Electrostatics of Specific Systems 47

4.6 Measuring In-Solution Potentials as a Function of Sample Biasing . . 49

4.7 Cyclic Voltammetry / Electrochemistry 54

Chapter 5 Measurements of the Stern and Bulk Potentials of Metal-Electrolyte Interfaces 56

5.1 A New Nomenclature for Solid-Liquid Interface Systems 56

5.2 Capacitive Description of the EDL 63

5.3 The Force Due to Double Layer Interactions 67

5.4 Measuring Diffuse Layer Potential Drops With AFM: Probe Calibration 68

5.5 Assumptions of the Model 70

5.6 Measurement Simulation: Error Analysis and Propagation 74

5.7 Reproducing Previous Results 77

5.8 Two-Electrode Measurements of EDL Potentials with AFM 85

Chapter 6 Conclusions / Future Work 91

6.1 Conclusions 91

6.2 Future Work 93

Bibliography 96

Glossary of Terms 103

List of Figures

Figure 2.1 The (a) charge and (b) potential distributions according to the Helmholtz theory. The two conductors develop equal and opposite surface charges, akin to a capacitor. Here, the charges are represented by black and white circles. The potential in this model is a linear function of the separation the conductors, represented here by the value of z. 7

Figure 2.2 The (a) charge and (b) potential distributions in the 1-D Gouy-Chapman model. The charges (filled circles) within the solid metal (gray) surface in (a) are bound to their lattice sites, while those in solution (filled and open circles) are free to form the exponentially decaying distribution proposed by the model. This charge distribution leads to the potential distribution in (b) which drops exponentially from the solid surface. The potential has a finite maximum value, $\phi_{surface}$, at the surface. The exponential decay of the potential is describe by the Debye length, λ. 11

Figure 2.3 Dependence of the spatial potential distribution on the valency of the salt present in solution. (a) Shows the potential profile of multiple valency salts present at 1 mM concentration while (b) shows the profile for the same valency salts at a 10 mM concentration. The concentration and valency have noticeable effects on the magnitude of potential drop through the parameter κ, whereas the temperature has little or no effect on the shape of the potential plot. 12

Figure 2.4 The temperature dependence of the potential distribution for (a) 1 mM 1:1 salts, (b) 10 mM 1:1 salts, (c) 1 mM 1:2 salts and (d) 10 mM 1:2 salts. 12

Figure 2.5 Dependence of the spatial potential distribution on the dielectric constant of the supporting medium. Each of the plots represent solutions of different valency salts at different concentrations. (a) and (b) show the values for 1 mM and 10 mM 1:1 salts, respectively and (c) and (d) show values for a 1 mM and 10 mM 1:2 salt, respectively. The dielectric constant of water used in most applications of theory is $\sim$ 80. Measurements suggest, however, that a value of $\epsilon \sim 10$ is more accurate[23]. . . . 13

Figure 2.6 Schematic representation of the charge and potential distribution according the Gouy-Chapman-Stern model. The charge (negative in this example) on the metal surface (dashes) attracts counterions in solution (large circles). The distance of closest approach of the counterions is defined by the Outer Helmholtz Plane (OHP). The location of the OHP, in turn, is dependent on the radius of the counterions and the solvent molecules (small circles). The potential drops linearly through the Stern layer out to the OHP and then exponentially through the diffuse layer to the bulk value. The Inner Helmholtz Plane (IHP) is not considered in this potential profile. 19

Figure 3.1 Schematic of a typical AFM system. The cantilever/tip system is brought near a sample and its three-dimensional movement is monitored via a laser beam that is reflected off the back surface of the cantilever. The reflected beam is collected at a quad-segment photodetector and a computer controlled feedback system is used to adjust the position of the sample according to various feedback input parameters defined by the user. 23

Figure 3.2 Schematic of a typical AFM cantilever on a larger silicon chip. Image courtesy of Budget Sensors ®. 24

Figure 3.3 The standard model for the AFM cantilever/tip system. The cantilever is a flat beam of length L, width w (not represented), and thickness t. The tip is composed of a truncated cone, with characteristic height, H, and angle θ with a sphere of radius R embedded at the end. 25

Figure 3.4 Block diagram of a PID feedback loop. A desired state is input by the user. The difference between that set point and the current state of the system (error) is calculated and used as the input for the PID network. The output is a control sequence which gives the system some instruction as to how to change its state. The process is then repeated continuously. 27

Figure 3.5 A representative force-distance curve measured in ambient laboratory conditions. The dashed line is the approach curve and the full line is the withdrawal curve. The cantilever begins far from the surface at zero deflection (A). As it approaches and the force gradient becomes larger than the spring constant, instantaneous jump to contact occurs (B). The sample and cantilever/tip are in contact and move in unison (B-D). The tip is withdrawn from the surface and eventually the adhesive forces are overcome and the tip and sample separate (E). 29

Figure 3.6 A typical force curve measured for a silica colloidal probe and a silicon sample surface in a 1 mM NaCl solution. Note the exponentially decaying force due to screening effects. Also, a jump-to-contact can be seen around 5 nm of probe-sample separation. This is not a constant feature of force curves in liquid and often the electrostatic and other repulsive forces are enough to negate any attraction due to van der Waals forces and eliminate any jump to contact. 31

Figure 3.7 A characteristic "V Curve" showing the minimum in the oscillation amplitude, shown here as CH8, at ω due to the applied potential. The minimum occurs at an applied DC potential equal to the contact potential difference between the tip and the surface. 34

Figure 5.1 Potential level diagrams for the (a) Gouy-Chapman and (b) Gouy-Chapman-Stern models. The V's represent potentials measured with respect to the external machine ground and the ϕ's represent differences between the V's. Either ϕ_{ssb} or ϕ_{psb} are what are measured in a typical force experiment. 61

Figure 5.2 Schematic of the two capacitors in series model of the EDL system. C_{st} and C_d represent the capacitance of the Stern and diffuse parts of the EDL, respectively. ϕ_{sss} and ϕ_{ssb} are the potential drops across the Stern and diffuse layers, respectively. The physical solid-liquid interface does not contain two separate capacitive elements. All of the charge exists, instead, within the diffuse layer beginning at the OHP. 64

Figure 5.3 Relationship between the potential drops across the diffuse and Stern layers according to (5.10). The different curves represent (5.10) evaluated for various solution concentrations. The dependence of the potential drop across the Stern layer on the diffuse layer potential drop increases with increasing solution concentration. 67

Figure 5.4 The potential profile for the symmetric electrode case. The drops across each region are the same in magnitude on either solid-liquid interface. The initial, linear potential drop from the probe surface represents ϕ_{pps} and that from the sample surface represents ϕ_{sss}. The exponential drops that occur thereafter represent ϕ_{psb} and ϕ_{ssb}. 70

Figure 5.5 Cyclic Voltammograms of (a) 0.1 mM NaCl and (b) 1 mM NaCl solutions. The data indicate that no chemical reactions are being induced, and hence there are no Faradaic currents in the applied bias range of $0 - 400$ mV 72

Figure 5.6 A selection of simulated force measurements with increasing amounts of Gaussian noise added to the system. Each simulation has noise added to both the probe-sample distance, z, and the force, F. The red lines represent fits to the simulated data (blue circles) to (5.14) with the fitting algorithm used for real experimental data. The black dashed line represents function used to generate the noisy data. The fits yielded R^2 values of (from left to right) 0.974, 0.972, 0.864, 0.680 76

Figure 5.7 Results of performing fits for the value of ϕ with varying noise levels in z and F. During the simulations, the potential, ϕ was set to 50 mV. The data indicates that, as expected, the fitting algorithm tightly constrains the value of ϕ for low levels of noise. As the noise level increases in either z or F, the error in the fitting increases. The algorithm appears more sensitive to F than z. The black lines indicate the standard error of the mean for fitted values of ϕ over 100 trials. 78

Figure 5.8 (a) Topographic image obtained by scanning a TGT1 grating with a colloidal probe. The height profile seen in (b) is obtained by plotting the points that lie along the green line in (a). The data from the profile is used to calibrate the radius of the spherical probe via (5.17). 80

Figure 5.9 A photo of a typical AFM experiment within a liquid environment. The water meniscus can be seen clearly. This meniscus begins from below at the sample surface and terminates above on the holder in which the cantilever/probe rests. Typical measurements are made in approximately 100 μL of solution. The small amount of liquid compared to similar larger scale measurements demands that consideration must be given to the effects of electrical biasing on the liquid itself. 81

Figure 5.10 Measured diffuse layer potential drops for a gold surface in 1 mM KNO_3. The measurements were made using a silica probe and a platinum reference/counter electrode. The diffuse layer potential of the silica probe was assumed to be -45 mV[29]. These results demonstrate that our measurement system and analysis of the forces yield results that are consistent in the nature of the response of the system with those in literature[6]. . 82

Figure 5.11 Calculated values of diffuse layer potential drops for a system consisting of a gold sample, an electrically isolated gold probe, and a platinum reference electrode in 1 mM NaCl over a range of applied sample biases. The underlying force data was analyzed under the assumption that (a) the bulk potential remains constant throughout the measurement and (b) the bulk potential is some constant offset plus $\Delta V/2$. The model of a constant bulk potential yields values of the diffuse layer potential drop that are independent of the applied bias. All previous work in the field indicates that this is not a reasonable result. The model of a shifting bulk potential yields the expected linear response of the diffuse layer potential drop to the applied bias up to ΔV = 100 mV, after which some saturation occurs. Saturation of this type has been observed in similar systems[3, 12, 25]. 84

Figure 5.12 Force versus probe-sample separation curves for a gold probe and gold sample in 0.1 mM NaCl at various applied sample biases. There is a clear dependence of the force on the applied bias potential. Only every sixth data point is shown for clarity. . 86

Figure 5.13 Calculated values of diffuse layer potential drops for a system consisting of a gold sample and gold probe in (a) 0.1 mM and (b) 0.5 mM and (c) 1 mM NaCl over a range of applied sample biases. The bias is applied directly between the sample and probe. Diffuse layer potential drops were calculated assuming the bulk potential is $V_b = V_0 + \Delta V/2$, yielding the expected linear response of the diffuse layer potential drop to the applied bias for $\Delta V < 100$ mV. 87

Figure 5.14 Calculated values of the potential drop across the Stern layer of the sample surface, ϕ_{sss}, assuming a shifting bulk potential. The values of the Stern potential are higher for the higher concentration, consistent with the notion of a more completely filled Stern layer. 88

Figure 5.15 Calculated values for values of V_i, the potentials as measured from power supply ground. (a) shows each potential for the 0.1 mM NaCl solution. The list of potentials shown includes V_s, the sample potential, V_{ss}, the potential at the OHP of the sample, V_{bs}, the bulk potential as measured from the sample, V_{bp}, the bulk potential as measured from the probe, V_{ps}, the potential at the OHP of the probe, and V_p, the potential of the probe. The potentials are represented by open squares, filled circles, upright triangles, open diamonds, open circles, and inverted triangles, respectively. The inset of (a) shows the values of V_{bp} (open diamonds) and V_{bs} (upright triangles). (b) and (c) depict only the bulk potentials as measured from each electrode for the 0.5 mM and 1 mM solutions, respectively. 90

Figure 6.1 Sample design to be used in the (a) unbiased and (b) biased measurements. The part of the sample marked "C" is the same material as the probe and is used for calibration. The area marked "I" in the second design is an insulating layer and "S" represents the sample surface that will be external biased and subsequently measured. 94

List of Symbols

c_0	Initial solution ionic concentration
$\mathcal{C}$	Capacitance (F)
C_d	Areal capacitance of the diffuse layer (F/m^2)
$\mathcal{C}_D$	Differential capacitance
C_D	Differential areal capacitance
C_{st}	Areal capacitance of the Stern layer
d_{st}	Thickness of the Stern layer
e	Elementary charge
ϵ	Dielectric constant of the bulk liquid medium
ϵ_0	Permittivity of free space
ϵ_{st}	Dielectric constant of the Stern layer
F	Force between AFM probe and sample
k	Boltzmann's constant
κ	Inverse Debye screening length
λ	Debye screening length
ϕ_{pb}	Total in-solution potential drop from probe to bulk solution
ϕ_{pps}	Potential drop across the probe Stern layer
ϕ_{psb}	Potential drop across the diffuse layer of the probe
ϕ_{sb}	Total in-solution potential drop from sample to bulk solution
ϕ_{ssb}	Potential drop across the diffuse layer of the sample
ϕ_{sss}	Potential drop across the sample Stern layer
R	AFM probe radius
$\mathcal{R}$	Ideal gas constant

σ	Areal surface charge density
V_0	Component of the bulk solution potential resulting from an offset potential between machine ground and the bulk solution
ΔV	Potential difference applied between the probe and sample
V_b	Machine ground-referenced potential of the bulk solution
V_{bp}	Machine ground-referenced potential of the bulk solution as measured from the probe
V_p	Machine ground-referenced potential of the probe
V_{ps}	Machine ground-referenced potential at the Outer Helmholtz Plane of the probe
V_s	Machine ground-referenced potential of the sample
V_{ss}	Machine ground-referenced potential at the Outer Helmholtz Plane of the sample
V_q	Component of the bulk solution potential resulting from charge transfer across the interface from the electrode to the solution
T	Temperature in Kelvin
Z_i	Ion valency
z	Spatial separation of AFM probe and sample

List of Abbreviations

AFM	Atomic Force Microscopy
AM-AFM	Amplitude Modulation Atomic Force Microscopy
CV	Cyclic Voltammetry
ECSFA	Electrochemical Surface Force Apparatus
EDL	Electrostatic Double Layer
EFM	Electrostatic Force Microscopy
FM-AFM	Frequency Modulation Atomic Force Microscopy
G-C	Gouy-Chapman
G-C-S	Gouy-Chapman-Stern
IEP	Isoelectric Point
IHP	Inner Helmholtz Plane
KCl	Potassium Chloride
KFM	Kelvin Force Microscopy
KNO_3	Potassium Nitrate
KPM	Kelvin Probe Microscopy (equivalent to KFM)
LIA	Lock-In Amplifier
NaCl	Sodium Chloride
OHP	Outer Helmholtz Plane
PID	Proportional Integral Derivative
PZC	Potential of Zero Charge
PZF	Potential of Zero Force
SFA	Surface Force Apparatus

Chapter 1

Introduction

Whenever a solid object is placed into a solution containing ions, charge accumulation can occur at the solid-liquid interface. An initially charged object in any medium will attract opposite (counter) charges from any nearby sources. In the case of an electrode in solution, the source of the counter charges will come from any dissolved ions or from the solvent molecules themselves. The charges can be cations or anions from the electrolytic species present as well or, in the case of an aqueous solution, positively charged hydronium or negatively charged hydroxide molecules.

Even if the solid is initially uncharged, a net charge will develop on its surface and the charge migration is thus initiated. A net charge can develop on such a neutral surface via a variety of physiochemical processes. Two dominant sources of charging are surface group ionization or dissociation (i.e., $\mathrm{COOH} \rightarrow \mathrm{COO}^- + H^+$) and entropic forces that result from the asymmetry created by the interface versus an infinite solution environment and drive ions toward the solid surface. No matter how the surface charge develops, what is important is the fact that the surface, now charged, will attract counter charges from solution and the region of space immediately surrounding the solid-liquid interface becomes filled with charges. This distribution of charges and counter charges at the interface are what form the EDL.

How the charges are distributed and what sort of electrostatic environment they create is a relevant question in many fields of science such as biology, biochemistry, soil sciences, mineralogy, chemistry, and solid state physics. This is because the presence of the EDL is what mediates all interactions that take place in liquid environments

of any kind. Whether it be colloids in a dispersion, cells in vivo, electrodes in a liquid cell battery, or any other system in which a solid-liquid interface is present, the EDL is present and plays a role in determining things like reaction rates, biological compatibility, or colloidal stability. Many models have been developed in the last 150 years to describe the electrostatic characteristics of the solid-liquid interface. Following the trend of much of modern science, the current goal of many researchers in the field is to probe the interface at smaller and smaller length scales.

My research has focused on utilizing AFM to investigate the solid-liquid interface. Within that context, I have focused on attempting to characterize the EDL that forms at the interface in terms of the electrostatic potentials that develop within certain spatial regimes. In Chapter 2, the development of the most widely accepted models of the EDL will be presented and discussed in chronological fashion. It is important to understand this developmental process as it gives a firm footing from which further development of new models and experimental techniques that rely on such models for the interpretation of experimental data can be built.

As the majority of my work has utilized AFM as the measurement system of choice, Chapter 3 delves into the full operational specifics of AFM, its capabilities, limitations, and its utility for nanoscale measurements of the EDL. Understanding how the instrument works and how it measures what it measures will provide a better foundation onto which the ideas presented in both Chapters 4 and 5 can be built. Chapter 4 presents a short literature review of some of the recent scientific developments in regard to measuring the characteristics of the EDL. This places the new research of this work in context and serves to introduce some terms and basic ideas for these types of measurements. The review will focus mostly on experiments in which AFM was the prevalent technique, but will not be limited to such cases.

Finally, Chapter 5 will present the new research and progress I have made in the last several years as pertains to the measurements and analysis of AFM-based

measurements of the EDL, with special focus on the electrostatics of the solid-liquid interface. This will include both theoretical and experimental research outcomes. The main result of the work presented within is a measurement of a particular potential drop that occurs on the solution side of the solid-liquid interface. This parameter has thus far only been measured once with AFM and the techniques developed make its measurement much simpler and more robust. A secondary outcome of the research presented is the ability to also measure the potential of the interior or bulk of a solution with respect to an external reference point. Both of these outcomes serve as solid advancements in the nanoscopic experimental investigation of solid-liquid interface systems. According to the results presented, a first of its kind complete characterization of these systems is now possible.

Chapter 2

Models of the EDL

The development of models of the solid-liquid interface has been ongoing for over a century. Many scientists have contributed to the overall understanding of this system. A full treatment of all theories and their respective place within the larger knowledge structure is beyond the scope of this thesis. Here, instead, I will discuss a few of the major developments in the field relevant to my work in roughly chronological order.

Of course, there should be some metric by which the validity of each model can be tested. It turns out that the metric that is most often used is a quantity known as the differential capacitance, $\mathcal{C}_D$. The differential capacitance differs from the normal or integral capacitance, $\mathcal{C}$, only in that the regular capacitance is a special case of the differential capacitance. The differential capacitance is defined as the rate of change of stored charge Q divided by the rate of change in the potential difference within that system, V, such that $\mathcal{C}_D = \frac{dQ}{dV}$. This differs in definition from the normal capacitance, which is typically written $\mathcal{C} = \frac{Q}{V}$. $\mathcal{C}_D$ can be thought of as the "real" or "fundamental" capacitance. In general, Q is always a function of V. In the simplest possible case, where $Q = \mathcal{C}_0 V$, with $\mathcal{C}_0$ being some constant, $\mathcal{C}_D$ and $\mathcal{C}$ are equal. If the situation deviates even slightly from this special case, then the two functions become different. For instance, if some initial charge, Q_0 is present, such that $Q = Q_0 + \mathcal{C}_0 V$. Even if one adopts a more rigorous definition of $\mathcal{C}$, such that $\mathcal{C} = \frac{\Delta Q}{\Delta V}$, $\mathcal{C}_D$ and $\mathcal{C}$ still diverge for situations in which the stored charge is a nonlinear function of the potential difference. It is for this reason that measurements of the EDL tend to use the differential capacitance, as it is known that their behavior is not that of an ideal

parallel plate system.

2.1 Helmholtz Model

Helmholtz is often credited as being the first scientist to investigate the solid-liquid interface and propose a model for this system. In a paper in 1853, often cited as that in which the first EDL theory was proposed, Helmholtz explored the electrical nature of the interface of two different conducting materials in contact or close to contacting one another[70]. He imagined a potential difference V being applied to one of the conductors. Citing the fact that all excess charge on a conductor resides on its exterior surface, he proposed that imposing V on a conductor would lead to surface charge density on this conductor. This charge would cause counter charges from the second, initially equilibrated, conductor to migrate toward its surface. He dubbed these two sheets of charge the "electric double layer".

In Helmholtz's simplified model, a monolayer sheet of charge forms at each surface. Helmholtz did not classify this system as a "capacitor", because the term was not introduced into the physical sciences vernacular until the 1920s[1]. Today, however, the system he described is recognized as just that. Helmholtz went on to derive an expression for the charge per unit area, σ, on the conductor surface as a function of the applied potential difference, V, and the conductor separation distance, d. He found that

$$\sigma = \frac{\epsilon\epsilon_0}{d}V. \tag{2.1}$$

Here, ϵ and ϵ_0 are the dielectric constant of the medium between the charge layers and the permittivity of free space, respectively.

Viewing the entire system as a single capacitor leads to an expression for the differential capacitance (per unit area), C_D, of the system,

$$C_D = \frac{d\sigma}{dV} = \frac{\epsilon\epsilon_0}{d}. \tag{2.2}$$

Therefore, the Helmholtz model predicts a differential capacitance that does not depend on potential difference or any factors other than the separation distance and the dielectric constant of the region between the two charge-carrying materials. Helmholtz cited Gauss' result that the excess charge on a conductor will reside on its surface to derive his results and attempted to translate this result to the solid-liquid interface[70]. From the perspective of molecules on a solid conductor surface that has been immersed in a solution, however, the second conductor (the liquid) is essentially infinite in space and approaches infinitely close to the metal surface. This leads to an ambiguity of where the surface of the second conductor actually is located. Furthermore, the charges in a liquid are not bound to a particular lattice structure as they are in a metal conductor. These two discrepancies between a solid-solid and solid-liquid interface are why the predictions of the Helmholtz Model were not realized in later experiments.

One of the first researchers to put the various models, including the Helmholtz Model, of the EDL to the test experimentally was Grahame in 1947[31]. The measurements made by Grahame of the differential capacitance of NaF solutions in contact with a mercury droplet showed that it was not constant as proposed in the Helmholtz Model. Grahame showed that the differential capacitance was a function of multiple factors including ionic concentration and applied voltage. Grahame's contributions, being seminal in the field, are discussed in more detail at the end of this chapter.

The underlying failure of the Helmholtz model to describe the solid-liquid interface, again, stems from the fact that Helmholtz was not considering that specific interface, but the more general case of two conducting materials close to contact. Among other models tested by Grahame was one that could potentially account for this shortcoming in the Helmholtz model. This model was that of Gouy and Chapman.

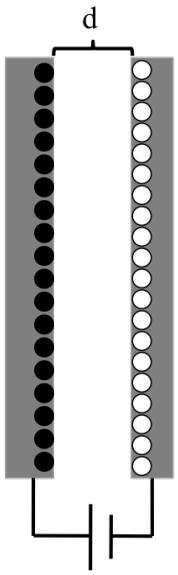

(a)

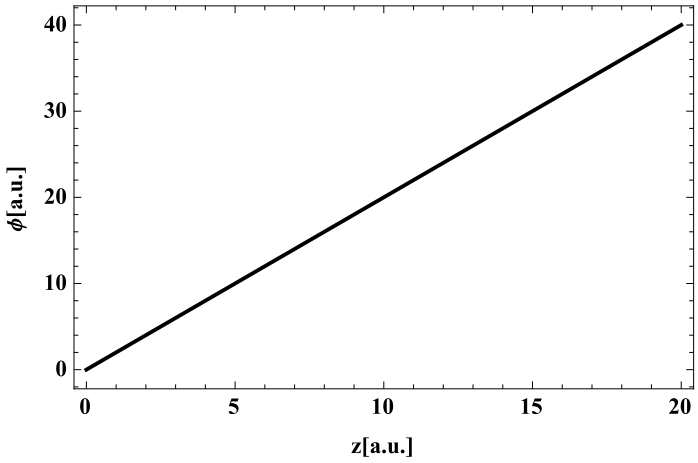

(b)

Figure 2.1: The (a) charge and (b) potential distributions according to the Helmholtz theory. The two conductors develop equal and opposite surface charges, akin to a capacitor. Here, the charges are represented by black and white circles. The potential in this model is a linear function of the separation the conductors, represented here by the value of z.

2.2 Gouy-Chapman Model

In the years between 1906 and 1915, before Grahame's experiments, Louis Georges Gouy and David Leonard Chapman independently considered the situation of a solid conductor immersed in an electrolytic solution[30, 16] and sought to build on and improve the work of Helmholtz. They both recognized that the major shortcoming of the Helmholtz model was its inability to describe the mobility of charges in the liquid phase. They both used thermodynamic techniques to solve the problem. Their approaches differed slightly, but they arrived at the same result. Since they took slightly different approaches, I present an approach that is similar to both without being exactly equal to either. The process begins by writing the Poisson equation for a general charge distribution, which is

$$\nabla^2\phi = -\frac{\rho}{\epsilon\epsilon_0}. \tag{2.3}$$

Here, ∇^2 is the Laplacian differential operator, ϕ is the electric potential difference at some point with respect to infinity in Volts, ρ is the charge distribution measured in $\frac{C}{m^3}$, ϵ is the unitless dielectric constant of the solution and ϵ_0 is the permitivitty of free space in $\frac{F}{m}$. This equation relates the charge distribution in any region of space to the electrostatic potential that generates that charge distribution or vice versa.

Gouy and Chapman realized that the thermal motion of the ions in solution would contribute a great deal to their overall energy profile. Ludwig Boltzmann had recently derived a set of statistical relations with which one could calculate the probability for a number of particles to be in a particular energy state. These relations hold true only if the temperature is high enough and/or the particle density is sufficiently low so as to neglect any quantum mechanical effects, which is generally the case for aqueous solutions at standard conditions. According to Boltzmann statistics, the concentration of any particular ionic species, i, at any point in the solution is given by

$$c_i = c_{0i} \exp\left[-\frac{W_i}{kT}\right], \tag{2.4}$$

where c_{0i} is the bulk concentration at infinity, W_i is the energy required to bring the ion in from infinity to the specified location, k is the Boltzmann constant, and T is the temperature. The work required to move a certain charge depends on its valency, denoted by Z. This value reflects the excess charge on a particular molecule or atom and is also known as the oxidation state. For example, sodium has a Z of $+1$, whereas chlorine has a Z of -1. Therefore, the work term can be rewritten as

$$W_i = eZ_i\phi, \tag{2.5}$$

where e is the elementary charge, ϕ is the scalar electric potential, and Z_i is the valency of the ion species. Therefore, the local ion density will be

$$c = \sum_i c_{0i} \exp[-\frac{eZ_i\phi}{kT}], \tag{2.6}$$

and hence the local charge density, ρ will be

$$\rho = e\sum_i c_{0i} Z_i \exp\left[-\frac{eZ_i\phi}{kT}\right]. \tag{2.7}$$

Combining (2.3) with this result yields

$$\nabla^2\phi = -\frac{e}{\epsilon\epsilon_0}\sum_i c_{0i} Z_i \exp[-\frac{eZ_i\phi}{kT}] \tag{2.8}$$

This is known as the Poisson-Boltzmann equation. It is a nonlinear second order differential equation. Equations of this type typically need to be solved numerically.

Solutions of (2.8) arise when one considers particular cases, such as different electrode geometries. Before considering any geometry, we note that we can perform a Taylor series expansion of the exponential function itself, which includes a linear term followed by higher order terms. If the argument is considered to be small, the higher order terms become insignificant. In this case, the argument begins to get "small" when the electrostatic potential energy has a value much less than the thermal energy. That is, when $eZ_i\phi \ll kT$. For standard laboratory conditions, kT is about 4×10^{-21} J or 25 mV. In fact, the model agrees with experiment for values of the electrostatic potential up to $\sim$ 100 mV[13, 39]. The procedure of expanding the exponential function and keeping only the linear term is known as the Debye-Hückel approximation or the Debye-Hückel Linearization. Doing so reduces (2.7) to

$$\rho \approx \sum_i c_{0i} Z_i\Big(1 - \frac{eZ_i\phi}{kT}\Big). \tag{2.9}$$

Plugging this result back into (2.8) leads to

$$\nabla^2\phi = -\frac{e}{\epsilon\epsilon_0}\Big(\sum_i c_{0i} Z_i - \sum_i \frac{c_{0i} eZ_i^2\phi}{kT}\Big). \tag{2.10}$$

The first term in this equation goes to zero due to the Nernst-Planck macroscopic electroneutrality principle of ionic solutions: bulk ionic solutions tend to be electrically neutral[63]. Equation (2.10) reduces to

$$\nabla^2\phi = \frac{e^2\phi}{\epsilon\epsilon_0 kT}\sum_i c_{0i} Z_i^2. \tag{2.11}$$

This is known as the linearized Poisson-Boltzmann equation or the Linear Poisson-Boltzmann equation. This reflects the fact that the full Poisson-Boltzmann equation has been linearized by expanding the exponential and only keeping the term in the expansion that is linear in the potential, ϕ. This equation, unlike the full form of (2.8), can be solved analytically for different cases. The solutions of (2.11) vary depending on the particular geometry and boundary conditions being used. Here, I will work through two such examples that are relevant to the other work discussed in this thesis.

2.2.1 The 1-D Case

It is illustrative to consider the case of a planar surface with a potential distribution in solution that is only a function of a single spatial coordinate. Since (2.11) is a second order differential equation, it will require two boundary conditions to solve. In one dimension, one guesses a solution of the form

$$\phi(z) = K_1 \exp[-\kappa z] + K_2 \exp[\kappa z], \tag{2.12}$$

where $\kappa = \sqrt{\frac{e^2}{\epsilon\epsilon_0 kT}\sum_i c_{0i} Z_i^2}$ is known as the "inverse Debye length" or the "inverse screening length". The boundary conditions are $\phi(z = 0) = \phi_0$ and $\phi(z = \infty) = 0$. The first condition is a definition of the "surface potential". This is the potential at the physical surface of the solid with respect to the bulk solution. The second boundary condition sets the potential in the bulk solution, assumed to be at an infinite distance from the surface, to be zero. Doing so sets the reference point of the potential scale for this system to a point within the bulk solution. Plugging these into (2.12) yields $K_1 = \phi_0$ and $K_2 = 0$. Therefore,

$$\phi(z) = \phi_0 \exp[-\kappa z]. \tag{2.13}$$

This leads to a differential capacitance given by

$$C_D = \left(\frac{2Z^2 e^2 \epsilon\epsilon_0 c_0}{kT}\right)^{\frac{1}{2}} \cosh\left(\frac{Ze\phi_0}{2kT}\right). \tag{2.14}$$

This is the Gouy-Chapman result for the potential at any distance z from a planar surface due to the EDL that forms at the surface. The exponentially decaying charge distribution that results from this model is often referred to as the "diffuse layer" of a double layer system. Often, the Debye length, given by $\lambda = \kappa^{-1}$, is used in place of κ. Figure 2.2b shows the charge and potential distributions that result from such a model. The differential capacitance, C_D, predicted by this model rises indefinitely with increasing potential, ϕ_0.

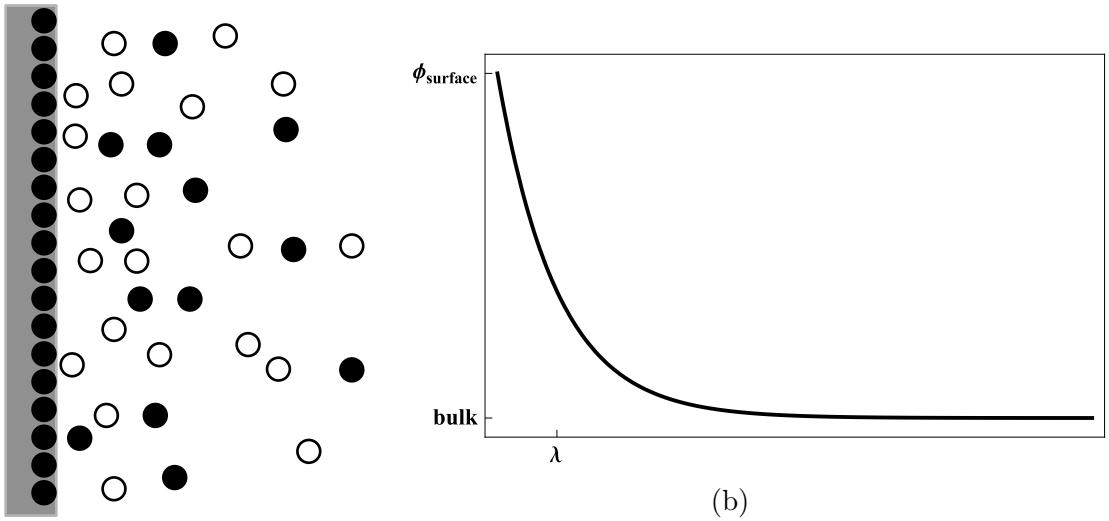

(a) (b)

Figure 2.2: The (a) charge and (b) potential distributions in the 1-D Gouy-Chapman model. The charges (filled circles) within the solid metal (gray) surface in (a) are bound to their lattice sites, while those in solution (filled and open circles) are free to form the exponentially decaying distribution proposed by the model. This charge distribution leads to the potential distribution in (b) which drops exponentially from the solid surface. The potential has a finite maximum value, $\phi_{surface}$, at the surface. The exponential decay of the potential is describe by the Debye length, λ.

Note that, through κ (or λ), the spatial potential distribution will be a function of several factors including the valency of the ionic species present, ionic concentration, ambient temperature, and the dielectric constant of the medium. Figures 2.3 through 2.5 demonstrate how these factors quantitatively affect the potential distribution.

It is obvious how some of these parameters can be changed within the course of

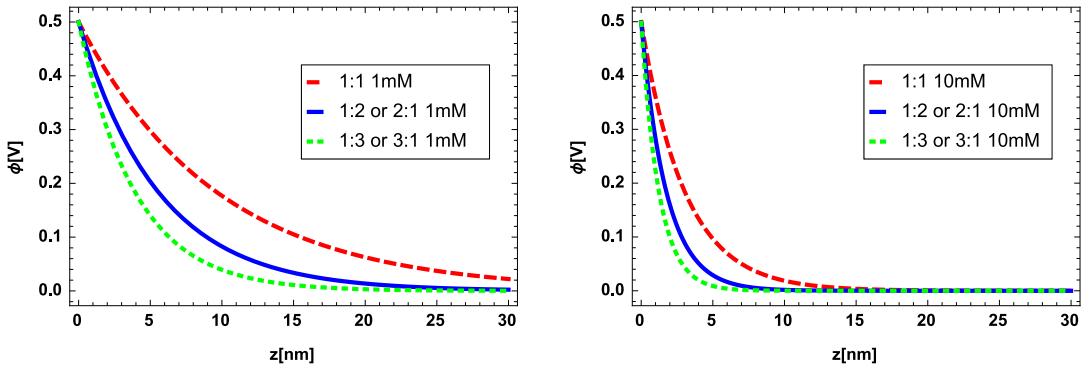

(a) (b)

Figure 2.3: Dependence of the spatial potential distribution on the valency of the salt present in solution. (a) Shows the potential profile of multiple valency salts present at 1 mM concentration while (b) shows the profile for the same valency salts at a 10 mM concentration. The concentration and valency have noticeable effects on the magnitude of potential drop through the parameter κ, whereas the temperature has little or no effect on the shape of the potential plot.

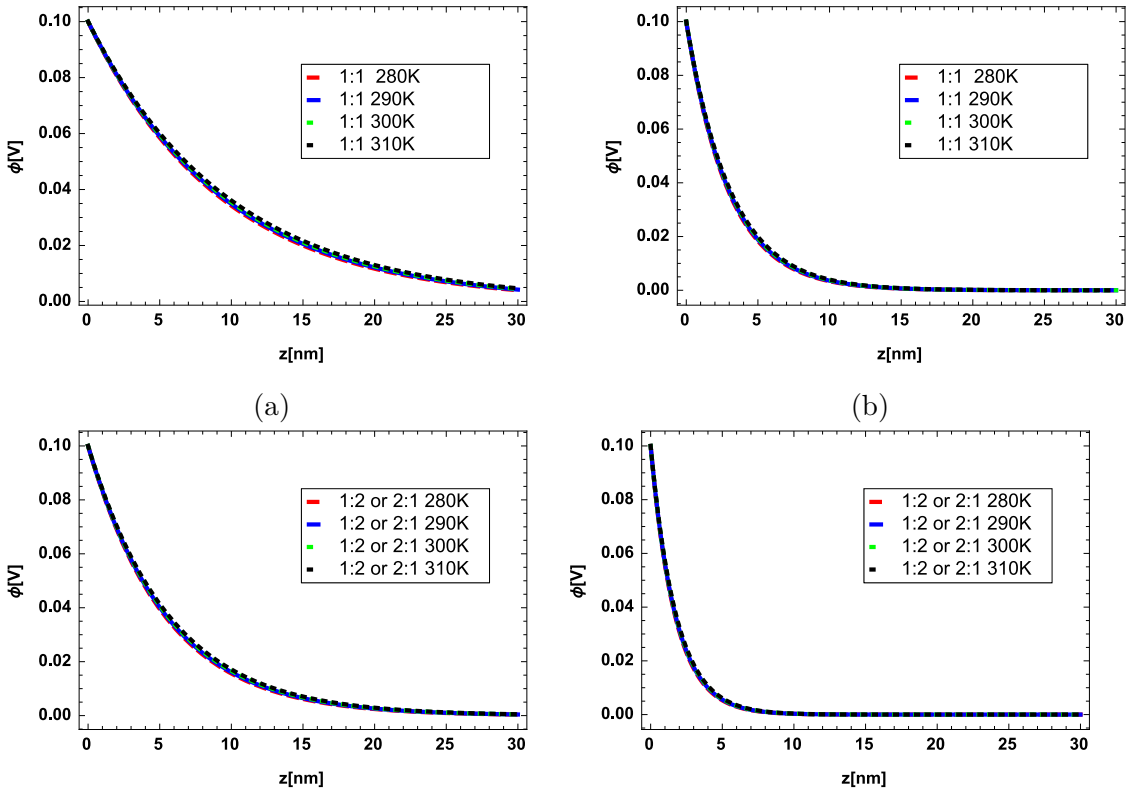

(a) (b)

(c) (d)

Figure 2.4: The temperature dependence of the potential distribution for (a) 1 mM 1:1 salts, (b) 10 mM 1:1 salts, (c) 1 mM 1:2 salts and (d) 10 mM 1:2 salts.

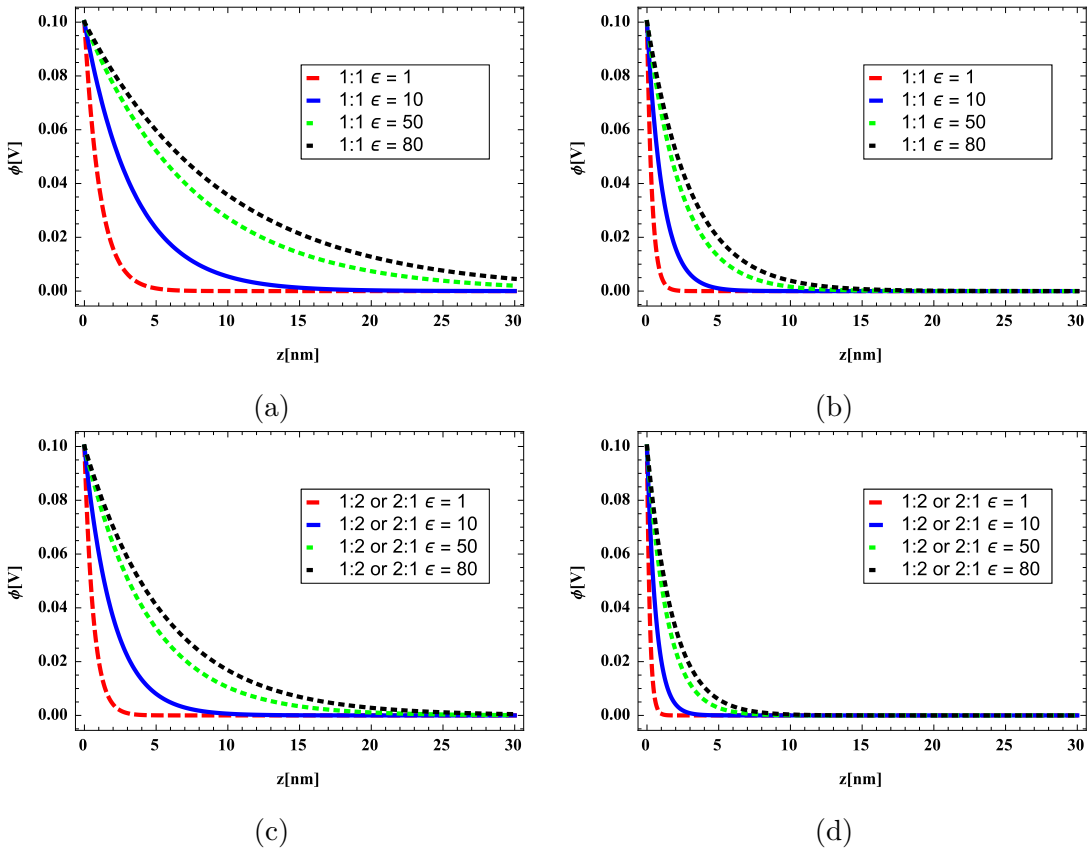

Figure 2.5: Dependence of the spatial potential distribution on the dielectric constant of the supporting medium. Each of the plots represent solutions of different valency salts at different concentrations. (a) and (b) show the values for 1 mM and 10 mM 1:1 salts, respectively and (c) and (d) show values for a 1 mM and 10 mM 1:2 salt, respectively. The dielectric constant of water used in most applications of theory is ~ 80. Measurements suggest, however, that a value of $\epsilon \sim 10$ is more accurate[23].

an experiment. For instance, the temperature can be adjusted by means of a heating element placed within the solution or simply increasing the ambient temperature. However, the dielectric constant of the solution is more complicated to understand. It's reasonable to assume that the addition of salts will affect its value, but to what extent? Experimental data and models have been combined in a number of studies to show that the addition of ions actually has little to no effect on the static dielectric constant of water for concentrations below ~ 2 M[26]. A number of reasons for the lack of effect have been proposed. For instance, Wang et al. suggest that water molecules, being very polar on their own, respond to the presence of an electric field much more

strongly and thus will dominate the overall response of the solution to an external field, even in the presence of other ionic species[71]. Another possible explanation is simply that the number of ions present at concentrations under 1 M is not enough to influence the response of an aqueous solution to an applied field, regardless of the polarizability of either type of molecule[34]. Whatever the reason, the bulk dielectric constant of aqueous electrolytic solutions under 1 M can be considered to be $\epsilon \sim 80$[26]. As will be discussed in Chapter 5, the dielectric constant of the medium at distances within a Debye length of a surface can be much different than the bulk value.

2.2.2 Potential of a Spherical Particle

In general, the 3-dimensional case is the one of most interest because it gives the most accurate representation of a real world scenario. In 3-D, the simplest surface one could imagine introducing into the theory is a spherical one. This geometry will be of particular importance in the context of future chapters.

In spherical coordinates,

$$\nabla^2 = \frac{1}{r^2}\frac{\partial}{\partial r}(r^2\frac{\partial}{\partial r}) + \frac{1}{r^2\sin\theta}\frac{\partial}{\partial\theta}(\sin\theta\frac{\partial}{\partial\theta}) + \frac{1}{r^2\sin\theta}\frac{\partial^2}{\partial\psi^2} \tag{2.15}$$

To reduce this complex expression, several approximations are made. First, the radius of curvature of the sphere is assumed to be much larger than the Debye length for the system is question. In the very large radius limit, the spherical surface essentially becomes a plane. In this case, only the radial component of the potential will survive. Assuming the potential has only a radial component and applying the chain rule to the first term of (2.15) yields

$$\frac{d^2\phi}{dr^2} + \frac{2}{r}\frac{d\phi}{dr} = -\frac{\rho}{\epsilon\epsilon_0}. \tag{2.16}$$

Using the form of the charge distribution given by (2.7),

$$\frac{d^2\phi}{dr^2} + \frac{2}{r}\frac{d\phi}{dr} = -\frac{e}{\epsilon\epsilon_0}\sum_i c_{0i}Z_i\exp\left[-\frac{eZ_i\phi}{kT}\right]. \tag{2.17}$$

Again, the exponential term is expanded assuming low potentials compared to the thermal energy. Similar to (2.11), this gives

$$\begin{aligned} \frac{d^2\phi}{dr^2} + \frac{2}{r}\frac{d\phi}{dr} &= \frac{e^2\phi}{\epsilon\epsilon_0 kT}\sum_i c_{0i}Z_i^2 \\ &= \kappa^2\phi, \end{aligned} \tag{2.18}$$

where, again,

$$\kappa = \sqrt{\frac{e^2}{\epsilon\epsilon_0 kT}\sum_i c_{0i}Z_i^2}. \tag{2.19}$$

This equation has the solution

$$\phi(r) = K_1\frac{\exp[-\kappa r]}{r} + K_2\frac{\exp[\kappa r]}{2r\kappa}. \tag{2.20}$$

To find the constants K_1 and K_2, two boundary conditions are once again needed. Similar boundary conditions as those used in the 1D case are used: $\phi(r = R) = \phi_0$ and $\phi(r = \infty) = 0$. Equation (2.20) yields $K_1 = \phi_0$ and $K_2 = 0$. As in the 1D case, ϕ_0 is the potential difference between the bulk solution and the physical surface and R is the radius of the surface in question. Combining all these results, the potential of a spherical particle placed in an electrolytic solution is given by

$$\phi(r) = \phi_0\frac{R}{r}\exp[-\kappa(r - R)]. \tag{2.21}$$

From (2.19), it is evident that the Debye Length is dependent on the bulk concentrations and valencies of the ions present in solution as well at the temperature and dielectric constant of the solution. Interestingly, the conditions on the surface, such as the potential, do not affect the screening length. It is a property purely of the solution.

2.3 Stern's Modification of the Gouy-Chapman Model

As with the model proposed by Helmholtz, the Gouy-Chapman model failed to accurately predict the differential capacitance of solid-liquid interface systems. In fact,

the differential capacitance predicted in the Gouy-Chapman model rises infinitely with increasing surface potential, ϕ_0, according to (2.14). Experiments by Grahame and others, however, showed that C_D did not rise indefinitely and, in fact, saturated at high values of externally applied bias.

It is important to note here that, while the theory references a potential with respect to the bulk solution, ϕ_0, an experimenter only has control over the external bias, V, that is applied to an electrode. For that reason, the notion of the potential of zero charge (PZC) was introduced in 1928[2].

The overall charge that develops at the solid-liquid interface is clearly a function of the external bias applied to the solid surface. The potential of zero charge is the external bias applied to an electrode at which no charge will aggregate at the electrode-solution interface. In essence, this is the point at which the externally generated potential matches that of the bulk solution, thus ridding the system of any potential gradients that would normally drive the formation of the double layer. Once this point is defined and/or measured, measurements of the differential capacitance, which have control only over V, can be compared to the theory, which describes only ϕ_0. Previous to this definition, the two systems (model and experiment) held different potential reference points. The model declares the bulk solution to be the potential reference point and of course experimenters are bound to the ground level of their machines as their reference point. With this definition of the PZC, (2.14) can be rewritten as

$$C_D = \left(\frac{2Z^2e^2\epsilon\epsilon_0 c_0}{kT}\right)^{\frac{1}{2}} \cosh\left(\frac{Ze(V - V_{PZC})}{2kT}\right), \tag{2.22}$$

where V_{PZC} is the potential of zero charge.

The infinite differential capacitance predicted by Gouy and Chapman arises from the fact that the continuum charge distributions used in their models failed to account for the finite size of ions and thus charges in this model could approach infinitely close to the solid surface at high surface polarizations. To overcome this, Stern proposed

a model that can be thought of as a combination of the Helmholtz model and the Gouy-Chapman model.

Stern proposed a modification to the Gouy-Chapman model asserting that ions in solution could not approach infinitely close to the surface. He declared that the distance of closest approach of an ion was its hydrated radius. When this idea is introduced, it leads to a charge distribution that consists of a single layer of charges parallel to the solid surface, termed the "Stern layer", with increasingly mobile and decreasingly densely packed charges further from the surface in the diffuse layer. The model resulting from Stern's modification to the Gouy-Chapman model is often referred to as the Gouy-Chapman-Stern model.

The potential produced by such a charge distribution is an initially linear potential drop across the Stern layer of charges, similar to that of a parallel plate capacitor, followed by an exponential potential drop though the diffuse layer, as proposed by Gouy and Chapman. The potential on the solid surface with respect to the bulk solution is the "surface potential", ϕ_0. The potential at the outer boundary of the Stern layer with respect to the bulk solution is known as the "Stern Potential", ϕ_{Stern}. Therefore the potential distribution, in this case for a planar object, in the Gouy-Chapman-Stern model is given by

$$\phi(z) = \begin{cases} \frac{\phi_{Stern}-\phi_0}{d_{Stern}} z + \phi_0 & z \leq d_{Stern} \\ \phi_0 + \phi_{Stern} \exp[-\kappa z] & z > d_{Stern}. \end{cases}$$

Here, d_{Stern} is the thickness of the stern layer, which extends from the surface and terminates at the centers of the solvated ions forming the Stern layer.

The Stern layer can be implemented into models with varying degrees of complexity. The layer can be considered to consist solely of solvated counterions (large shaded circles in Figure 2.6), or be a mixture of solvated counterions and individual solvent molecules, or it could form from some specifically adsorbed ions, or some combination of all of these. The specific adsorption of ions to the surface takes place

when covalent bonds are formed between the ions in solution and the atomic of the solid surface. Furthermore, the strength of the ions' bond to the surface can have a large impact on the dielectric properties of the Stern layer, the value of which plays a role in the magnitude of the potential drop across the Stern layer. For these reasons and others, a great deal of the current work on the solid-liquid interface is focused on understanding the behavior of the Stern layer. Regardless of what level of detail is used to model the Stern layer, its presence solves the problem of infinite differential capacitance. It does so by limiting the distance of closest approach of ions in solution to the solid surface.

2.4 Grahame's Contribution

Grahame contributed to both the experimental and theoretical treatments of the solid-liquid interface. In 1947, he wrote a review of the various models of the EDL, including those developed by Helmholtz, Gouy, Chapman, and Stern. In this review, he also expanded on the ideas of Stern and performed some of the first experimental studies of these models. He proposed that the solvent molecules could potentially form the first, compact layer adjacent to the electrode surface. Along with solvent molecules, Grahame posited that even uncharged molecules could specifically adsorb to the surface[31]. The next layer, he proposed, would be composed of solvated ions. This led to the defining of two planes. The plane parallel to the surface at a distance of one solvent molecule radius is called the "Inner Helmholtz Plane" (IHP). Parallel to the IHP and located a distance of one solvated ionic radius from the surface is the "Outer Helmholtz plane" (OHP). The region beyond the OHP is the diffuse layer defined in the Gouy-Chapman model. Figure 2.6 gives a schematic representation of the Outer Helmholtz Plane and its position with respect to a surface. Beyond this, Grahame also derived an expression for the surface charge density present in the whole double layer as a function of the potential drop across the diffuse layer. He

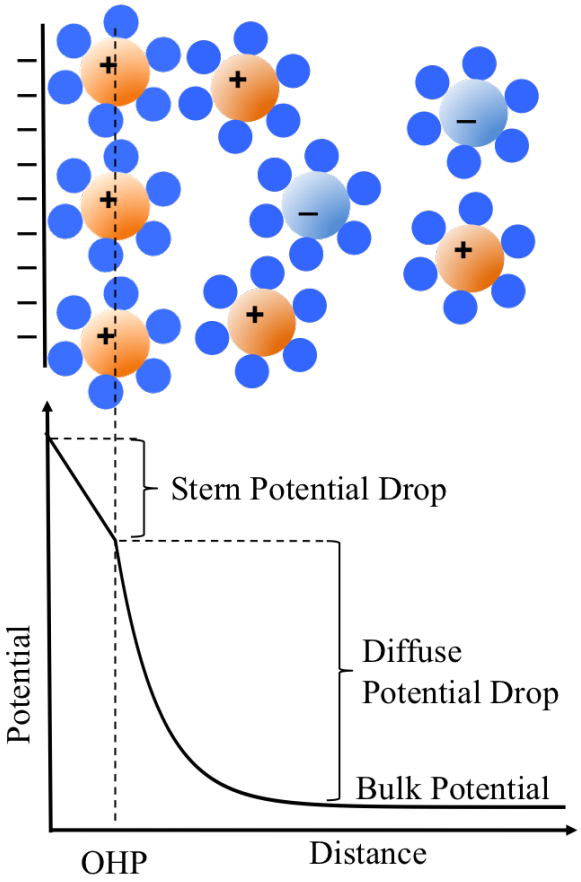

Figure 2.6: Schematic representation of the charge and potential distribution according the Gouy-Chapman-Stern model. The charge (negative in this example) on the metal surface (dashes) attracts counterions in solution (large circles). The distance of closest approach of the counterions is defined by the Outer Helmholtz Plane (OHP). The location of the OHP, in turn, is dependent on the radius of the counterions and the solvent molecules (small circles). The potential drops linearly through the Stern layer out to the OHP and then exponentially through the diffuse layer to the bulk value. The Inner Helmholtz Plane (IHP) is not considered in this potential profile.

showed that

$$\sigma = \sqrt{8c_0\epsilon\epsilon_0 kT}\sinh\left(\frac{e\phi_0}{2kT}\right), \tag{2.23}$$

where ϕ_0 is the potential difference between a point in the bulk solution and a point that lies on the OHP[31]. This is known as the Grahame equation. It was derived assuming that the solvated ions had a distance of closest approach to the surface given by the position of the OHP. A more detailed analysis of this theory will be discussed in the final chapter when it is applied to analyze my experimental data.

2.5 Further Refinement of Models

The theories laid out thus far have been what are called "continuum" models because they treat the solution, consisting of solvent molecules and ions, as a perfectly continuous medium. Although Stern and Grahame considered the finite size of solvated ions and declared a distance of closest approach to the surface based on this value, the discreteness of their models stopped there. Much of the recent research in the field has focused on treating the system in a more discrete manner. This involves correcting for ion-ion interactions, steric crowding, etc., and typically relies on computational modeling[9, 22, 28, 50]. Those models that attempt to treat the ions discretely, but the solvent in a primitive, continuum manner are referred to as "primitive models". Impressively, the models of Gouy, Chapman, Stern, and Grahame are more than sufficient to explain a wide array of solid-liquid interface phenomena without the need for the addition of discreteness[5, 13].

2.6 Forces Due to Double Layer Interactions: DLVO Theory

While the models mentioned thus far were concerned with describing the charge distribution around an object in solution, researchers quickly began wondering if these

theories could explain any well-studied phenomena. The first application of these models was put forth in an attempt to explain coagulation of colloids in solution. Aggregation of aqueous dispersions had been well-studied experimentally up to the 1940s, yet no quantitative model existed to explain the particular behaviors of such dispersions. Roughly simultaneously, Derjaguin and Landau and Verwey and Overbeek derived analytical theories that could quantitatively describe particulate coagulation in solution[69, 18]. The theories from the two groups were derived slightly differently but arrived at similar results. Hence, the theory is collectively known as DLVO theory. In essence the theory combines the long-range EDL forces, which were described by Gouy, Chapman, and Stern, with the close-range van der Waals forces to fully describe the interaction between colloids in solution.

This method was successful in explaining phenomena that were known only empirically previous to its development. For instance, DLVO theory yields a quantitative dependency between the coagulation rate and salt concentration in solution. It was the first theory to do so. DLVO theory does, however, also have its shortcomings. For example, it cannot explain the formation of colloid crystals or the stability of some colloidal dispersions[42, 52]. The analytical foundation of this theory, however, still serves as the basis for most models of double layer interactions. Applications of DLVO theory will be discussed in later chapters, specifically in the context of measurements of double layer interactions in Chapter 4. First, however, Atomic Force Microscopy will now be introduced as a general nanoscopic measurement technique and then its applicability to measurements of the solid-liquid interface will be discussed.

Chapter 3

Atomic Force Microscopy

The majority of the research I have done with respect to solid-liquid interfacial potential measurements relies on the use of AFM. Specifically, colloidal force measurements form the foundation of my work in the field and are where I have contributed to the development of new techniques and analysis. For that reason, I present in this chapter an introduction to the construction and operation of an AFM. I will also describe in some detail several different operational modes of AFM. Note that many details of equipment and specific designs will be limited to the type of instrument I used while performing measurements for this thesis (Nanotec Dulcinea control unit and Nanotec Lanza/Cervantes AFM heads).

Atomic Force Microscopy is the go-to tool for the measurement of nanoscale interactions in a variety of environmental conditions. The AFM is useful for ascertaining an array of physical properties of a sample such as elasticity, roughness, electrostatic potential difference, or magnetic field strength. An AFM by definition, however, measures forces and only forces. By carefully crafting the experimental setup, one can extract the aforementioned properties, but to do so, one must be able to relate the force measured by the apparatus to the property in question. The lateral and vertical resolutions of the instrument are dependent on the particular choice of equipment. Many different operational modes have been developed to serve a myriad of experimental needs. However, the basic operational principles hold true for almost all operation modes.

3.1 How AFM Works

The standard AFM consists of a cantilever with a probe at one end, laser, photodetector, a digital control unit, and at least two piezoactuators as depicted in Figure 3.1. There is, as will be shown, much more included in a typical experimental setup, but these components form the basis of any AFM system. The microscopic cantilever and its embedded probe are brought close to the surface via a 3D piezoelectric raster scanner mounted under the sample stage. The forces on the cantilever-probe system cause the cantilever to bend. To monitor this motion, a laser beam is directed at the back of the cantilever and the reflected laser beam is collected and registered by the segmented photodetector.

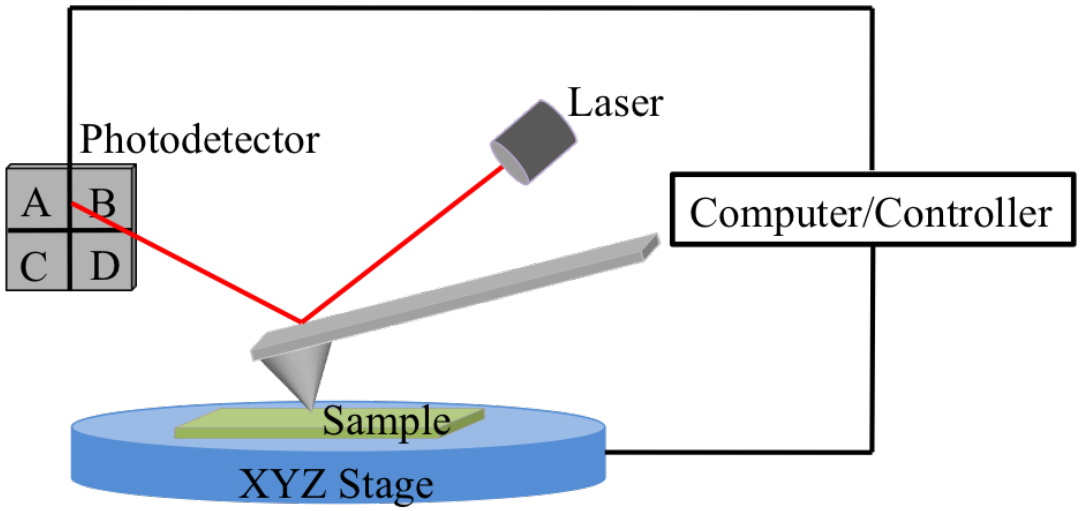

Figure 3.1: Schematic of a typical AFM system. The cantilever/tip system is brought near a sample and its three-dimensional movement is monitored via a laser beam that is reflected off the back surface of the cantilever. The reflected beam is collected at a quad-segment photodetector and a computer controlled feedback system is used to adjust the position of the sample according to various feedback input parameters defined by the user.

The cantilever is usually approximately 200 μm in length, 50 μm wide, 1 μm thick. The probe is typically a sharpened conical tip which is defined by its height, nominal radius, and cone angle. The cantilever and tip's geometrical dimensions have

a large impact on the force sensitivity of the AFM system. The average commercially available cantilever tips are on the order of 20 μm long, with a half cone angle of approximately 30°, and a nominal radius of 50 nm. Systems employing these cantilevers have a lateral resolution of on the order of 30 nm and vertical resolution of 0.5 nm. Cantilevers are etched from silicon or a silicon-based composite material and can be treated with a variety of coatings to alter their behavior under different experimental conditions. For example, gold and platinum coatings are frequently used to make the cantilever a conductor of electrical current. In terms of modeling, the cantilever/tip system is almost always considered to be comprised of a beam, truncated cone, and sphere embedded at the end of the cone.

The laser uses light generally in the visible range with wavelengths on the order of

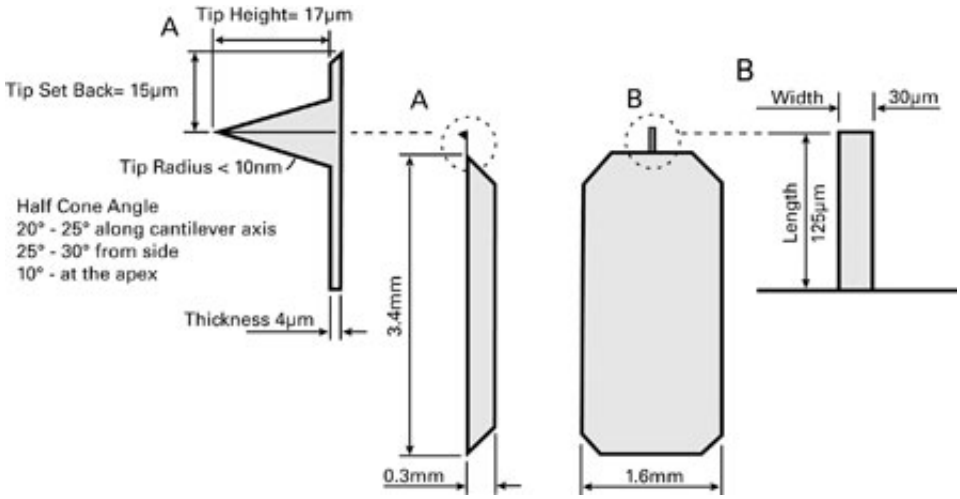

Figure 3.2: Schematic of a typical AFM cantilever on a larger silicon chip. Image courtesy of Budget Sensors ®.

500 nm and power in the range of 5 mW. It is shone onto the back of the cantilever and the reflected beam is used as a proxy to measure the movement of the cantilever. The motion of the reflected beam is measured by a quad-segment photodetector as shown in Figure 3.1. The photodetector measures the position of the reflected beam in a 2-D plane, which can be related to the 3-D motion of the cantilever. Each position of the laser spot on the silicon detector generates a current which is converted to a

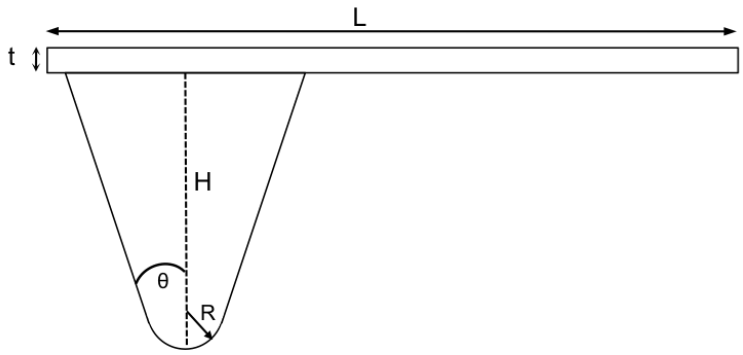

Figure 3.3: The standard model for the AFM cantilever/tip system. The cantilever is a flat beam of length L, width w (not represented), and thickness t. The tip is composed of a truncated cone, with characteristic height, H, and angle θ with a sphere of radius R embedded at the end.

voltage and then sent to the digital controller unit. Segments labeled A, B, C, and D have respective voltages of V_A, V_B, V_C, and V_D. The current generated is dependent on what fraction of the beam is radiated on each of the four segments of the detector. For this reason, the beam diameter is an important parameter and generally needs to be on the order of the side length of one of the four square segments. In order to actually convert the beam position to cantilever motion, the detector registers the amount of light entering each segment. This information is passed to the computer, which runs through a simple calculation. To monitor the vertical displacement of the cantilever, the computer calculates $(V_A + V_B) - (V_C + V_D)$. To monitor the horizontal displacement, the computer calculates $(V_A + V_C) - (V_B + V_D)$. With knowledge of the displacement in each direction and the effective spring constant of the cantilever, one can calculate the force on the cantilever in each direction. One of the piezoactuators, the piezo scanner, is used to move the sample or cantilever/tip system in the x-y plane in order to scan and acquire data over a specified area. The range of standard piezo scanners is on the order of 10 μm.

Despite its name, an AFM does not measure forces directly. All that is measured is the deflection of the cantilever via the reflected laser beam. This can be easily converted to a force, however, with knowledge of the spring constant of the cantilever.

The spring constant can be obtained via a number of methods. One method involves adding a known load to the cantilever and measuring its deflection. Another involves applying the equipartition theorem to the cantilevers thermal noise spectrum. Yet another involves measuring the dynamic response of the cantilever to an external driving force applied over a range of frequencies[51].

3.2 Operational Modes Of AFM

All operational modes of AFM require the use of a feedback system. In a feedback system, a signal which is an output of the measurement system is fed back into the system and used as an input measurement for some sort of modification or adjustment signal[7]. Specifically, AFM systems generally apply what is known as a Proportional-Integral-Derivative (PID) feedback mechanism. In this type of feedback system, the error or difference between an input signal and a desired value for that signal is minimized. To do so, the input signal is measured and an error is calculated between its value and the set point value. Then the system adjusts a particular control variable in order to further minimize the error. This cycle repeats until stopped by the user.

Each unit in the PID network functions slightly differently. The P unit uses a gain that is proportional (P) to the error signal as its input to the control variable. The I unit uses a gain that is proportion to the integral (I) of the error signal as integrated over a certain number of previous cycles. The D unit uses a gain that is proportional to the derivative (D) of the error signal as a function of time as its input to the control variable process. The input value to the feedback system is a voltage which represents a physical parameter of the experiment. For the majority of AFM measurements, the control variable is used to adjust the vertical position of the sample with respect to the AFM tip and the input signal is some property of the cantilever motion.

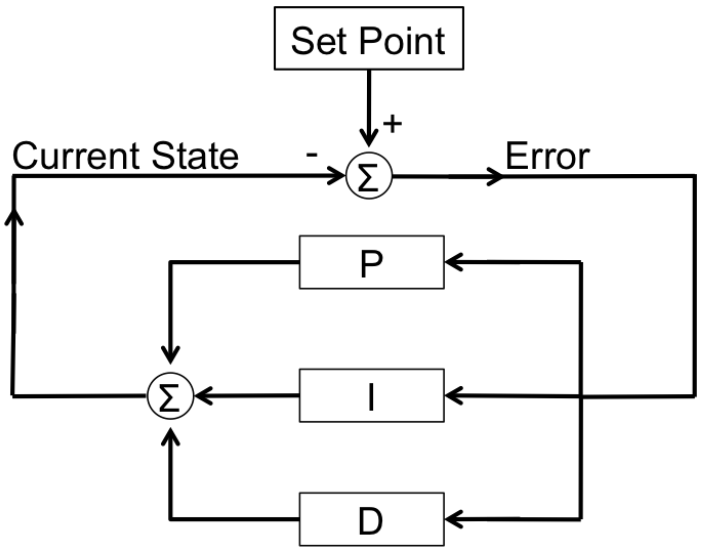

Figure 3.4: Block diagram of a PID feedback loop. A desired state is input by the user. The difference between that set point and the current state of the system (error) is calculated and used as the input for the PID network. The output is a control sequence which gives the system some instruction as to how to change its state. The process is then repeated continuously.

3.2.1 Contact Mode

In the simplest operational mode of AFM, the tip is brought into contact with the surface and scanned over a user-defined area. This is known as contact mode. The feedback parameter here is the z-component of the total force as measured by the photodetector. This is known as the "normal force". The feedback is usually employed to keep the normal force constant. In order to do so, the feedback output uses the piezo to move the sample in the z-direction, thus adjusting the deflection of the cantilever as it encounters objects or features on the surface. The voltage sent to the piezo which is required to keep the normal force constant is then digitized and turned into a topographical representation of the surface. The piezo can be used to withdraw the sample far enough such that the tip and sample break contact.

3.2.1.1 Direct Force Measurements In Air/Vacuum

Typically, one is interested in how the force on the cantilever/probe combination varies with separation distance. So, a commonly employed measurement is a mapping of the force on the cantilever versus the z-position of the piezo. This is known as a "force-distance curve" or "F-Z curve" or "force curve". A typical contact mode or "static" force curve taken in air or vacuum conditions is depicted in Figure 3.5.

In the figure, the blue dotted line represents the approach of the probe towards the sample and the red curve depicts the separation of the probe and sample. Force curves have a very distinctive structure that has been well explained and modeled in literature[14]. When the tip is far from the surface (A in Figure 3.5), there is no force and the cantilever deflection (force) is zero. Once the tip is brought close enough ($\sim$ 20 nm) to the surface, long-range electrostatic forces tend to pull the cantilever towards the surface. As the tip gets close and van der Waals forces begin to have an impact, the total force gradient becomes larger than the elastic constant of the cantilever and there is an almost instantaneous jump to contact with the surface (B in Figure 3.5). This is known as "snap-in" or "snap-to-contact" or "jump-to-contact". Now the tip and surface are in contact and move in unison with one another (B-D in Figure 3.5). As the sample is withdrawn from the tip, the adhesive forces between the two keep the tip "glued" to the surface until the elastic restoring force of the cantilever is large enough to pull the sample and tip apart (E in Figure 3.5). This is sometimes referred to the "pull off". One can see from the figure that the approach and withdrawal processes do not overlap when plotted with one another. One reason for this is hysteresis in the sample positioning piezo. Furthermore, the adhesive forces between the tip and sample are much larger than the attractive van der Waals forces. This is the reason for the larger force required for pull off.

This mode can be destructive to highly compliant substrates and for that reason is rarely used for biological and other physically sensitive applications.

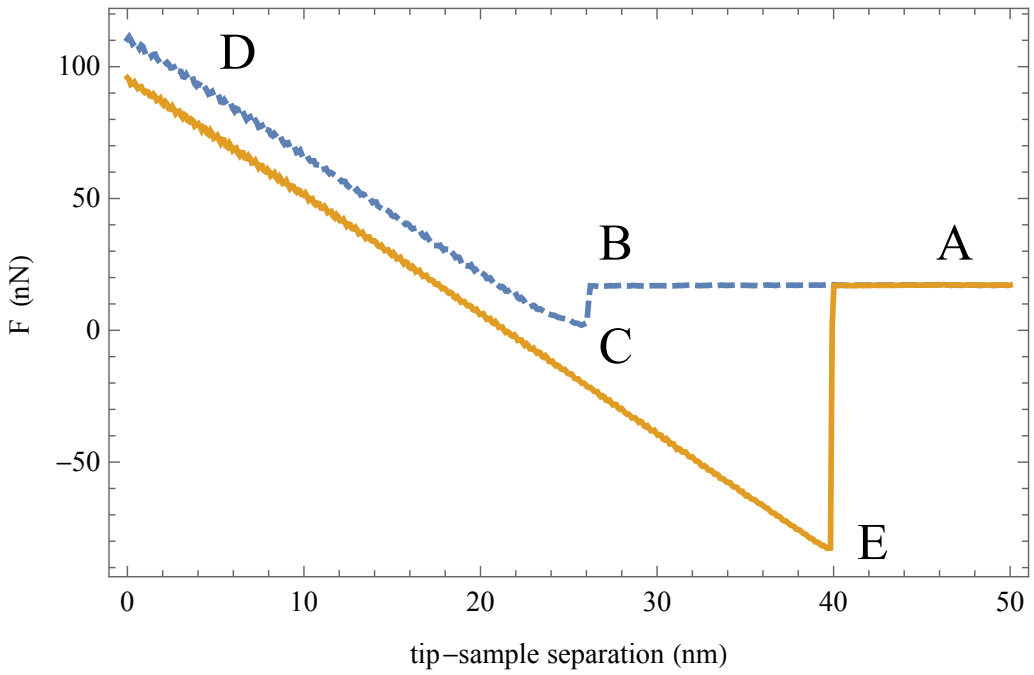

Figure 3.5: A representative force-distance curve measured in ambient laboratory conditions. The dashed line is the approach curve and the full line is the withdrawal curve. The cantilever begins far from the surface at zero deflection (A). As it approaches and the force gradient becomes larger than the spring constant, instantaneous jump to contact occurs (B). The sample and cantilever/tip are in contact and move in unison (B-D). The tip is withdrawn from the surface and eventually the adhesive forces are overcome and the tip and sample separate (E).

3.2.2 Direct Force Measurements in Liquids: Colloidal Force Microscopy

A versatile direct force measurement technique for analyzing the solid-liquid interface is colloidal probe method or colloidal force microscopy. A colloid is roughly defined as a microscopic or larger molecule or particle that is dispersed in another substance. Colloidal Force Microscopy is a method used to understand the forces on such particles as they interact with other objects, typically in a liquid environment. In fact, the first measurement with AFM of the solid-liquid interface used this technique[11]. In general, the sharpened AFM tip at the end of the cantilever is replaced by a colloidal probe. A typical colloidal probe is a silica sphere with a radius of 1–10 μm.

Colloidal Force Microscopy involves performing static force measurements, making it simple, fast, and versatile. The cantilever/probe system is approached to a surface and the force is measured as a function of separation distance similar to the force measurements discussed in Chapter 2.

The relatively large dimensions of the typical colloidal probe increase the signal to noise ratio while also minimizing the contributions from other components of the system such as the cantilever itself. The large probe size does present drawbacks, however. For instance, the lateral resolution of this method is very poor compared to techniques that employ sharp, nanoscopic tips, making it a poor choice for surface feature imaging/profilometry. The forces that cause static deflection are directly related to the electrostatic properties of the surface and probe and are unique to systems in ion-containing liquid media. The spherical geometry of the probe makes analysis of these forces easier since most basic force models such as those derived within DLVO theory, assume at least one of the interacting surfaces to be spherical in nature. Specific applications of this technique will be discussed in greater detail in Chapter 4.

Figure 3.6 shows a typical direct force measurement made with a colloidal probe in an electrolyte solution. The system consists of a $\sim$ 3 μm silicon dioxide probe attached to the end of a silica cantilever and a silicon sample surface in an aqueous 1 mM NaCl solution. It can be seen that the characteristic shape of the force-versus-distance profile is different than those in an air/vacuum measurement. Namely, the snap-in due to van der Waals forces is smaller in magnitude or not present at all in many cases. Furthermore, these forces display an exponential distance dependence and are present due to the interaction of EDL's from either surface.

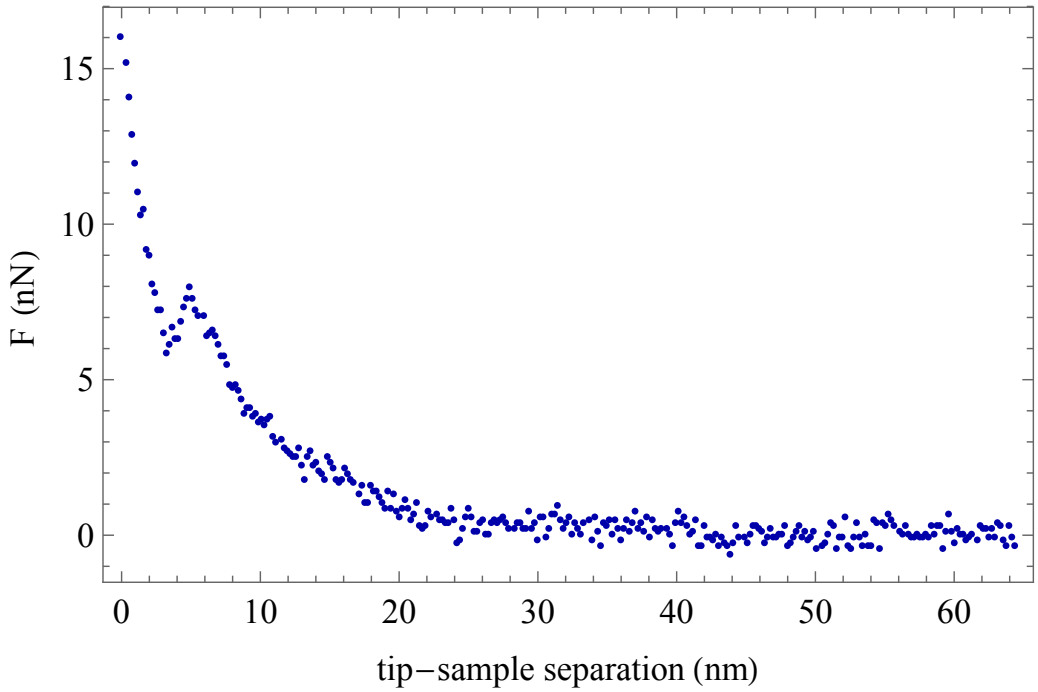

Figure 3.6: A typical force curve measured for a silica colloidal probe and a silicon sample surface in a 1 mM NaCl solution. Note the exponentially decaying force due to screening effects. Also, a jump-to-contact can be seen around 5 nm of probe-sample separation. This is not a constant feature of force curves in liquid and often the electrostatic and other repulsive forces are enough to negate any attraction due to van der Waals forces and eliminate any jump to contact.

3.2.3 Non-Contact / Tapping Mode

A more nondestructive operational mode is one known as non-contact or tapping mode. In this mode, the cantilever is physically oscillated, usually at its resonance frequency, via a piezoelectric plate on which it rests, and scanned at a certain distance above the sample. The cantilever is kept far enough from the surface so that the attractive van der Waals forces do not cause a snap-to-contact. The cantilever is then driven at its resonance frequency and the associated oscillations will bring the tip momentarily close to the surface. Forces such as van der Waals, long-range electrostatic, and air damping between the tip and surface result in a shift in the dynamic motion of the cantilever. Assuming the cantilever behaves like a simple harmonic oscillator, the cantilever will then undergo damped harmonic motion. The

variations in the forces due to the interaction with the surface will cause changes in the oscillation amplitude and/or resonance frequency. The cantilever oscillations are monitored via a lock-in amplifier (LIA). Feedback is employed to keep one or more of the oscillation amplitude, oscillation frequency shift, or phase difference between the driving waveform and the cantilever oscillations constant. Once again, the feedback output is typically the z-position of the sample. Using feedback on any one of the different parameters listed results in a different operational mode. For example, applying feedback to keep the oscillation amplitude or frequency constant is known as Amplitude Modulation AFM (AM-AFM) and Frequency Modulation AFM (FM-AFM), respectively. These modes and others like them are useful for gaining a quantitative measurement of the surface topography, adhesion, compliance, etc. One may be interested, however, in the electrical or magnetic properties of the sample. In the case of the electrical measurements, there exists a subset of operational modes, often collectively referred to as Electrostatic Force Microscopy (EFM).

3.2.4 KFM

By far, the most versatile and often used EFM mode is known as Kelvin Force Microscopy (KFM) or Kelvin Probe Microscopy (KPM). In this mode, an alternating AC potential is applied between the tip and substrate. This alters the harmonic motion of the cantilever by adding a new force to the tip/substrate interactions. When a potential is applied between any two conductors, the resulting force has the form

$$F = \frac{1}{2}\frac{d\mathcal{C}}{dz}V^2, \tag{3.1}$$

where $\mathcal{C}$ is the capacitance of the system, z is the direction whose unit vector points from one surface to the other, and V is the applied potential. In the case of KFM, $V = (V_{DC} - V_{CPD}) + V_{AC}\sin(\omega t)$, where V_{DC} is an applied static potential, V_{CPD} is the contact potential difference between the tip and sample, V_{AC} is the amplitude of the

applied sinusoidal voltage, and ω is the frequency of oscillation of the AC potential. The contact potential difference arises from a difference in work functions between the electrons in two different metals. Due to the different work functions, which can be a factor of lattice structure, doping, or contamination, the electrons in the highest occupied state within one metal will be of a different energy than those in a different metal. Thus, there is an energy difference between them and this is the source of the contact potential difference. Equation (3.1) now becomes

$$\begin{aligned} F &= \frac{1}{2}\frac{d\mathcal{C}}{dz}(V_{DC} - V_{CPD} + V_{AC}\sin(\omega t))^2 \\ &= \frac{1}{2}\frac{d\mathcal{C}}{dz}(V_{DC} - V_{CPD})^2 + \frac{1}{4}\frac{d\mathcal{C}}{dz}V_{AC}^2 + \frac{d\mathcal{C}}{dz}(V_{DC} - V_{CPD})V_{AC}\sin(\omega t) \\ &- \frac{1}{4}\frac{d\mathcal{C}}{dz}V_{AC}^2\cos(2\omega t), \end{aligned} \tag{3.2}$$

where the relation $\sin(x)^2 = \frac{1-\cos(2x)}{2}$ has been used.

It is evident from the above equations that the force between the tip due to the applied potential will be oscillatory in nature. Furthermore, it will have a static component and components that oscillate at ω and 2ω. That is

$$F = F_{static} + F_{\omega} + F_{2\omega}. \tag{3.3}$$

It is this fact that makes KFM a functional measurement technique. By setting ω properly, the cantilever can be oscillated at a desired frequency using the electrostatic interactions between it and the surface. A lock-in amplifier is employed to detect the oscillation signal, which will have components due to the electrostatic interactions and the mechanical vibration. The LIA measures the input signal, performs a version of Fourier analysis and reports the amplitude of oscillation at a particular frequency. Many different measurements can be made once the cantilever is set in motion. For example, the contact potential difference between the surface and tip can be found by oscillating the cantilever using the AC potential while simultaneously applying a DC potential and varying its value. As seen above, the ω component of the force is

dependent on $V_{DC} - V_{CPD}$. Thus, the force is minimized when the applied DC potential is equal to the contact potential difference. The characteristic plot of amplitude of oscillation versus applied DC voltage will have a minimum where $V_{DC} = V_{CPD}$ as seen in Figure 3.7. This is the most fundamental use of KFM. Of course, the

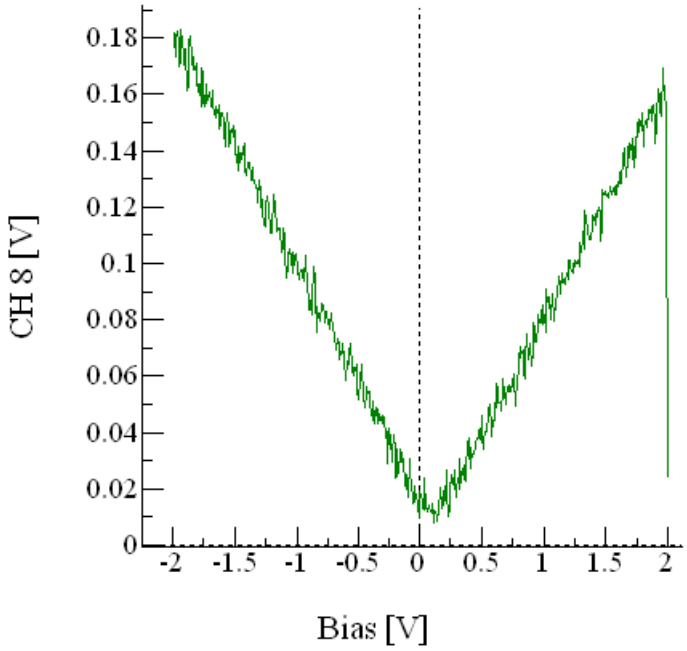

Figure 3.7: A characteristic "V Curve" showing the minimum in the oscillation amplitude, shown here as CH8, at ω due to the applied potential. The minimum occurs at an applied DC potential equal to the contact potential difference between the tip and the surface.

practical uses for this technique have been extended to measure new surface properties. Currently, a great deal of interest is being placed on performing these types of electrostatic measurements in liquid environments, as will be discussed in the next chapter.

Now that some of the basic operational principles and modes of AFM are understood, we can turn our attention specific systems of interest to the research presented in this thesis. Namely, I will discuss the various experimental approaches used to

understand the electrostatic properties of the solid-liquid interface.

Chapter 4

Previous Nanoscopic Measurements of the EDL

The solid-liquid interface is a system of great current interest in several academic and industrial fields. Because it is known that, at small scales, the screening and other effects from the EDL can be the major driver of system dynamics and behavior, much of the current work is focused on addressing this particular facet of the interface. In this chapter, previous studies involving interfacial measurements will be discussed. The discussion will focus on measurements and measurement techniques involving electrical characterization of the EDL at microscopic and nanoscopic length scales. This chapter consists of a basic executive summary of these developments followed by a more in-depth exploration of specific studies and their results as they pertain to small scale measurements of the EDL and its properties. The executive summary will focus on previous research that relates most directly to the work I have performed, while the subsequent listing will include further works that may not be as directly related, but nonetheless provide context for my work. Again, this is done in order to place the novel measurements and developments I will present in Chapter 5 within context.

4.1 Executive Summary

Our understanding of the EDL and its properties has gradually increased over the last several decades. Early measurements of the double layer, like those by Grahame discussed in Chapter 2, focused on bulk characteristic measurements. As computa-

tional and experimental tools became more powerful and sophisticated, researchers began to explore the EDL at smaller and smaller length scales. Within the last decade, micro and nanoscopic devices have been built that rely on the presence of the EDL to operate. Roughy 20 years after Grahame's measurements, Tabor, Winterton, and Israelachvili developed a tool known as the Surface Force Apparatus (SFA) to measure the forces between surfaces at nanoscopic separations[66]. Some of the first measurements of EDL forces between surfaces were done using this technique.

Of course, AFM plays a large role in teasing out small-scale properties of interfaces and for that reason a great deal of effort has been put into developing newer and more sophisticated measurements, specifically of the electrical properties of surfaces in solution or the whole solid-liquid interface. Quickly after AFM was developed, multiple measurements were made of the forces between AFM probes and surfaces in electrolytic solutions. Butt made qualitative measurements of forces in solution and showed general agreement with DLVO theory in 1991[11]. Ducker and Senden followed this up with a quantitative analysis of similar measurements that was used to extract values for the potential drop across the diffuse layer of the EDL[20].

The next progression in AFM-based measurements of the EDL was the application of potentials to either the sample or the AFM probe in order to study the effects on the EDL characteristics. Ishino et al. measured the effects of potentials applied to a metal-coated AFM probe on the forces measured between it and various surfaces in salt solutions. Several groups performed measurements that are variations on this theme[41]. Arai et el. tested the effect of biasing either the sample or the probe and found a correlation between which surface was biased and the magnitude of the measured forces, but no correlation for the sign on the force[3]. These and the vast majority of all other measurements employing bias potentials to either the sample or probe utilize a three-electrode experimental setup that mimics that of an electrochemical measurement.

Barten et al. used the variation in the measured force due to applied biases coupled with a novel model of the EDL to extract the value of the solution's potential with respect to one of the three electrodes[6]. In doing so, the group was able to report the applied potential with respect to the solution itself. This work forms the basis of much of my research. The aim of my experiments is first to reproduce the results found by Barten et al. and finally provide my own method of determining an absolute potential scale on which all potentials in an AFM-based measurement of the solid-liquid interface can be measured.

In summary, the electrostatics of the solid-liquid interface have been a popular scientific topic for over a century. The last several decades have seen advances beginning in basic modeling of such systems, progressing to nanoscopic measurements that are testing the limits of many of those models. Of course, there are details in every measurement that leave the door open for further refinement and exploration. My research seeks to build on the work of Barten et al. Specifically, I aim to build a model and make measurements of electrostatic properties of the EDL using a unique two-electrode experimental configuration. Further details and motivations of this work are presented in Chapter 5.

I will now present a more detailed review of some of the scientific works that are most relevant to the research I have preformed for this thesis. This section will demonstrate the diversity of approaches taken to measure electrostatics in liquid media at small scales. This section will include some research that does not directly correlate to my work, but instead highlights the state of the field.

4.2 Unique Methods For Making In-Liquid Electrical Measurements With AFM

4.2.1 A Model for Electrostatic Actuation in Conducting Liquids – 2009

Panchawagh et al., in 2009, developed a model and performed experiments measuring the dynamics of microscopic actuators operated in conducting liquid media[60]. They were concerned mostly with the frequency dependence of the displacement of comb-drive and parallel plate actuators, which are two commonly used microelectromechanical devices (MEMs). In both systems, a potential was applied between a mobile electrode, which was suspended via a spring, and a fixed electrode. Opposite charges gather on the electrodes and an attractive force develops between them. The applied potential was constant in magnitude and the frequency was varied.

To analyze the system, they developed a model which treated the system as a simple RC electrical circuit and all parameters of interest were calculated or derived from there. Two electrodes were considered to be plates of a capacitor, each coated with a passivation layer characterized by its permittivity and resistance. The passivation layer was put in place for purposes important for practical engineering and adds little to no complication to the physical system. The conducting liquid media between the two plates was characterized by its conductivity and capacitance. Using this simple analysis, they were able to model the dynamical behavior of both the parallel plate and comb-like actuator systems. They showed that the position and stability of the mobile plates were dependent on the frequency and amplitude of the applied AC potential.

Moreover, they calculated the force on the electrodes as a function of frequency and voltage and found the critical frequency at which the actuation force due to the applied potential overcomes the restoring force of the spring and the plates "pull in" to

contact. After calculating this critical frequency and using it as a known parameter, the experimental data did not fit the model prediction for displacement as a function of frequency. While the form of the dependence (sigmoidal) is predicted correctly, the experimental data was shifted versus the model prediction. The authors gave a list of possible causes for a shift in the entire data set. They included the possible difference in liquid conductivity for small volumes versus bulk liquid, unknown native oxide layer thickness and hence dielectric response, and dissolution of salts or evaporation of the conducting liquid which would affect its electrical response.

4.2.2 Dynamic Electrostatic Force Microscopy in Liquid Media Gramse – 2012

Gramse et al. performed a number of experiments focused on electrical measurements in liquid media with AFM for several years. They first developed a method with which it is possible to measure the local dielectric properties of surfaces in conducting liquid media[33]. They then applied this technique to measure the dielectric constant of biological components bound to a surface[32]. In order to do so, they modeled the system using an equivalent circuit analysis. They considered the cantilever and tip as separate and found the critical actuation frequencies for each. The frequency here is that with which the potential between the tip and sample is oscillated.

They found that the critical frequency for the cantilever is in the 10 kHz range, whereas for the tip, it is in the 10 MHz range. This implies that the cantilever will contribute more to the interaction force than the tip at low frequencies and vice versa. One expects that if the tip is the major contributor to the force, the force resolution will be higher for higher frequencies. To test this, they performed dielectric spectroscopic measurements over a patterned surface in aqueous electrolytic solutions at varying frequencies. The sample was a surface with intermittent stripes of Si^{2+} and SiO_2.

It was shown that at high frequencies, the resolution increases and the pattern becomes more distinguished. This implies that the system is becoming increasingly sensitive to changes in the electrical properties of the surface.

Next, they used force-distance curves to quantify the capacitance and dielectric constants of the Si^{2+} and SiO_2 surfaces, respectively. Again, they did so while applying bias potentials at frequencies ranging from 10 KHz to 20 MHz and showed that the sensitivity of these measurements increases as the applied frequency increases. The argument for higher frequencies yielding higher resolution is that at frequencies in the MHz range, the EDL can essentially be considered to be static in nature. As the biasing frequency is lowered the ions within the EDL are more dynamic and hence the forces are also dynamic, leading to convolution and decreased resolution.

4.2.3 High-Resolution Frequency-Modulated Atomic Force Microscopy in Liquids Using Electrostatic Excitation Method – 2010

Umeda et al. developed a method that allowed for frequency modulation AFM (FM-AFM) to be performed in liquid environments[68]. This method involved applying a bias potential between a cantilever which had a conductive coating on its back side and a thin conducting layer (indium tin oxide) deposited on a glass window above the cantilever. The coating allowed the laser light to pass through while simultaneously acting as a counter electrode for the cantilever. By varying the frequency of the applied bias between the cantilever and the coated window, they were able to oscillate the cantilever over a range of frequencies.

The advantage of this setup is that the potential is applied between the cantilever and a counter electrode that is not the sample. This means that the electrical properties of the sample do not affect the operation. Therefore, this method is uniquely

capable of electrically exciting the cantilever with a non-conducting sample. The AFM was operated in frequency modulation mode in order to obtain topographic scans of surfaces.

They found that at lower bias frequencies, the amplitude of oscillation is increased. The peculiarly large oscillation amplitude at low frequencies is attributed to surface stress forces. The surface stress force arises when charges from solution accumulate in an asymmetric fashion on the tip side and backside of the cantilever. The fact that the surface stress dominated the cantilever deflection at low frequencies is due to the formation of the EDL. At lower frequencies, the charges have more time to approach their equilibrium positions around the cantilever and hence the EDL will be more fully formed and contribute more to interaction forces.

It can be seen that the distribution of charges around a solid surface in solution are of interest to researchers in a wide variety of fields. Several of the above studies do not focus on the characterization or measurement of the EDL, they simply note its presence and importance in modulating the behavior of their various systems.

Because the bulk of the work that I will show later in this thesis attempts to clarify some confusing terminology and interpretation of measurements in the field of solid-liquid interfacial measurements using AFM, the focus now shifts to direct measurements of double layer properties using various nanoscopic surface probe devices. The previous studies presented in this section serve as a semi-chronologically ordered foundation for the body of work developed fully in Chapter 5.

4.3 The Surface Force Apparatus

Measurements of the electrostatic potentials associated with double layer systems have been in development for nearly 40 years. The first small scale (nanoscopic) measurements of surfaces in electrolytic solutions were carried out using a device devised by Isrealachvili in 1978[43]. This device was a modified version of the Surface

Force Apparatus (SFA) developed by Tabor, Winterton and Israelachvili several years earlier[66]. This version of the device measured the forces between two cylindrical objects immersed in a salt solution as a function of their nanoscopic separations. The separations were measured via the interference fringes of multiple light beams that were passed through the system. The forces were measured via the displacement of a calibrated spring system connected to one of the two samples.

4.4 Measuring Double Layer Forces with AFM

Because of the geometrical requirement of the samples in SFA measurements, this technique was limited in its uses. Most measurements were done on mica or glass samples or surfactant-modified versions of those two materials. Further iterations of the SFA were introduced and used to measure forces between surfaces in solution. The advent of AFM ushered in a new era of measurements of the solid-liquid interface.

4.4.1 Measuring Electrostatic, van der Waals, and Hydration Forces in Electrolyte Solutions with an Atomic Force Microscope –1991

By deriving a useful analytical equation to describe the force between a sphere and plane in solution, Butt was able to quantitatively analyze data from AFM force measurement experiments in different liquid environments[11]. He showed that the size of the measured forces were in agreement with those predicted by the derived expression. The data was then used to calculate the screening length, which also agreed well with that predicted by the Debye-Hückel solution of the Poisson-Boltzmann equation.

4.4.2 Measurement of Forces in Liquids Using a Force Microscope – 1992

Later, Ducker and Senden used AFM to measure the forces between similar surfaces to extract quantitative information about "surface potentials" at a variety of solution pH's and concentrations[20]. Their results were in agreement with previously measured values using other experimental techniques and calculations. This was one of the earliest reports of using DLVO theory to find fits to experimental data on the force between surfaces in solution using AFM. By using similar surfaces, they were able to reduce the number of fit parameters since the two "surface potentials" were assumed to be equal.

How does the choice of surface effect the analysis of the output data? Recall that the only output of an AFM is the force experienced by the probe. Therefore, if one wishes to extract information about the electrostatic potentials, one needs an expression that relates the force to the various potentials of interest. This has been done in many forms by essentially extending the framework of DLVO theory to new geometries. For instance, the interaction energy as a function of potentials between two spherical particles, each surrounded by diffuse charged layers, was calculated by Hogg and Healy in 1965[39]. Lin et al. used this result to obtain a simple expression for the force between a spherical particle and a planar surface separated by a distance z[53]. This is mentioned specifically because it represents the typical model of the geometry used in AFM experiments. They found that the force for such a geometry is given by

$$F(z) = \frac{4\pi\epsilon\epsilon_0 R\phi_1\phi_2 \exp[-\frac{z}{\lambda}]}{\lambda}, \tag{4.1}$$

where ϕ_1 and ϕ_2 are the diffuse layer potentials of the two surfaces with respect to bulk, R is the sphere radius, ϵ and ϵ_0 are the dielectric constant of the medium and

permittivity of free space, respectively, and λ is the Debye length. Looking at the form of this expression it becomes clear that both potentials cannot be measured simultaneously. At least not by fitting experimental force data, since the function is indiscriminate of the two potentials. For this reason, one of the surfaces must first be electrically calibrated. That is, its potential must be known. Only then can the experimental data be fit for the remaining potential of interest. This calibration step has been handled by a number of researchers in the recent past.

The most common way to exploit the structure of (4.1) is to create a situation in which the two potentials are equal, as done by Ducker and Senden. This is typically accomplished simply by ensuring the two surfaces are chemically and physically similar, e.g., gold and gold. By doing so, (4.1) reduces to

$$F(z) = \frac{4\pi\epsilon\epsilon_0 R\phi^2 \exp[-\frac{z}{\lambda}]}{\lambda}. \tag{4.2}$$

The two potential parameters are thus reduced to one. Once the potential of both surfaces is known, the sample surface can be replaced and its potential measured via (4.1) where ϕ_1 is now known and ϕ_2 is unknown.

4.4.3 Electric Double-Layer Potentials and Surface Regulation Properties Measured by Colloidal-Probe Atomic Force Microscopy - 2014

Montes Ruiz-Cabello et al. measured the forces between colloids of different types using colloidal probe AFM[54]. They employed the "similar surfaces" method to effectively calibrate a sulfate-latex coated probe and then used that probe to measure the properties of other colloidal particles which were then themselves used as probes to measure the properties of even more colloidal particles with varying surface coatings. By measuring the force between two spherical objects of similar materials, they were able to exploit both the geometrical and compositional symmetry of the system

to utilize an equation of the form of (5.14). They then used differences between measured forces and theory to show a need for consideration of the "charge regulation parameter", which is dependent on the capacitances of the inner (Stern) and diffuse layers. They claim that force measurements should be analyzed under the assumption of constant charge regulation parameter, as opposed to constant surface charge or constant potential as is customary.

4.4.4 Stern Potential and Debye Length Measurements in Dilute Ionic Solutions With Electrostatic Force Microscopy – 2013

Other methods for calibrating the probe have been developed as well. Kumar et al. developed an analytical model and measurement scheme that consisted of multiple calibration steps plus a final measurement step. They employed multi-frequency KFM-type measurements coupled with an analytical expression for the capacitive gradient of the tip-sample system to extract a value for the potential of the AFM probe. With the potential of the AFM probe known, force measurements were fit to an equation of the form of (4.1). Their analysis included a fractional term that related the diffuse layer potential drop that was extracted from the fitting to the applied potential to the probe. In essence, this fraction represented the potential drop across the Stern layer. Their measurements were the first to use AFM to measure the potential drop across the Stern layer directly. An underlying assumption in their analysis was that the liquid in which the sample and AFM probe were immersed could be grounded by introduction of a platinum wire that was itself grounded into the solution.

4.5 Measuring Interfacial Electrostatics of Specific Systems

4.5.1 Determining Surface Potential of the Bitumen-Water Interface at Nanoscale Resolution Using Atomic Force Microcopy – 2007

In 2007, Drelich et al. derived a model for a conical tip and flat substrate interaction force that incorporated both the electrostatic contribution as well as forces due to van der Waals interaction[19]. To do so, they modified the model of Parsegian and Gingell, which calculated the force per unit area between two infinite plates in a salt solution[61]. They did so by adjusting the planar geometry of one of the surfaces to that of a truncated cone with a sphere embedded at the end. The model they developed was much more complex in form than that of Parsegian and Gingell. However, even this model, with its complex structure, suffers from the indiscriminate nature of the two potentials. That is, force data cannot be fit to this model with the hope of extracting unique solutions for the two potential parameters in a single process.

In this work, the authors first calculated the surface charge density of the sample and converted that to a "surface potential" via the Grahame equation. Their analysis, similar to other authors, required importing information about the sign of the surface charge of the probe as an input parameter in the fitting of the data.

4.5.2 Probing Anisotropic Surface Properties of Molybdenite by Direct Force Measurements – 2015

In 2015 Hu et al. used AFM to measure the "surface potentials" of the various faces of the layer-type mineral molybdenite. The measurements were carried out using a standard silicon nitride cantilever with a sharpened probe. This team utilized the force model developed by Drelich for such systems. They showed that the various surface faces of the mineral exhibited different electrostatic properties when surrounded

by an aqueous electrolyte solution. They also showed that the solution pH affected the magnitude of the potentials in the solution side of the interface.

4.5.3 Double Layer Structure of Ionic Liquids at the Au (111) Electrode Interface: An Atomic Force Microscopy Investigation – 2011

Hayes et al. used AFM force measurements to probe the adsorbed layers of ions adjacent to a gold surface in ionic liquid solutions at varied gold bias values[35]. They measured the force required to "rupture" through the various layers of adsorbed ions and observed that the ionic packing at the surface could be altered by adjusting the bias potential. Specifically, they found a constant multilayer morphology at the interface with increased numbers of ionic layers at larger (positive or negative) applied bias potentials.

4.5.4 Dielectric Constant Measurements of Interfacial Aqueous Solutions Using Atomic Force Microscopy – 2001

de Souza et al. used AFM force measurements in concert with a model of a medium with spatially varying dielectric constant to claim that variation in the dielectric constant is the reason for forces on AFM probes immersed in the EDL of other surfaces. Their work confirmed other studies that showed that the dielectric constant of the double layer region is much smaller than that of the bulk solution. No attempt is made to treat the EDL as two separate subsystems, suggesting a Gouy-Chapman type interpretation of its structure.

4.5.5 Ionic Liquids Behave as Dilute Electrolyte Solutions – 2013

Debbie et al. utilized a specialized Electrochemical Surface Force Apparatus (ECSFA) to make direct surface force measurements combined with thermodynamic arguments to demonstrate that ionic liquids behave in a similar fashion to dilute electrolytic solutions in solid-liquid interface systems[27]. More specifically they showed that the electrostatic properties of ionic liquid-surface interface systems can be described using classical Poisson-Boltzmann formulations. They show that the ionic liquids display screening and charge distribution properties similar to those of dilute aqueous electrolyte solutions.

4.6 Measuring In-Solution Potentials as a Function of Sample Biasing

4.6.1 Stern Potential Near Gold and Chromium Surfaces in Contact With Aqueous and Alcoholic Ammonium Salt Solutions – 1991

Using an early version of a surface force balance technique, Keldenich and Peschel deduced values of the potential at the Outer Helmholtz Plane with respect to the bulk solution, termed the "Stern potential"[45]. They showed that the Stern potential is dependent on the chemical composition as well as concentration of solutions and also the physical structure of the surface (gold or chromium). They noted that each surface-solution pair exhibits specific chemistries that affect the potential distribution within the solution side of the interface. Ultimately, they measured Stern potentials ranging from about 20 to 150 mV.

4.6.2 Electrical Double-Layer Forces Measured with an Atomic Force Microscope while Electrochemically Controlling Surface Potential of the Cantilever – 1994

Ishino et al. measured the response of forces between a gold-coated AFM tip and surfaces modified with various self-assembled monolayers (SAM). For each modified surface, they varied the potential applied to the metal-coated AFM tip and observed variations in the magnitude of the force for all surfaces studied. However, only for a stearic acid-modified surface did they observe a change in the sign of the force. They related the sign of forces under various conditions to the different chemical compositions of the particular monolayers under investigation.

4.6.3 Effects of Electric Potentials on Surface Forces in Electrolyte Solutions – 1995

Arai et al. used AFM to analyze the electric double layer of a gold surface in an aqueous solution of NaOH as a function of applied biasing potential. They found that the bias potential applied to either the gold sample or a gold-coated probe did affect the magnitude of the interaction force, however it had no effect on the sign of the interaction force. By performing further measurements using a probe made of silicon nitride, they concluded then that the diffuse layer potential of the gold surface is always negative within the conditions of their experiment, possibly the result of OH^- ions adsorbing the gold surface.

4.6.4 Measurement of Double-Layer Forces at the Electrode/Electrolyte Interface Using the Atomic Force Microscope: Potential and Anion Dependent Interactions – 1996

Hiller et al. measured the forces between a colloidal silica probe and silicon and gold substrates as a function of applied bias potential for various salt solutions. Fits of measured forces were used to extract values of the "surface potential". It was found that the applied potential could be used to transform the forces between the silica probe and the gold sample from attractive to repulsive. These forces corresponded to diffuse double layer potentials ranging between −47 mV and +5 mV for applied potentials of −700 mV and +100 mV.

4.6.5 Direct Measurement of Diffuse Double-Layer Forces at the Semiconductor/Electrolyte Interface Using an Atomic Force Microscope – 1997

Hu et al. measured the forces at the interface of a TiO_2 crystal and an aqueous electrolyte solution of 1 mM using a silica colloidal probe. The pH of the solution was adjusted and the effect on the measured forces was observed. Simultaneously, the effect of applied bias potentials on the measured forces was investigated at each of the various pH levels. It was found that the applied potential at which interaction forces fall to zero, referred to as the "potential of zero force" (pzf) was a function of pH. Measured forces were used to calculate values of the potential drop across the diffuse part of the double layer, termed in this work, the "surface potential". This value ranged from approximately −50 mV to +20 mV under applied potentials ranging from approximately −1000 mV to +500 mV.

4.6.6 The Electrical Double Layer on Gold Probed by Electrokinetic and Surface Force Measurements – 2002

Giesbers et al. used colloidal probe AFM as well as streaming potential measurements to measure the effect of solution pH on the double layer surrounding a gold surface[29]. Using the electrokinetic techniques, they found that the electrostatic environment surrounding the gold surface was sensitive to solution properties and noted a negatively linear relationship between solution pH and the zeta-potential. For surface force measurements, they employed a "similar surfaces" method to limit the amount of information that needed to be inferred about the system. In this way, they were able to fit experimental force measurements for only one potential as illustrated by (5.14) and found a similar inverse relationship between the "double layer potential" and the solution pH.

4.6.7 Double Layer of a Gold Electrode Probed by AFM Force Measurements – 2003

Barten et al. continued to probe the gold-solution interface by using colloidal probe AFM measurements in concert with a model developed within their group to describe the solid-liquid interface that included an oxide layer as well as the Stern and diffuse layers[6, 21]. The model was known as the "amphifunctional double layer model". Utilizing this combination, they were able to measure the effect of applying bias potentials to the gold surface in solutions of varying pH. Furthermore, they use the applied potential at which the measured force fell to zero to get a measure of the potential of the bulk solution with respect to their external power supply. By doing so, they were able to report the applied bias potentials with respect to the solution as opposed to a reference electrode. Getting there, however, required the use of a reference electrode initially. They assumed the potential of the bulk solution remained

constant even while the gold electrode was biased by several hundred millivolts, which is unlikely to be true.

4.6.8 Probing the Surface Properties of Gold at Low Electrolyte Concentration – 2016

Recently, in 2016, Tivony and Klein used Surface Force Balance (SFB) measurements on gold surfaces immersed in highly dilute aqueous electrolyte solutions to understand the effect of biasing the gold surface on interaction forces between the gold and a mica probe. From these measurements, they deduced the value of the "surface potential" of the gold electrode. They found that this potential increases from largely negative to positive as the biasing potential is increased from negative to positive.

4.6.9 Double Layer Forces Over Large Potential Ranges as Measured in an Electrochemical Surface Force Apparatus – 2001

Frechette and Vanderlick used a modified SFA to study the effect of electrode biasing on the forces between gold and mica surfaces separated by 1 mM $KClO_4$. The major achievement of this work was the study of the mica-gold system under a wide potential range (-700 mV to -200 mV). Through this large applied bias potential range, they found the gold "surface potential" to change from -200 mV to 0 mV. In subsequent publications, the same team found that the applied bias also has effect on the adhesive forces between the mica and gold in electrolyte solutions.

Experimental investigations of the double layer take many forms. This chapter has thus far focused on AFM-based measurements. Other methods include electrochemical approaches such as impedance spectroscopy and cyclic voltammetry, spectroscopic techniques such as total internal reflection microscopy and X-ray photoelectron spectroscopy (XPS), electrophoretic techniques such as streaming potential

measurements, and several others[5, 10, 13, 29, 57, 64].

4.7 Cyclic Voltammetry / Electrochemistry

As it will be compared and contrasted with AFM as a solid-liquid interface measurement technique and because it will be used in this work, a brief discussion of basic electrochemical measurements seems fitting.

Electrochemistry is the study of chemical process that cause the physical motion of electrons. A typical electrochemical measurement system is composed of a cell in which the solution is contained. Inserted into this cell are a number of electrodes. By far the most common experimental setup is a three-electrode configuration. The three electrodes include a working electrode, a counter electrode, and a reference electrode. The working electrode is the one to which a biasing voltage is applied. The counter electrode is used as a sink for the electrons in motion (current). And finally the reference electrode as a point of constant potential against which the potential of the working electrode is measured. The specific motivations for this experimental configuration are discussed in more detail in Chapter 5.

Electrochemical techniques are not particularly sensitive to small scale interactions at the interface and generally are used as measurements of bulk properties of surface/solution combinations[8, 49, 55, 59]. Furthermore, the need of a third electrode makes the use of these techniques for small, confined systems more procedurally difficult. There have been advances in combining the nanoscopic resolution of AFM with the ability of electrochemistry to detect and characterize the chemical behavior of solutions and interfaces. Namely, scanning electrochemical microscopy (SECM), developed by Bard et al., aims to bridge the gap between the two measurement techniques[4]. It is capable of topographical mapping as well as probing the surface reactivity of solid-state materials, electrocatalyst materials, enzymes and other biophysical systems[72].

One can see from the works cited above that AFM is common and highly adaptable tool for nanoscale investigations of the solid-liquid interface. Given the diverse conditions and environments in which AFM has been applied, there is still one commonality between all measurements that utilize external biasing of either the probe or the sample. They all borrow the three-electrode scheme developed within the field of electrochemistry to analyze and report their measurements. This scheme, while the standard in that field, has limitations in nanoscopic measurements. My research aims to address these shortcomings and develop a new scheme that is more suitable to AFM-based measurements of in-liquid electrostatics.

Chapter 5

Measurements of the Stern and Bulk Potentials of Metal-Electrolyte Interfaces

In this chapter, I will first present the details of the research that I have completed with respect to nanoscale electrical characterizations of the solid-liquid interface using AFM. First, I will explain the development of a specific nomenclature that clarifies several commonly encountered concepts in measurements of the type I have employed. This will include the definition of terms and mathematical descriptions of their relationships. That will be followed by a description of a model of the force due to double layer interactions between two surfaces that will be the basis of the analysis of my measurements. I will then walk through the derivation of mathematical relations between the various potential drops that occur within the EDL. After laying out the theoretical developments I have made, I will describe in detail the experimental procedures that I carried out in order to characterize the EDL in a more complete fashion and discuss the results of such these measurements.

5.1 A New Nomenclature for Solid-Liquid Interface Systems

Often, in experimental sciences, the goal is simply to devise a simpler way to measure a certain quantity of interest. Of course, this simpler method should preserve or improve current levels of accuracy and resolution available with established methods. Simpler in this case means with less cumbersome equipment or fewer analytical or

procedural steps. My contribution to the field of nanoscale interfacial measurements is the development of a method to more simply measure the potential drop across the diffuse layer of a sample. In order to facilitate simpler experimental procedures for measuring the electrostatic nature of the solid-liquid interface with AFM, a new theoretical framework was deemed necessary. To that end, I devised a novel model of a nanoscopic system consisting of two electrodes, separated by a liquid, and held under potential control. The inclusion of only two electrodes is the simplifying factor of this model and experimental setup. Previous to this work, a three-electrode scheme with more complex electrical relationships was the standard in the field.

The implementation of the model, along with an associated nomenclature, accomplishes two main feats of scientific interest. First, much of the ambiguity due to poorly developed and maintained conventions is eliminated. Secondly, the simple algebraic model requires only a single parameter to be measured experimentally and from there, predicts the behavior of system components. In this way, measurements of only that single parameter can lead to a full characterization of the electrode-liquid-electrode system.

5.1.1 Potentials and Potential Differences

In many investigations of the solid-liquid interface, a value referred to as the "surface potential", "double layer potential", "absolute potential", "effective potential", or some combination thereof is often the parameter which is measured or inferred and reported [10, 20, 24, 25, 46, 58, 67]. In reality, these terms almost always refer to the potential difference between a point on or near the solid surface and a point within the bulk solution, assumed to be infinitely far from every other component of the system. The exact spatial origin, i.e., exactly at or somewhere near the solid surface, depends on the model chosen to examine the system. The term "surface potential", however, is also used frequently in studies that employ electrochemical techniques to

describe the biasing potential applied to the working electrode. This is an example of the ambiguity in the description of electrostatic potentials that is present throughout much of the literature in the field. Typically, the exact terminology used is field-specific, only complicating things more.

Another layer of confusion is created when one considers the electrostatic potential coordinate reference system employed in many investigations of the solid-liquid interface. As discussed briefly in previous chapters, the in-solution potential drops that occur across the Stern and diffuse components of the EDL are inherently referenced to the bulk solution in all theoretical models. In many AFM-based, as well as electrochemical measurements, one or more of the electrodes present in the system are held under potential control. This means the potential applied to those electrodes becomes an experimental variable. These potentials, unlike the potential drops in the solution, are inherently referenced to the ground level of the power supply to which they are connected. So now there are two separate reference points against which two sets of potential drops are measured. In order to combat the obvious confusion, the field of electrochemistry has adopted the practice of introducing the reference electrode as a point of constant potential against which the externally applied potentials can be measured.

The need for the reference electrode becomes clear when it is recognized that it is impossible to measure the potential difference between two phases of matter with purely ohmic techniques like those employed in electrochemical measurements[5]. For this reason, knowledge of the bulk solution's potential with respect to some external ground or reference has eluded researchers. Since all in-solution potential drops are referenced to this possibly shifting reference point, analysis of their measured values is not always easily understood.

By building on the work of Grahame and Stern, the model I will present demonstrates that it is analytically and experimentally possible to devise a measurement

using AFM that can yield values of the two major potential drops (diffuse and Stern) that occur in the solution phase. Furthermore, it yields analytic expressions for the potential at several other points of interest, including that of the bulk solution, with respect to an external reference point. The measurements by Brown et al. are the clearest attempt to present all potentials on an absolute scale, but their XPS measurements required access to and use of a highly specialized X-ray light source[10].

Measurements akin to those performed by Barten et al. attempt to bridge the gap between potential reference frames in AFM measurements by using the so-called potential of zero force (PZF). The PZF is the applied bias to an electrode at which the force measured between it and an AFM probe goes to zero[6, 37, 40]. It is implied that this represents the point at which all charge has been driven from the surface of the sample, essentially matching the potential of the sample to that of the solution. This point is then declared to be the potential of the solution with respect to an external point, and is assumed to be static. While this is a reasonable approach, it requires a measurement scheme that mirrors electrochemical ones in that it requires the third reference electrode. It also glosses over the fact that the bulk solution potential may change throughout a measurement due to the bias potentials applied to the working or any other electrode.

While it is widely known that the EDL consists of a compact or Stern layer, which acts as a capacitive element within the overall system, the measurements by Kumar et al. are the only known instance of AFM being employed to measure the potential drop across the Stern layer directly[48].

In a typical colloidal probe force measurement, the probe and sample are either insulated by themselves or connected to an external power supply. It is of interest to know how biasing the probe or sample or both affects the EDL at their respective interfaces within the solution and, in turn, the forces between them. As discussed earlier in this chapter, the application of external bias potentials to either surface

introduces another electrical reference point (i.e., the power supply ground) besides the bulk solution potential and these separate reference points have the potential to make the measurements much less informative if not treated appropriately. The possibility of an experiment having multiple of these electrical reference points came up frequently in the analysis of the experiments carried out in my research. I therefore saw a need to ensure that all measurements of in-solution potentials that included the use of external bias potentials had a congruous and simple electrical potential coordinate system.

To that end, I propose here a combination of nomenclature and physical model of an EDL system which eliminates any ambiguity in terms of potentials and their respective reference points. Consider an experiment with two electrodes separated by an electrolytic solution. Both electrodes are connected to a common power supply with its own ground. We can map the potentials of all points of interest for two cases; the Gouy-Chapman case in which only a diffuse layer of ions is present and the Gouy-Chapman-Stern case in which there is both a diffuse layer and a compact Stern layer. Using these two interpretations, we have the two models in Figure 5.1. Here, the ground of the power supply machine is taken as the zero point and all potentials (V's) are referenced with respect to it. All corresponding ϕ's represent differences between those potentials. Looking at the two models separately: in the G-C model, V_s is the potential of the sample with respect to machine ground, V_b is the potential of the bulk solution with respect to machine ground, V_p is the potential of the probe with respect to machine ground. Within the solution, ϕ_{sb} is the potential difference between the sample surface and the bulk solution. This is the diffuse layer potential drop that is almost always referred to as the "surface potential" in literature. The potential drop from the probe surface to the bulk solution has a similar form in this nomenclature, ϕ_{pb}.

In the Gouy-Chapman-Stern model of the EDL, the situation is slightly more

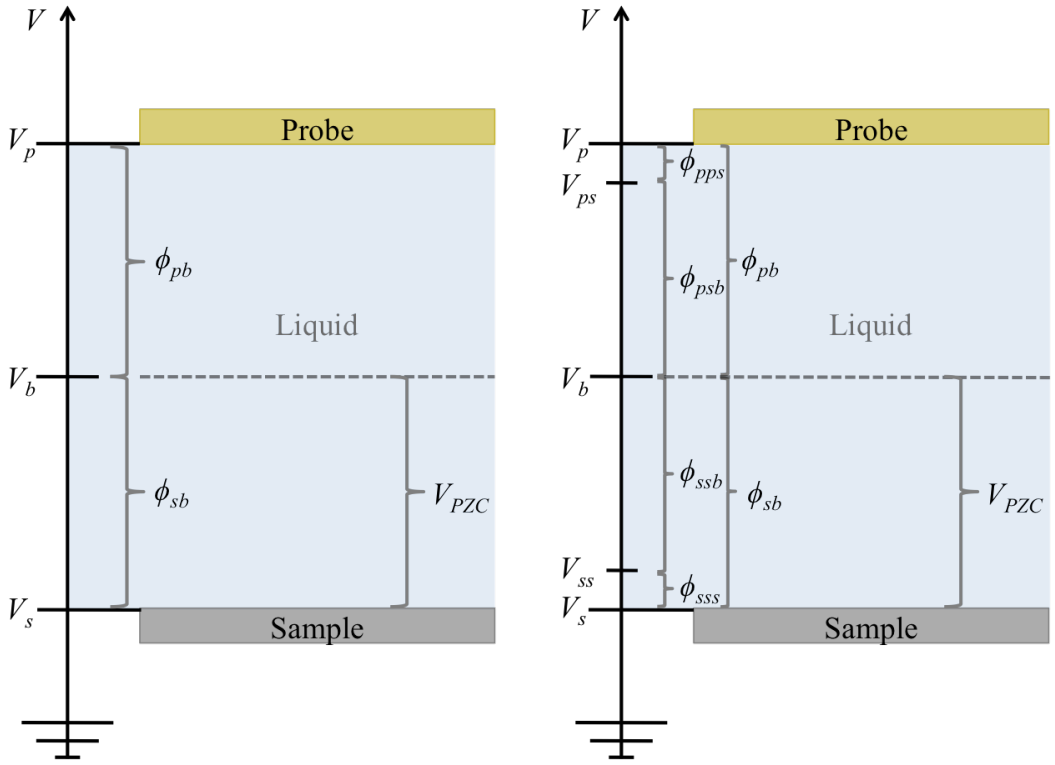

Figure 5.1: Potential level diagrams for the (a) Gouy-Chapman and (b) Gouy-Chapman-Stern models. The V's represent potentials measured with respect to the external machine ground and the ϕ's represent differences between the V's. Either ϕ_{ssb} or ϕ_{psb} are what are measured in a typical force experiment.

complex. V_s, V_p, and V_b retain their same meanings as before. V_{ss} and V_{ps} are the potentials of sample and probe, respectively, at the outer edge of the Stern layer with respect to machine ground. As for the potential drops in the solution, ϕ_{sss} and ϕ_{pps} are the potential differences from the electrode surface to the outer edge of the Stern layers, placed at the OHP, of the sample and probe, respectively. Similarly, ϕ_{ssb} and ϕ_{psb} are the potential drops from the OHP to the bulk solution. Finally, ϕ_{sb} and ϕ_{pb} are the potential differences between the bulk solution and the surface of the sample and probe, respectively. The reason for this nomenclature becomes more obvious when written mathematically as

$$\begin{aligned} \phi_{sb} = V_s - V_b \quad ; \quad \phi_{pb} = V_p - V_b \\ \phi_{sss} = V_s - V_{ss} \quad ; \quad \phi_{pps} = V_p - V_{ps} \\ \phi_{ssb} = V_{ss} - V_b \quad ; \quad \phi_{psb} = V_{ps} - V_b \\ \text{or more generally} \quad \phi_{ij} = V_i - V_j. \end{aligned} \tag{5.1}$$

5.1.2 Geometric Definition of the Bulk Potential

In many electrochemical and other measurements of solid-liquid interface systems, the potential of the bulk solution is assumed to be independent of the biasing of the electrodes. This may be a reasonable assumption for macroscopic investigations, which typically involve hundreds of milliliters of electrolyte solution with electrodes separated by tens of centimeters. From the perspective of ions in the vicinity of the electrodes, this equates to an essentially infinite space. In AFM-based investigations, however, typical measurement cells contain amounts of solution on the order of micro-liters and electrode separations on the order of nanometers. Furthermore, the surfaces of the sample and probe are large enough to be approximated as infinite planes when compared to the small separation distances. This approximation essentially reduces the system to a parallel plate capacitor with a dielectric inserted between the plates. From a purely geometric standpoint, then, the potential of the solution between the two electrodes will be a function of the distance from and relative potentials of either electrode as is the case in a parallel plate capacitor.

Note that the definition of the bulk potential presented here differs from the one sometimes used in literature. In the definition of bulk potential used in this work, it is the power supply, among other factors, that determines the potential at any point in the solution. In the case of two flat sheets of charge, the potential at a point exactly half way between the plates is equal to one half the potential difference between the plates. This is true no matter how the potential varies in space (linearly,

exponentially, etc.). Thus, in my model, the bulk solution potential has a contribution from the potential difference between the electrodes equal to half of the potential difference. The bulk solution potential in this model has another component that comes from any initial charging of the solution that may occur in preparing, stirring, transferring, etc. of the solution itself. This leads to an offset potential that exists before any experiment begins. Finally, the bulk solution potential can be affected by the transfer of any charge across the solid-liquid interface. In total, the bulk potential can be written as

$$V_b = V_0 + \frac{1}{2}\Delta V + V_q(\Delta V), \tag{5.2}$$

where ΔV is the potential difference applied to the two electrodes, V_q is the extra potential generated in the bulk solution by the flow of charge from either electrode across the interface, and V_0 is the potential offset between the machine ground and the interior of the solution. This offset can be measured in an experiment where ΔV is set to zero. As ΔV is shifted from zero, currents of various forms can possibly flow across the interface. The injection of charge into the solution phase of the system will affect the value of V_q and thus V_b.

5.2 Capacitive Description of the EDL

I assert that, with knowledge of the diffuse layer potential differences, which, as will be shown in the next section, can be measured via forces, paired with an appropriate electrical description of the EDL, one can infer a value for the potential drop across the compact Stern layer, and hence fully characterize the electrostatic environment of the solid-liquid interface. Tests of the limits and veracity of this assertion will be presented in the two final sections of this chapter.

Grahame showed in 1947 that the EDL at an interface can be treated as two capacitors in series. He arrived at this result by relating the total charge in the EDL,

which has the same magnitude and opposite sign of the charge on the metal surface, to the two potential drops that occur from the surface to the bulk solution in the Gouy-Chapman-Stern model. By doing so he was able to write an expression for the total capacitance of the interface and showed that the resulting equation followed the same form as that of two capacitors in series[31].

It should be noted that the physical solid-liquid interface does not include four separate layers or sheets of charge that one would expect to be present when two capacitors are configured in series in a circuit. In fact, all of the charge on the solution side of the interface resides beyond the OHP in the diffuse layer. The mathematics simply delivers a convenient expression that contains information about both the Stern and diffuse layers of the system. In the more simplistic Gouy-Chapman model there is a single term in the expression for the total capacitance. Figure 5.2 depicts the system with which the EDL can be modeled in the Gouy-Chapman-Stern framework. In this model, the total capacitance of the system, C_T, is given by

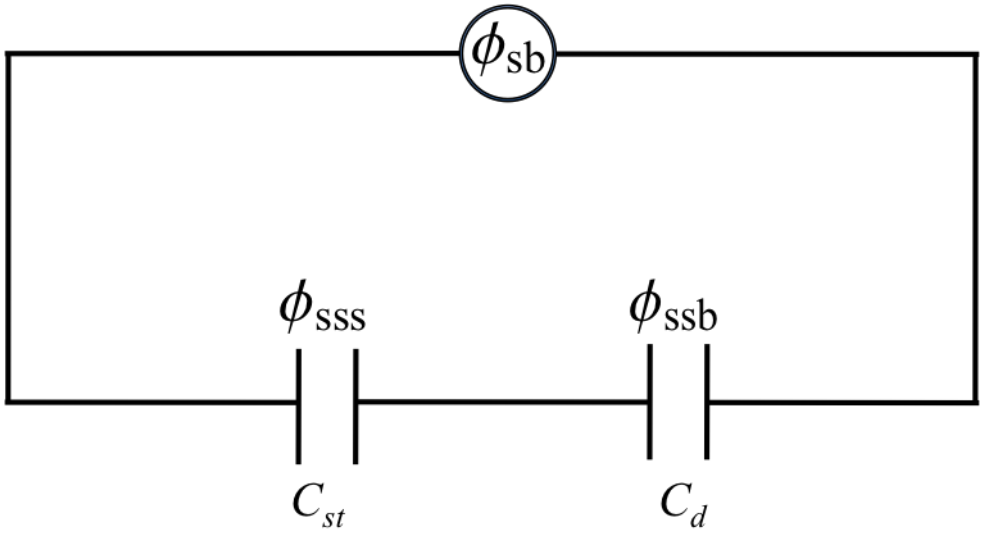

Figure 5.2: Schematic of the two capacitors in series model of the EDL system. C_{st} and C_d represent the capacitance of the Stern and diffuse parts of the EDL, respectively. ϕ_{sss} and ϕ_{ssb} are the potential drops across the Stern and diffuse layers, respectively. The physical solid-liquid interface does not contain two separate capacitive elements. All of the charge exists, instead, within the diffuse layer beginning at the OHP.

$$\frac{1}{C_T} = \frac{1}{C_{st}} + \frac{1}{C_d} \Rightarrow C_T = \frac{C_{st}C_d}{C_{st} + C_d}, \tag{5.3}$$

where C_{st} and C_d are the capacitances per unit area of the Stern and diffuse layers, respectively. In any capacitive system, the total charge accumulated within the system is a function of the potential difference between the two terminals. Similarly in an EDL system, the charge density, σ, on the solution side will be governed not by the applied potential, ΔV, directly, but by ϕ_{sb}, which is the total potential drop on the solution side of the interface. Therefore,

$$\sigma = C_T\phi_{sb} = C_{st}\phi_{sss} = C_d\phi_{ssb} \tag{5.4}$$

since capacitors in series have equal charges. Grahame showed that the charge density of the diffuse layer is given by

$$\sigma = \sqrt{8c_0\epsilon\epsilon_0\mathcal{R}T}\sinh\left[\frac{Ze\phi_{ssb}}{2kT}\right]. \tag{5.5}$$

Therefore, the capacitance of the diffuse layer can be written as

$$C_d = \frac{\sqrt{8c_0\epsilon\epsilon_0\mathcal{R}T}}{\phi_{ssb}}\sinh\left[\frac{Ze\phi_{ssb}}{2kT}\right], \tag{5.6}$$

where c_0 is the ionic concentration of the solution, ϵ is the bulk solution dielectric constant, $\mathcal{R}$ is the ideal gas constant, k is Boltzmann's constant, and T is the temperature. The capacitance of the Stern layer, which is assumed an ideal linear capacitor, is simply

$$C_{st} = \frac{\epsilon_{st}\epsilon_0}{d_{st}}, \tag{5.7}$$

where d_{st} is the thickness of the Stern layer, generally taken to be the radius of a hydrated ion and ϵ_{st} is the dielectric constant of the Stern layer, which has been shown to be smaller than the bulk value of 80, but often that value is used[17]. With this information known, we can relate all potential drops to the total potential drop

across the EDL, ϕ_{sb}, with

$$\begin{aligned} \sigma &= C_T\phi_{sb} = \sigma_{st} = \sigma_d \\ &= \frac{C_{st}C_d}{C_{st}+C_d}\phi_{sb} = C_{st}\phi_{sss} = C_d\phi_{ssb} \\ \Rightarrow \phi_{sss} &= \frac{C_d}{C_{st}+C_d}\phi_{sb} \\ \text{and} \quad \phi_{ssb} &= \frac{C_{st}}{C_{st}+C_d}\phi_{sb} \end{aligned} \tag{5.8}$$

Dividing these last two and solving for ϕ_{sss}, we get

$$\phi_{sss} = \frac{C_d}{C_{st}}\phi_{ssb} \tag{5.9}$$

The first relation in the series stems from the argument that capacitors in series will have equal charges. Plugging in the capacitance expressions, we get

$$\begin{aligned} \phi_{sss} &= \frac{\frac{\sqrt{8c_0\epsilon\epsilon_0\mathcal{R}T}}{\phi_{ssb}}\sinh(\frac{Ze\phi_{ssb}}{2kT})}{\frac{\epsilon\epsilon_0}{d_{st}}}\phi_{ssb} \\ &= \frac{\sqrt{8c_0\epsilon\epsilon_0\mathcal{R}T}\sinh(\frac{Ze\phi_{ssb}}{2kT})}{\frac{\epsilon_{st}\epsilon_0}{d_{st}}}. \end{aligned} \tag{5.10}$$

Therefore, with AFM measurements that yield values of ϕ_{ssb} at different applied ΔV's, it is possible to find a corresponding value of ϕ_{sss}, the potential drop across the Stern layer of the sample. A similar derivation could be carried out for ϕ_{psb} and ϕ_{pps}.

Furthermore, since ϕ_{ssb} is measured directly, it can be related to the potential of the bulk solution by

$$V_b = V_s - \phi_{sss} - \phi_{ssb}. \tag{5.11}$$

V_s is set during the experiment and ϕ_{sss} is inferred from (5.10) and hence V_b can be found for each fitted value of ϕ_{ssb}. Continuing even further, the relationships in (5.1) can be used to deduce a value of V_{ss}. In this way, the entire system can be characterized with respect to the same reference point (using the V's only), thus reducing the ambiguity in electrical coordinate systems that can proliferate in such measurements. In this process, a model for V_b is proposed and (5.11) can be used

to recalculate value of V_b using experimentally obtained data, effectively serving as a consistency check of the model.

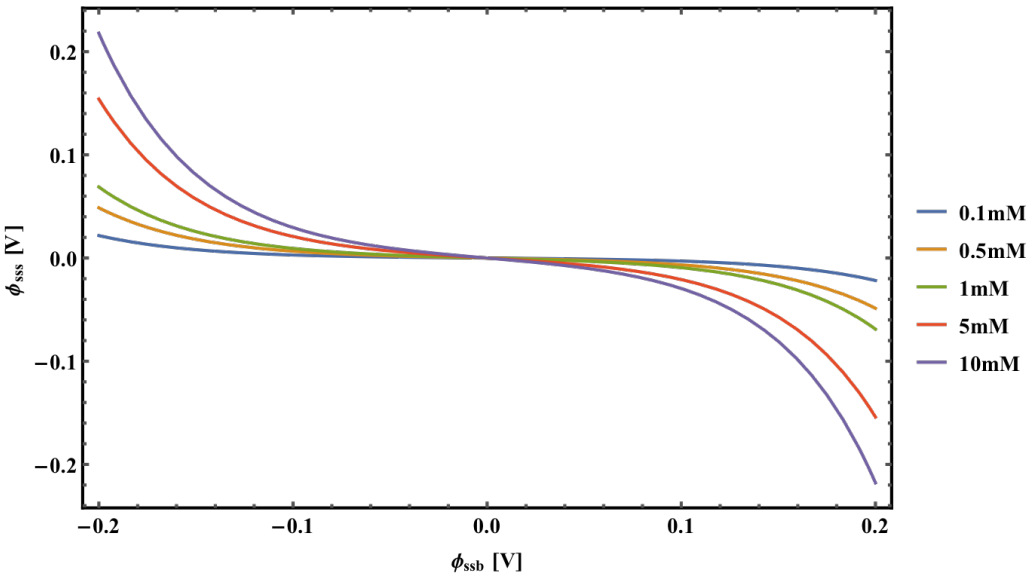

Figure 5.3: Relationship between the potential drops across the diffuse and Stern layers according to (5.10). The different curves represent (5.10) evaluated for various solution concentrations. The dependence of the potential drop across the Stern layer on the diffuse layer potential drop increases with increasing solution concentration.

5.3 The Force Due to Double Layer Interactions

An important assumption of this model is that the force due to double layer interactions between surfaces is proportional only to the diffuse layer potential drop. Under this assumption, a force expression similar to that derived by Lin et al. can be rewritten in the new nomenclature as[53]

$$F = \frac{4\pi\epsilon\epsilon_0 R\phi_{psb}\phi_{ssb}\exp[-\frac{z}{\lambda}]}{\lambda}. \tag{5.12}$$

Here, R is the colloidal probe radius. Because the model declares that the bulk potential can shift during an experiment according to (5.2), care must be taken to account for this shift as it propagates into the values of other parameters. Most importantly, a shifting bulk potential implies that the value of ϕ_{psb} is not constant.

Given the relationships of (5.1) and (5.2), it can be shown that

$$\phi_{psb}(\Delta V) = \phi_{psb,0} - \frac{\Delta V}{2}, \tag{5.13}$$

where $\phi_{psb,0}$ is the value of ϕ_{psb} measured at no applied bias ($\Delta V = 0$).

The introduction of a more descriptive nomenclature has not changed the fact that this equation is degenerate in the two potential values, ϕ_{psb} and ϕ_{ssb}. Therefore a fit to data of the measured force cannot be trusted to produce reliable values of both potentials simultaneously. Still present is the need for some sort of calibration in order to gain knowledge of one the ϕ's in order to fit force data for the other. Here is where one can implement the symmetric electrode scheme described earlier to reduce the number of fitting parameters by one. I refer to this as the "probe calibration" step of the measurement scheme.

5.4 Measuring Diffuse Layer Potential Drops With AFM: Probe Calibration

A measurement scheme complementary to the model of the EDL that I discussed earlier in this chapter has also been developed. In this scheme, the AFM probe is calibrated by using a particular probe-sample pair, which induces the type of symmetries employed by Montes Ruiz-Capello et al. mentioned in Section 4.4.2. The theoretical foundations of this work lie within the limits of the Gouy-Chapman and Gouy-Chapman-Stern models of the EDL. There is no consideration given to the finite size of ions other than those within the compact layer. The medium is considered to be a uniform dielectric with dielectric constant $\epsilon = 80$ up to the Stern layer, where the dielectric constant drops to a lower value (10 in this work). The veracity of the Gouy-Chapman-Stern model will be discussed later in this chapter. Let us begin by first laying out the framework of the analytic model that has been derived.

This section outlines the general process for making AFM measurements that can be used as a calibration of the probe in terms of its diffuse layer potential. Typically, gold or platinum AFM probes are used for electrostatic measurements because they are inert for relevant environmental and experimental conditions. They are close to ideal polarizable electrodes, meaning current does not easily flow across the solid-liquid interface and they also have little specific chemistry with most salts. Therefore, if we have a gold-coated probe, we can similarly coat a planar sample. From the perspective of an ion in solution, a sphere with an approximately 5 μm radius and a planar sample are both infinite planes. The potential profiles of such a situation are given in Figure 5.4. The symmetry that this creates reduces (5.12) to

$$F = \frac{4\pi\epsilon\epsilon_0 R\phi_{psb}^2 \exp[-\frac{z}{\lambda}]}{\lambda}. \tag{5.14}$$

Looking at (5.14), it is evident that a fit of the force for a value of ϕ_{psb} will yield only the magnitude of the potential since the fit parameter is actually ϕ_{psb}^2.

How can we deduce the sign of the potential difference? It is known that different surfaces gather particular charges at given pH conditions. The value of the pH at which no charge gathers on a surface is known as the isoelectric point (IEP). At pH values above the IEP, surfaces will obtain net negative charges and positive ones at values below the IEP. This is because the pH is a measure of the ratio of positive hydrogen and negative hydroxide molecules. Higher pH values indicate a higher ratio of hydroxide ions in solution, which will result in more negative charges being driven toward the surface. Given that the IEP of gold is known to be between 3 and 4, its surface charge state and hence sign of the diffuse potential drop can be found at any pH[6]. For instance, at a pH of 7, the diffuse layer potential drop will be negative.

The choice of which surface receives the calibration is arbitrary, but in general, it is more useful to calibrate the probe. With a fully calibrated probe, it is then possible to measure the diffuse layer potential drop of any surface.

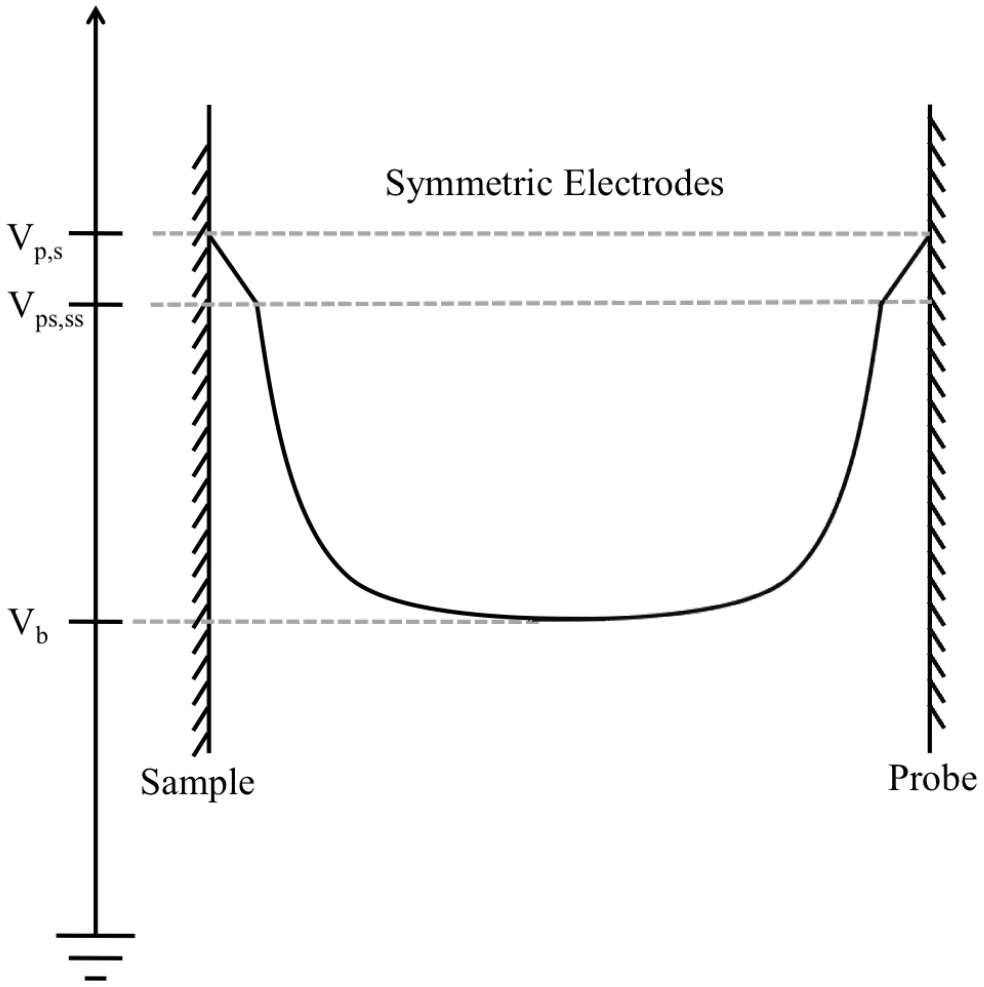

Figure 5.4: The potential profile for the symmetric electrode case. The drops across each region are the same in magnitude on either solid-liquid interface. The initial, linear potential drop from the probe surface represents ϕ_{pps} and that from the sample surface represents ϕ_{sss}. The exponential drops that occur thereafter represent ϕ_{psb} and ϕ_{ssb}.

5.5 Assumptions of the Model

Several assumptions have been made in the construction of this analysis, which merit discussion. First, it was stated earlier in this chapter that the flow of currents across the interface will affect the value of the bulk potential, a characteristic of the system we wish to deduce. The two most functionally important classes of currents in experiments of this kind are Faradaic and non-Faradaic currents.

Faradaic currents occur when chemical reactions are catalyzed at or near the inter-

face and electrons "hop" from a chemical species in solution through the electrode or from the electrode through to the solution. The chemical reactions in electrochemical experiments take the form of reduction and oxidation of electroactive species within the solution itself. In the model proposed here, it is assumed that there are no Faradaic currents. That is, no chemical reactions take place at the interface that would cause charge to flow from the electrode to the solution or vice versa. Is this reasonable? In a typical electrochemical experiment, these Faradaic currents are the currents that are of interest to the researcher. Our experiments are carefully designed, however, to avoid such currents.

For experiments done with this model in mind, we, by design, have no such electroactive species at the potentials applied to the electrode. More specifically, we typically measure dilute electrolytes such as NaCl of KCl or KNO_3, etc. The chemical species within these salts are known to have higher reduction/oxidation potentials than the water in which they are dissolved. For instance, it is known that the reduction potentials of Na^+ and K^+ are -2.71 V and -2.92 V vs. a Standard Hydrogen Electrode (SHE), respectively. For comparison, water molecules are reduced at -0.83 V vs. SHE. As for anions, the oxidation potentials of Cl^- and NO_3 are -1.36 V and 0.8 V vs. SHE. Water molecules are oxidized at -1.23 V vs. SHE. Since the Cl^- atoms and water molecules have similar oxidation potentials, both Cl_2 and O_2 gases can be produced at the anode, but only at that applied voltage, which is well above those used in these experiments.

In practice, our experiment will never apply potentials above a few hundred millivolts, so we will catalyze no reactions and produce no Faradaic currents. This assertion can be tested with relative ease. To do so, cyclic voltammetry measurements were carried out using a modified AFM system. A CHI Instruments 620B potentiostat was connected to the AFM system such that a gold-coated sample surface and a gold-coated AFM probe acted as the working and counter electrodes, respectively,

while a platinum wire served as the reference electrode. Figure 5.5 shows the results from a typical CV measurement in 1 mM NaCl. The absence of any peaks in the curve in the region between 0 and +300 mV vs. Pt indicate that there are no chemical reactions or subsequent Faradaic currents at the interface. This type of measurement was performed before each set of AFM experiments as described below. This step also served as a method to ensure the purity of all prepared solutions as contaminants would alter the shape of the current vs. voltage profiles.

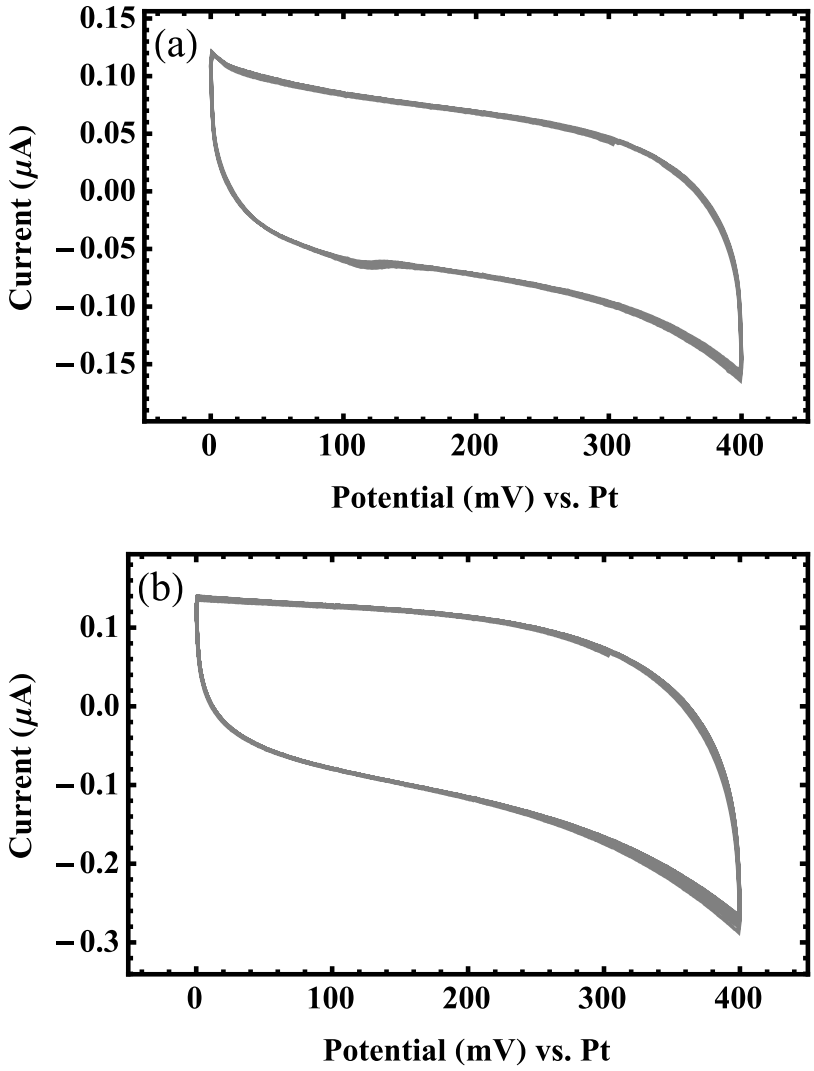

Figure 5.5: Cyclic Voltammograms of (a) 0.1 mM NaCl and (b) 1 mM NaCl solutions. The data indicate that no chemical reactions are being induced, and hence there are no Faradaic currents in the applied bias range of $0 - 400$ mV

As for non-Faradaic currents, they are not assumed to be zero, but their effect on the bulk potential is negligible. Non-Faradaic currents are those in which the source of current is the flow, migration, or reorientation of charges to form the double layer or alter its capacitance. For this reason, these currents are often also referred to as "double layer currents", "charging currents", or "capacitive currents". When non-Faradaic currents are present, charge does not cross the interface, but external currents can still flow. What effect may these currents have on the bulk potential? Consider a system very similar to one used in the experiments performed in this work. In such systems, a roughly 1 cm^2 sample surface is immersed in roughly 100 μL of a 1 mM 1:1 salt solution. Within the solution, there are roughly 10^{16} of Na and Cl ions each, assumed to be equally distributed throughout the solution in the initial state. Hence, the total charge in the solution phase is 10^{-1} C. Typical measurements of surface charge densities at electrified interfaces are on the order of mC/m^2, or approximately 10^{-7} C spread over the entire sample surface[36, 47, 71, 73]. If one considers a spherical Gaussian surface of radius r within the bulk solution and calculates the potential, V, of a point within that region with respect to a point infinitely far way, this is an analogous calculation of the bulk solution potential. Doing so for the potential before, $V_1 = \frac{kQ_1}{r}$, and after, $V_2 = \frac{kq_2}{r}$, the double layer is formed yields $\frac{V_2}{V_1} = \frac{Q_2}{Q_1} = \frac{Q_1 - \Delta Q}{Q_1}$, where k is the Coulomb constant and ΔQ is the charge that moves to the surface from the bulk. With the values listed above, this yields a fractional change in the bulk solution potential of 10^{-6}. This is clearly a negligible change in the potential of the bulk solution and so it can be approximated as constant under the migration of charge to the surface.

Under the assumption of no Faradaic currents being present and that the presence of non-Faradaic currents will not affect the value of the bulk potential, its value can be found via (5.2).

The next assumption holds that only the diffuse layer contributes to the force

due to double layer interactions. Why is this? In the model of the system we have adopted, the region of space between the surface and OHP (Stern layer) contains no charge. In this region, a linear potential drop occurs, and it is this potential we wish to probe. The charges of the Stern layer exist at the OHP. An application of Gauss' Law to the probe, assumed to be spherical, shows that the it can be treated as a single point charge located at the sphere's center with a magnitude equal to the net charge on its surface. A Gaussian surface that encompasses only the charges in the Stern layer will encompass the net charge on the probe. In the absence of specific adsorption at the surface, this is zero. Hence the force between it and any other charge distribution such as the one on the sample surface, also with a charge-free region out to the OHP, is zero. In this way, we can declare that the Stern layer of charges do not contribute to the measured force. Therefore, all of the force is from the interaction of the two diffuse layers of charge and the force expression can be fit with data to yield values of the diffuse layer potential drop.

5.6 Measurement Simulation: Error Analysis and Propagation

In order to know to what extent the particular fitting algorithm that was designed could be trusted, a series of simulations were performed. Essentially, the force model of (5.14) was used to simulate a large number of individual force measurements with varying degrees of noise in two separate experimental variables, the probe-sample separation, z, and the measured force, F. The uncertainty in z could stem from imperfect calibrations of the piezoelectric positioning devices, mechanical vibrations, or simple voltage resolution issues from the main power supply. Uncertainty in the measurement of forces can come from errors in cantilever spring constant calibration, contributions from forces not considered in a given interaction model, or positional

uncertainty in the reflected laser beam.

Multiple different experiments were performed to test the uncertainty of force measurements. First, a simple calculation was done using standard error propagation techniques to at least understand the order of magnitude of uncertainty in measurements of potentials given uncertainties in z and F. Since (5.14) can be rearranged to show that the potential, ϕ is a function of the force, F and the position, z, the uncertainty in ϕ is given by

$$\sigma_\phi = \sqrt{\left(\sigma_F \frac{\partial \phi}{\partial F}\right)^2 + \left(\sigma_z \frac{\partial \phi}{\partial z}.\right)^2} \tag{5.15}$$

Rearrangement and differentiation of (5.14) yields

$$\begin{aligned} \frac{\partial \phi}{\partial F} &= \frac{\lambda \exp[\frac{z}{\lambda}]}{8\pi\epsilon_0\epsilon_D R\phi} \quad \text{and} \\ \frac{\partial \phi}{\partial z} &= \frac{\phi}{2\lambda} \end{aligned} \tag{5.16}$$

Although this exercise illuminates the order to which error may propagate through a measurement, it is not empirical in nature. To further understand the scale of error propagation as well as the sensitivity of the fitting algorithms used, force measurements were simulated assuming the force was given by (5.14). In this series of tests, simulated force measurements were generated with the uncertainty in z and F ranging from 0.1 to 5 nm and 0.01 to 0.6 nN, respectively. These values are generated from a heuristic understanding of the measurement system and the sources and magnitude of noise encountered in a typical measurement. As real measurements take place over a range of approximately 100 nm and the exponential decay takes place over approximately 30 nm, the simulated uncertainty in z is roughly equivalent to a 15% error. The simulated errors in F are as high as 30%. The noise inserted into the simulation is Gaussian in nature. Gaussian noise was chosen because it is known that most noise in electronic circuits has at least a Gaussian component. Gaussian noise sources in real systems include shot noise, thermal noise, or electromagnetic interference from external sources.

In this series of tests, 100 individual measurements were simulated at each noise level pair. In total, 11 noise level values in z were implemented along with 12 noise levels in F, for a grand total of 132 combinations. The potential parameter, ϕ was set to 50 mV for both series of tests. This value was chosen as it is approximately an average value of many experimental measurements of the diffuse player potential of various surfaces in standard electrolyte solutions. Other values were also tested with similar results.

Figure 5.6 depicts the results of fitting simulated data with Gaussian noise in both the position and force variables to (5.14). The fitting algorithm continues to fit the data well even with high levels of noise in both the probe-sample distance and the force.

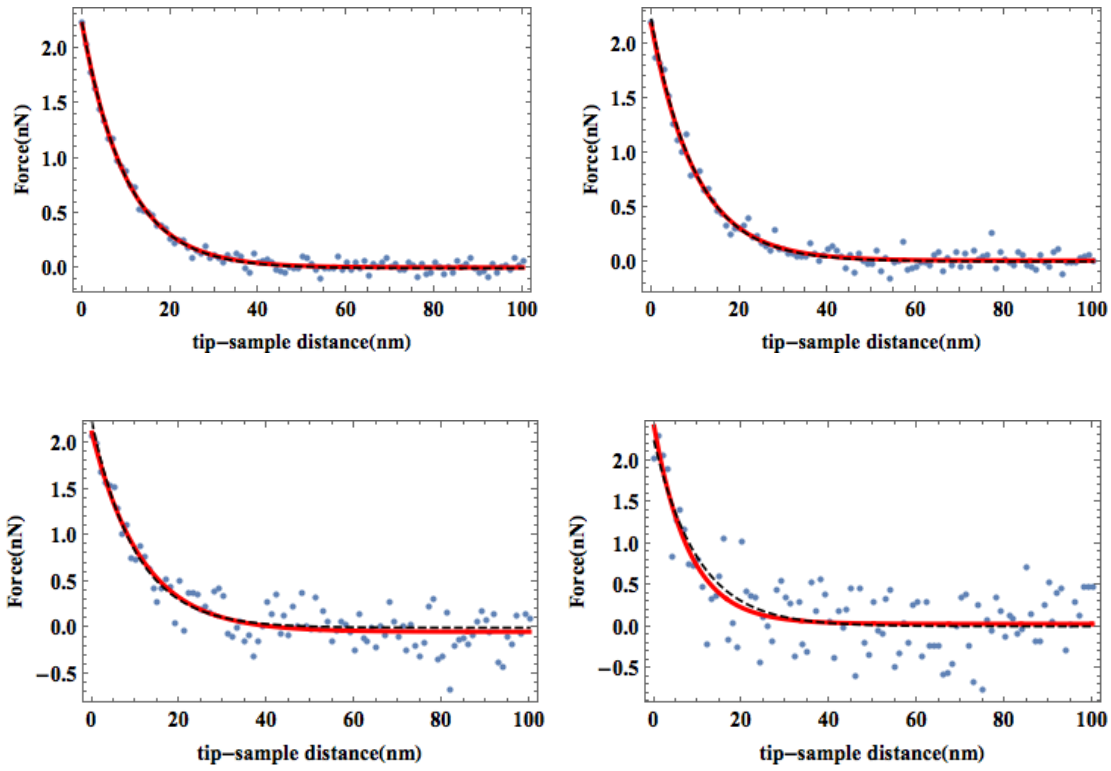

Figure 5.6: A selection of simulated force measurements with increasing amounts of Gaussian noise added to the system. Each simulation has noise added to both the probe-sample distance, z, and the force, F. The red lines represent fits to the simulated data (blue circles) to (5.14) with the fitting algorithm used for real experimental data. The black dashed line represents function used to generate the noisy data. The fits yielded R^2 values of (from left to right) 0.974, 0.972, 0.864, 0.680

Trial	z-noise (nm)	F-noise (nN)	R^2
1	0.8	0.07	0.974
2	0.9	0.8	0.972
3	4	0.2	0.864
4	9	0.4	0.680

Table 5.1: A selection of results of performing fits of (5.14) to simulated experimental force measurements. As expected, the larger noise in both z and F resulted in lower R^2 values.

Figure 5.7 shows the results of plotting the average value of ϕ found by fitting the simulated data in exactly the same way as done in real experiments. All constraints and variables are input to the algorithm in the exact fashion as when fitting real experimental data. In all cases, R is known from previous measurements as outlined in Section 5.7 in and λ is also known from (2.19). Table 5.1 shows a condensed description of the simulation parameters and the associated R^2 values.

Statistical analysis of the subsequent fits of the simulated data to (5.14) was performed to obtain average and standard error values of each simulated measurement. The black vertical lines in Figure 5.7 represent the standard error of the fitting for each noise combination. In this context the standard error is defined as $\sigma_\mu = \frac{\sigma}{\sqrt{N}}$, where σ is the standard deviation and N is the number of trials.

The fit algorithm produced values of ϕ that deviated by no more than 15% for values of ϕ that ranged from 10 mV to 150 mV.

5.7 Reproducing Previous Results

Because the measurements and analysis described in this work are a departure from standard practice, it is of great importance to ensure that results obtained from them can be trusted. In the following three sections, I will lay out a series of experiments that were used to ensure that both our measurement system as well as the analytical framework I developed produce results consistent with those obtained in previous

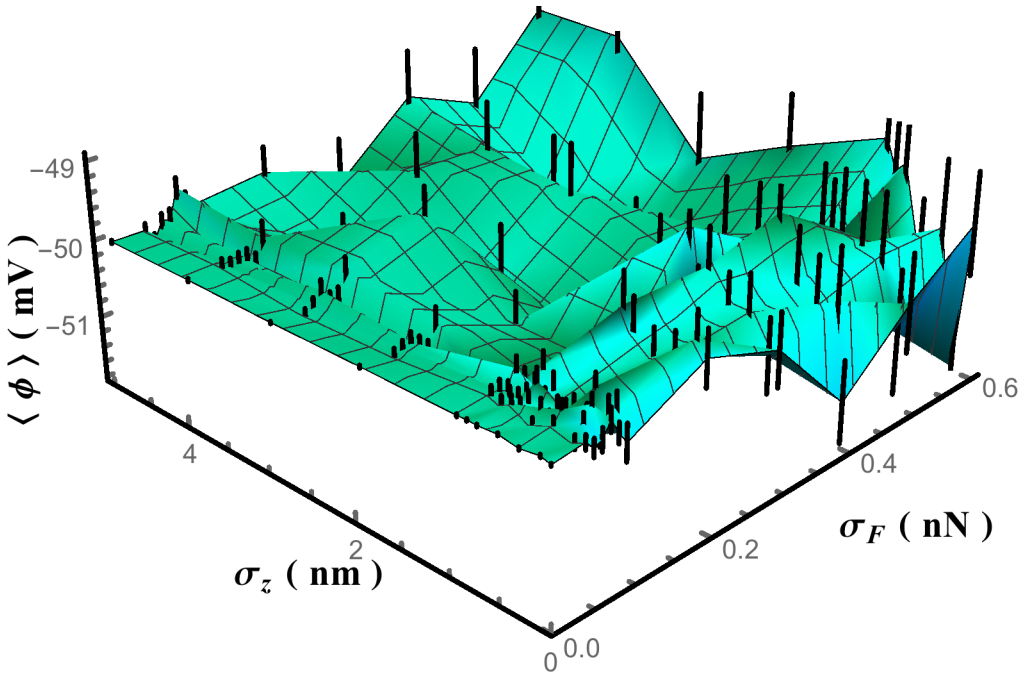

Figure 5.7: Results of performing fits for the value of ϕ with varying noise levels in z and F. During the simulations, the potential, ϕ was set to 50 mV. The data indicates that, as expected, the fitting algorithm tightly constrains the value of ϕ for low levels of noise. As the noise level increases in either z or F, the error in the fitting increases. The algorithm appears more sensitive to F than z. The black lines indicate the standard error of the mean for fitted values of ϕ over 100 trials.

studies.

5.7.1 Materials and Methods

All AFM measurements were carried out using a commercially available AFM from Nanotec Electronica with a complementary Dulcinea digital control and high voltage power supply unit. In cases when external biasing was employed, a Keithley 6430 Sub-Femtoamp Remote source measure unit was connected to the system as necessary. Colloidal probes used in these measurements were obtained from AppNano (FORT-TL-A-5).

Aqueous electrolyte solutions were prepared using reagent grade salts dissolved

in deionized (DI) water obtained from an in-house system. The resistivity of the DI water was > 17.4 MΩ·cm.

Gold samples and gold-coated cantilevers were prepared via thermal evaporation. The samples began as 1 cm^2 V1 grade mica discs from Ted Pella (Prod #50). The mica was mechanically cleaved immediately prior to the evaporation process.

The radius of the probes, R, was measured by way of the method of Neto et al.[56]. The probes were removed from packaging, cleaned, and scanned over a TGT1 grating purchased from NT-DMT. Topographical images of the grating were recorded and analyzed. The radius was obtained via profilometric analysis of the topographical data. Results of the profilometric scanning of the grating are shown in figure 5.8(a). Figure 5.8(b) was obtained by plotting the data from every point along the line in Figure 5.8(a). The radius was calculated via

$$R = \frac{H^2 + \left(\frac{W}{2}\right)^2}{2H}, \tag{5.17}$$

where H and W are defined as the height and width, respectively, of the profilometric curves obtained by scanning the TGT1 grating.

The first step to confirming the veracity of the newly proposed experimental and analytical system discussed earlier was to reproduce results from several previous studies on similar systems using the same techniques. Each of these studies involved biasing either the probe or sample, measuring forces, and extracting values of the diffuse layer potential drop.

Because my experiments involve two-electrodes (probe and sample), which are connected to a common power supply, with no reference electrode in place, I first performed tests in which the sample was the only electrified component in the system. The probe was insulating silica and remained isolated from the electrical circuit of the sample, reference electrode, counter electrode, and power supply. Next, I made measurements using an isolated metallic probe, now with only a reference electrode

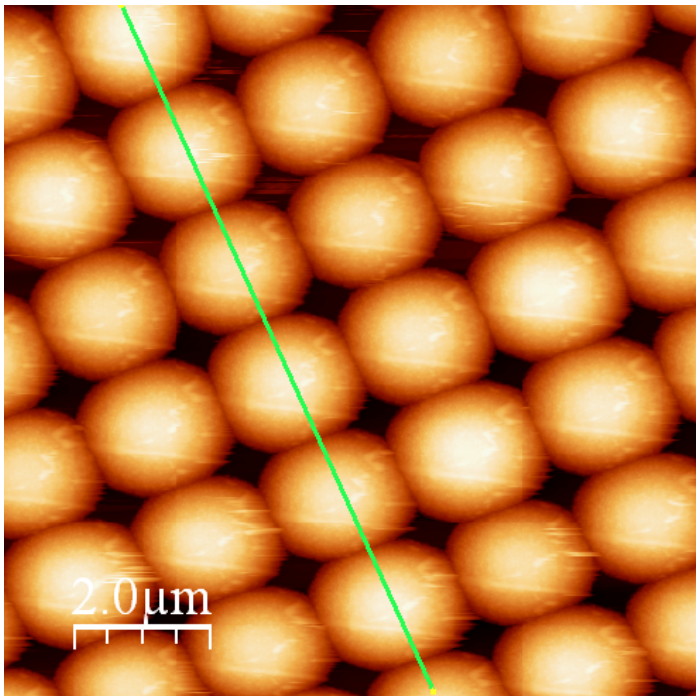

(a)

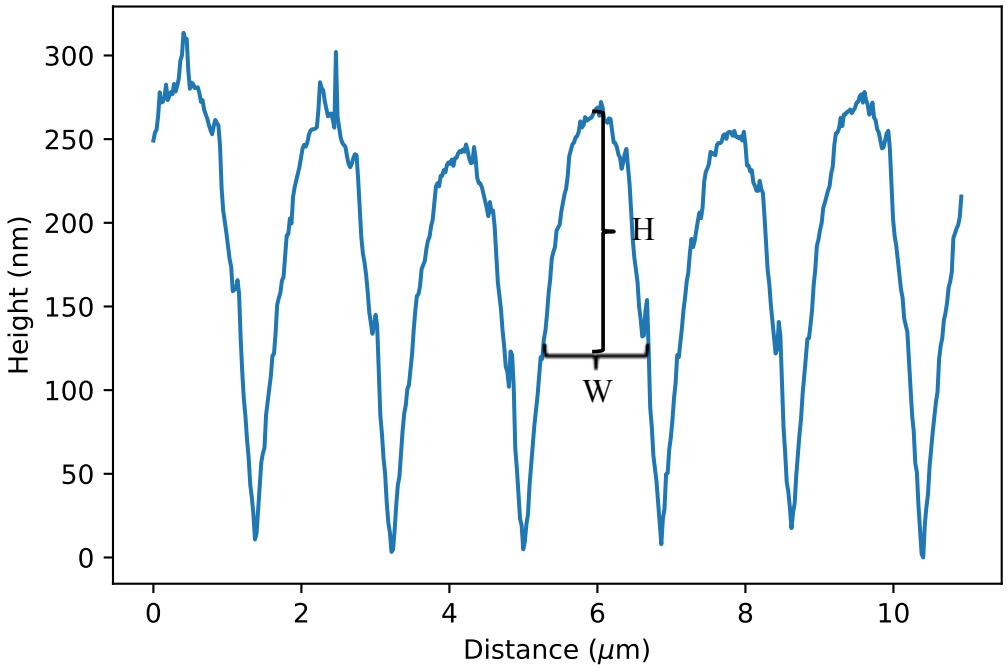

(b)

Figure 5.8: (a) Topographic image obtained by scanning a TGT1 grating with a colloidal probe. The height profile seen in (b) is obtained by plotting the points that lie along the green line in (a). The data from the profile is used to calibrate the radius of the spherical probe via (5.17).

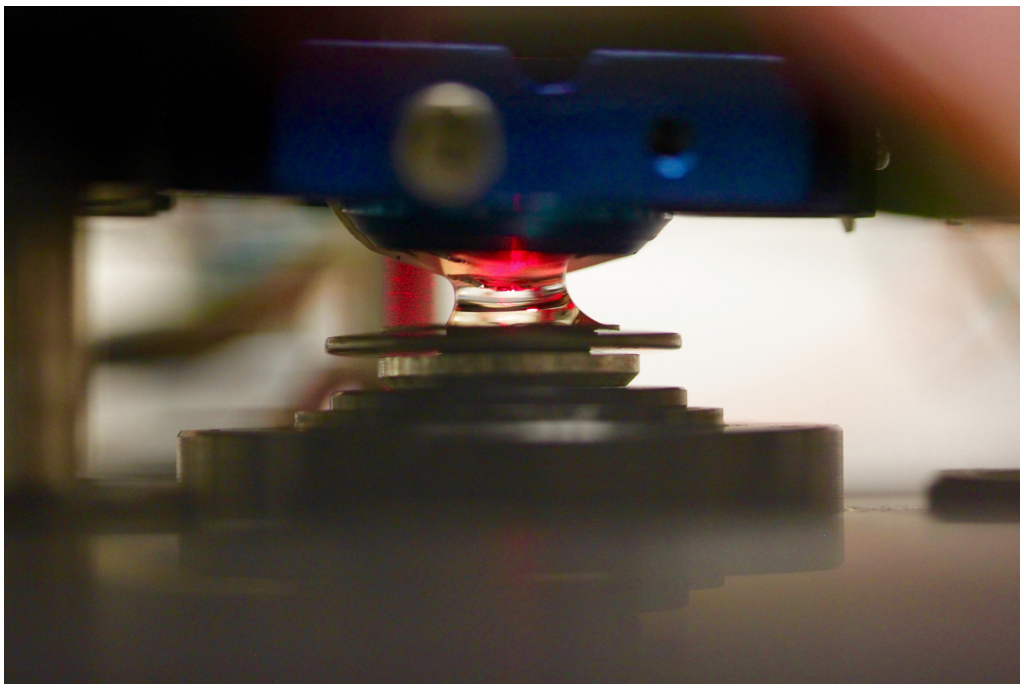

Figure 5.9: A photo of a typical AFM experiment within a liquid environment. The water meniscus can be seen clearly. This meniscus begins from below at the sample surface and terminates above on the holder in which the cantilever/probe rests. Typical measurements are made in approximately 100 μL of solution. The small amount of liquid compared to similar larger scale measurements demands that consideration must be given to the effects of electrical biasing on the liquid itself.

inserted into the system to understand the effects of a metallic probe in these systems. Finally, the two-electrode measurements consisting of only an electrically connected probe, sample, and power supply were made.

5.7.2 Isolated Silica Probe

The first test was carried out using a silica colloidal probe, a gold sample surface, and a platinum reference and counter electrode, all immersed in a 1 mM KNO_3 solution as done in the work of Barten et al. [6]. The variation in forces between the probe and sample were measured as a function of sample biasing with respect to the platinum reference electrode. Figure 5.10 shows the results for one of the tests of this type. The results indicate that biasing the sample between -400 mV and $+400$ mV vs. Pt,

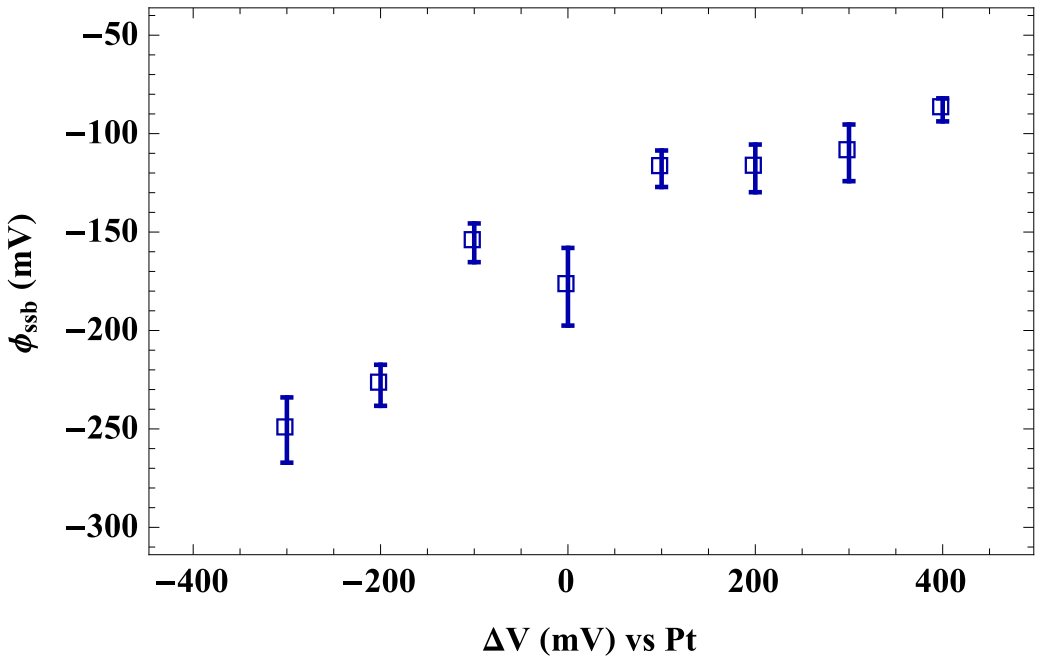

Figure 5.10: Measured diffuse layer potential drops for a gold surface in 1 mM KNO_3. The measurements were made using a silica probe and a platinum reference/counter electrode. The diffuse layer potential of the silica probe was assumed to be −45 mV[29]. These results demonstrate that our measurement system and analysis of the forces yield results that are consistent in the nature of the response of the system with those in literature[6].

leads to a diffuse layer potential drop that shifts by approximately 150 mV. These results are in good agreement with the results of Barten et al. One major deviation from those results, however, is the lack of a change in the sign of the force. Barten et al. observed a switch from repulsive to attractive forces as the sample was driven to more positive potentials. As noted in Chapter 4, there is some lack of reproduction of this result, with some groups reporting a change in force sign while others do not. A possible explanation for this lies in the fact that the bulk solution potential with respect to machine ground may differ by hundreds of millivolts in different labs and on different days. For this reason, one may not be able to drive an electrode to a potential high or low enough to overcome this offset potential. One advantage of the model I have developed is that this factor is accounted for by default.

5.7.3 Isolated Metallic Probe

The next set of tests performed involved replacing the silica probe with one coated in gold. The probe, although now conductive, was left isolated from the biasing circuit. Again, a platinum wire was used as a reference electrode. The experiments in this case were carried out in 1 mM NaCl.

Once the force measurements had been made, the data was analyzed under two differing assumptions. In the first analysis, the bulk potential was assumed to be constant. This is the equivalent of what all other studies up to this point have used. Under this assumption, the bulk solution potential is a point of constant reference for the diffuse layer potential and all other in-solution potentials. In the second analysis, the bulk potential was assumed to shift according to (5.2). Figure 5.11(a) shows the resulting calculations of the diffuse layer potential drop assuming a constant bulk potential. Under this assumption, the diffuse layer potential drop seems independent of the applied bias potential. However, Figure 5.11(b) shows that the assumption of a shifting bulk potential in the analysis yields values of the diffuse layer potential drop that themselves shift in a similar fashion. That is, they vary roughly linearly up to an applied bias of about 100 mV.

As with the isolated silica probe measurements, it can be seen that the force and hence measured diffuse layer potential drop increases up to applied bias values of $\Delta V \approx 100$ mV. That range of the increase in the diffuse layer potential agrees with this in literature for similar applied bias ranges[6]. I presume any difference in magnitude is attributed to the offset bulk potential, V_0, which can vary from solution to solution and experiment to experiment.

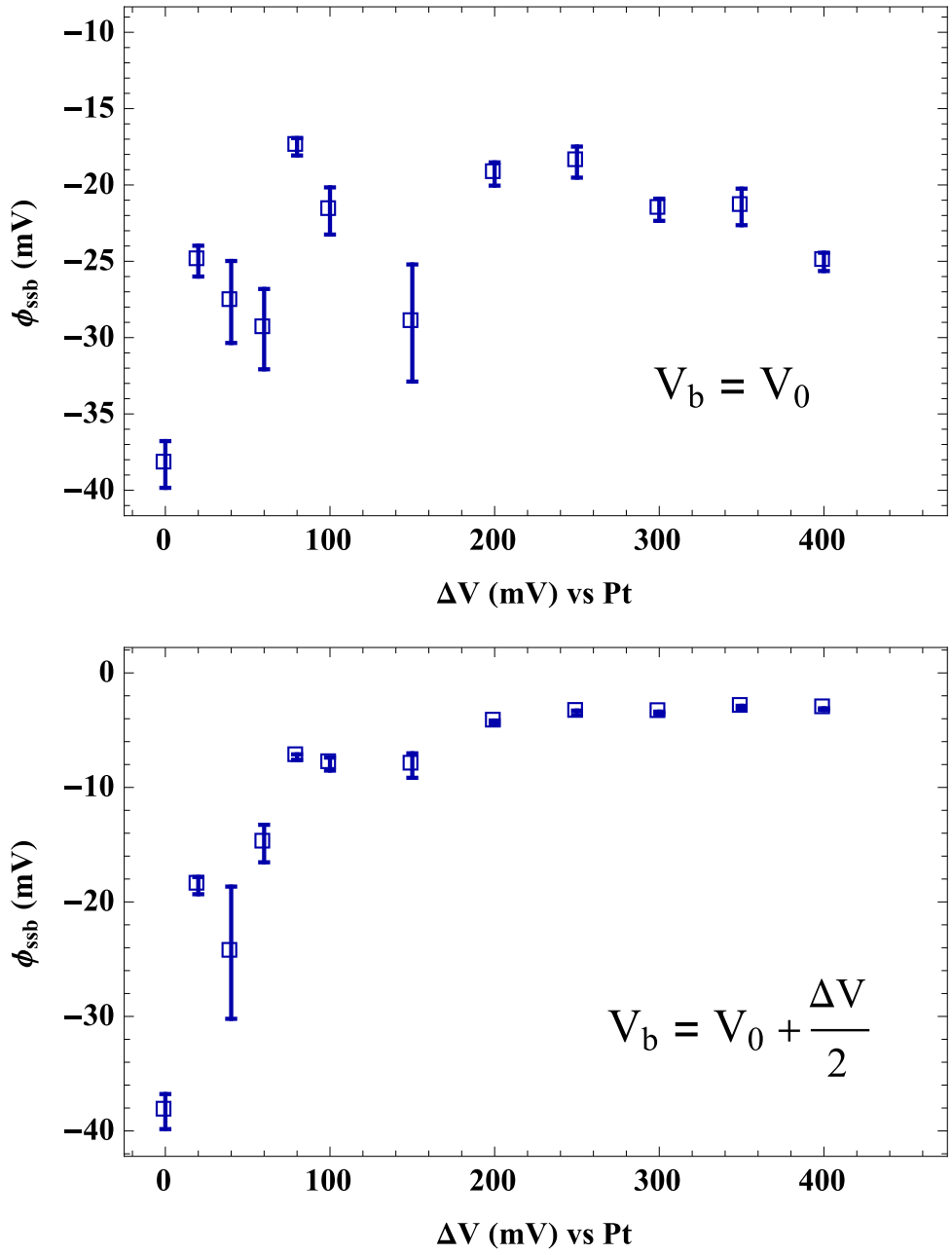

Figure 5.11: Calculated values of diffuse layer potential drops for a system consisting of a gold sample, an electrically isolated gold probe, and a platinum reference electrode in 1 mM NaCl over a range of applied sample biases. The underlying force data was analyzed under the assumption that (a) the bulk potential remains constant throughout the measurement and (b) the bulk potential is some constant offset plus $\Delta V/2$. The model of a constant bulk potential yields values of the diffuse layer potential drop that are independent of the applied bias. All previous work in the field indicates that this is not a reasonable result. The model of a shifting bulk potential yields the expected linear response of the diffuse layer potential drop to the applied bias up to $\Delta V = 100$ mV, after which some saturation occurs. Saturation of this type has been observed in similar systems[3, 12, 25].

5.8 Two-Electrode Measurements of EDL Potentials with AFM

Knowing that that AFM measurement system produces reasonable results, the final step in the series of measurements was to perform true, two-electrode measurements of solid-liquid interface systems. All measurements were performed in symmetric (1:1) salt solutions, typically NaCl or KCl. Measurements were carried out using a gold coated probe and gold sample where the probe was connected to the ground of the power supply and the sample was biased. No third electrode was present. In this scheme, the bias potential is applied directly between the probe and sample. It is known that the nanoscale morphology of the probe and sample can have an effect on the EDL that forms at either interface [38, 44, 62]. It is also known that surface morphology varies among coating and fabrication processes [15, 65]. For this reason, the probe and sample were coated with approximately 100 nm of gold within the same deposition process. Typically this process was thermal evaporation, although electron-beam depositions were sometimes used as well. In any case, it was important that the two surfaces be as chemically and physically similar as possible to induce the highest degree of symmetry possible so that calibration measurements could be made and fit according to (5.14).

Again, the force between the probe and sample was measured as a function of applied biases to the sample. Similarly to the previous set of experiments, analysis was performed with the two basic assumptions about the nature of the bulk solution potential. Figure 5.12 depicts the variation in the measured forces as a function of applied sample bias.

Once again, it can be seen that the force and hence measured diffuse layer potential drop increases up to applied bias values of $\Delta V \approx 100$ mV. The range of the increase in the diffuse layer potential agrees with those in literature for similar applied bias

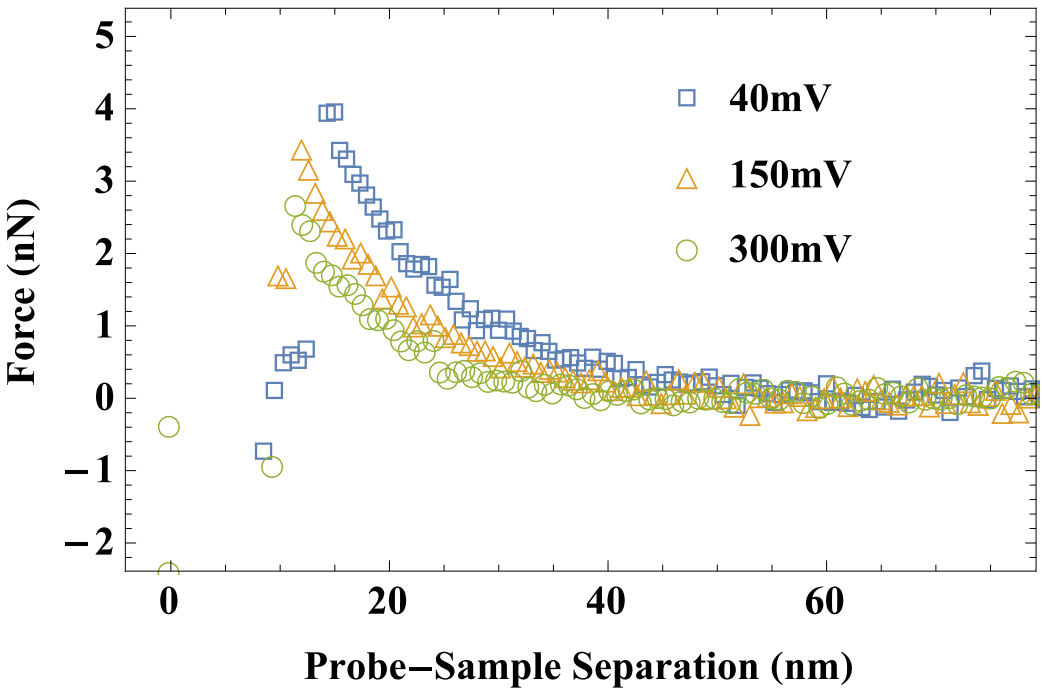

Figure 5.12: Force versus probe-sample separation curves for a gold probe and gold sample in 0.1 mM NaCl at various applied sample biases. There is a clear dependence of the force on the applied bias potential. Only every sixth data point is shown for clarity.

ranges[6, 25]. Any difference in absolute magnitude is attributed in this work to the offset bulk potential, V_0, which can vary from solution to solution and experiment to experiment.

As was done previously, the measured forces were used to calculate the diffuse layer potential drops. Figure 5.13 illustrates the measured diffuse layer potential drops, ϕ_{ssb}, for solutions of NaCl at three different concentrations. Because the previous analysis showed that it is most reasonable to assume that the bulk solution has a bias potential-dependent component, the analysis used to calculate these values was done using only that assumption.

Using the value of the diffuse layer potential drop, ϕ_{ssb}, calculations of ϕ_{sss} were carried out according to (5.10). Typical calculations of ϕ_{sss}, are depicted in Figure 5.14. With both ϕ_{ssb} and ϕ_{sss} known, the value of V_b was recalculated according to (5.11). Since each surface is treated separately, the bulk potential value with respect

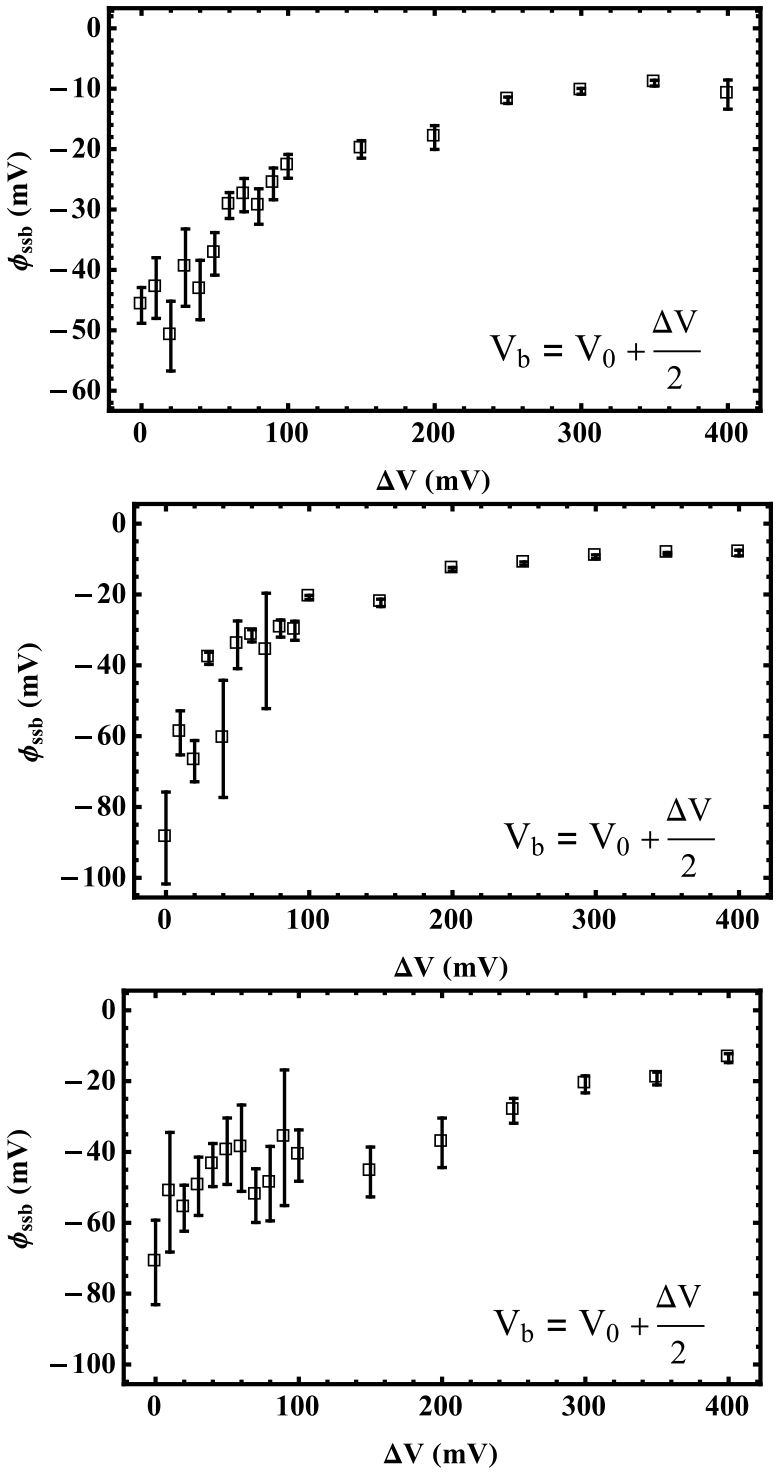

Figure 5.13: Calculated values of diffuse layer potential drops for a system consisting of a gold sample and gold probe in (a) 0.1 mM and (b) 0.5 mM and (c) 1 mM NaCl over a range of applied sample biases. The bias is applied directly between the sample and probe. Diffuse layer potential drops were calculated assuming the bulk potential is $V_b = V_0 + \Delta V/2$, yielding the expected linear response of the diffuse layer potential drop to the applied bias for $\Delta V < 100$ mV.

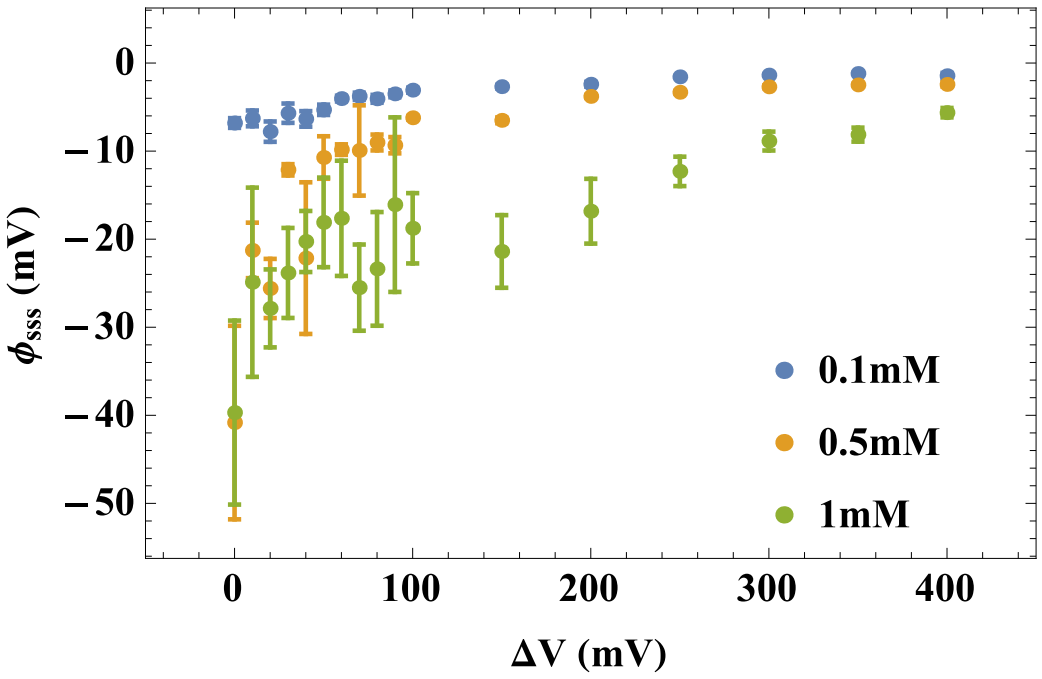

Figure 5.14: Calculated values of the potential drop across the Stern layer of the sample surface, ϕ_{sss}, assuming a shifting bulk potential. The values of the Stern potential are higher for the higher concentration, consistent with the notion of a more completely filled Stern layer.

to either electrode can be calculated.

This last step serves as a self-consistency check of the model. That is, by assuming that the bulk potential varies with applied bias according to (5.2), the analysis provides a way to then recalculate the value of V_b after calculating the two in-solution potential drops under the assumption that the bulk potential varies in that way.

Finally, it is now possible to plot the potential at every spatial point of interest within the system as a function of applied bias. Importantly, every potential can be plotted on a single axis, with a single common reference or ground point. The results of doing so are shown in Figure 5.15. It can be seen that up to $\Delta V \approx 100$ mV, the bulk potential varies linearly with ΔV. Furthermore, within that range, the two values of the bulk potential as measured from either electrode are in fairly good agreement with one another, especially for the 0.1 mM NaCl solution. In the region above $\Delta V \approx 100$ mV, the data for the bulk potential as measured from the probe, V_{bp},

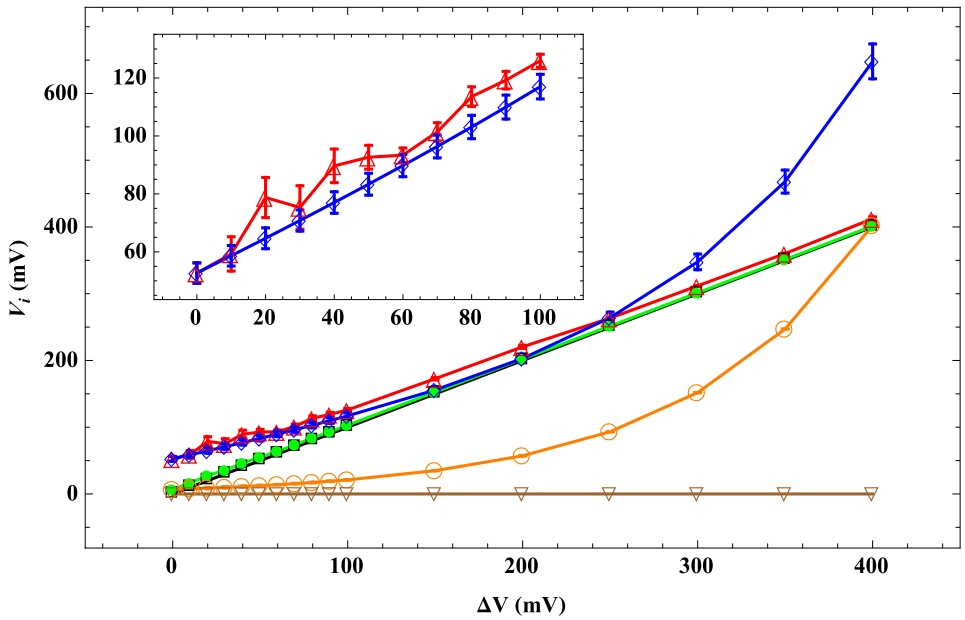

(a)

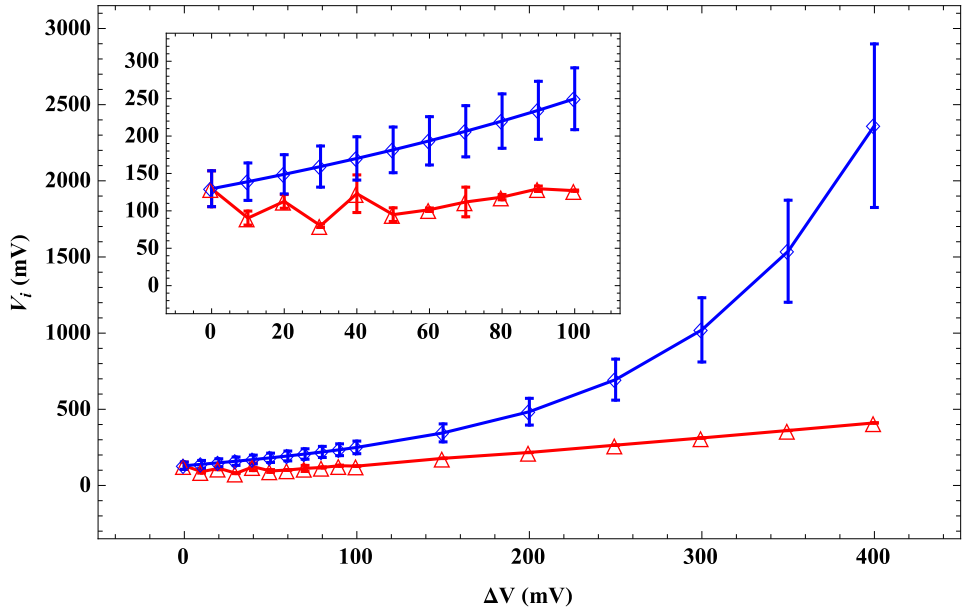

(b)

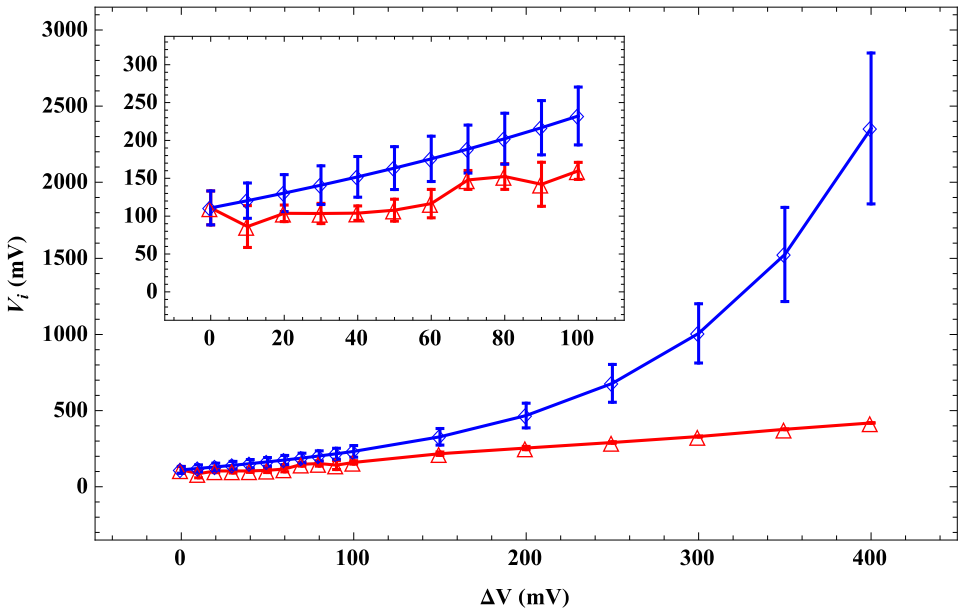

(c)

Figure 5.15: Calculated values for values of V_i, the potentials as measured from power supply ground. (a) shows each potential for the 0.1 mM NaCl solution. The list of potentials shown includes V_s, the sample potential, V_{ss}, the potential at the OHP of the sample, V_{bs}, the bulk potential as measured from the sample, V_{bp}, the bulk potential as measured from the probe, V_{ps}, the potential at the OHP of the probe, and V_p, the potential of the probe. The potentials are represented by open squares, filled circles, upright triangles, open diamonds, open circles, and inverted triangles, respectively. The inset of (a) shows the values of V_{bp} (open diamonds) and V_{bs} (upright triangles). (b) and (c) depict only the bulk potentials as measured from each electrode for the 0.5 mM and 1 mM solutions, respectively.

deviates sharply from the value of the bulk potential as measured from the sample, V_{bs}, and curves upward rapidly. This indicates a breakdown of the model for the bulk potential that was used to calculate this data. That is, the model's self-consistency breaks down at $\Delta V > 100$ mV. This is likely due to the onset of Faradaic currents, which will add charge to the solution side if the interface, thus shifting V_q from zero.

Chapter 6

Conclusions / Future Work

6.1 Conclusions

In this work, I have shown that it is possible to use AFM-based direct force measurements between simple surfaces to infer elusive electrostatic properties of the solid-liquid interface. The work I have presented can serve as a proof-of-concept series of measurements that open the door for many more nanoscopic measurements of interfacial systems. Furthermore, I have shown that a careful choice of reference point and nomenclature within the analysis of such force measurements can yield previously unobtainable insights into the nature of solution-side responses to applied electric fields.

The combination of model and measurement scheme was used on a system of a gold sample and a gold probe in various electrolyte solutions. Standard force measurements yielded values of the diffuse layer potential drop that agreed with those found in literature. These values were obtained only when the model of a bulk potential that varies with applied bias was used. These diffuse layer potentials were found to vary roughly linearly with applied sample bias up to 100 mV. The values of the diffuse layer potentials varied from -46 mV to -11 mV, -89 mV to -8 mV, and from -71 mV to -13 mV for the 0.1 mM, 0.5 mM, and 1 mM solutions, respectively, for applied biases ranging from 0 to +400 mV.

Using the diffuse layer potential drops, the potential drops across the Stern layer were calculated using a newly derived formula for the relationship between that po-

tential drop and the diffuse layer potential drop. The Stern layer potential drops were found to be a function of both solution concentration and applied bias as seen in previous research. The Stern layer potential drops were found to vary from -7 mV to -1 mV, -41 mV to -2 mV, and from -40 to -6 mV for the 0.1 mM, 0.5 mM and 1 mM NaCl solutions, respectively, for applied biases ranging from 0 to +400 mV.

Finally, using the known sample and probe potentials with respect to machine ground and the two potential drops described above, the bulk solution potential with respect to machine ground was inferred. This potential was also observed to shift with applied bias, as predicted by the model. The total shift above applied biases of 100 mV could not be fully accounted for by the model, however. Bulk potential offset values of 56 mV, 136 mV, and 108 mV were inferred using this process.

As I stated in the Introduction, the specific electrostatic characteristics of interfacial systems play a crucial role in many naturally occurring processes and thus these developments have a broad range of application in biology, chemistry, and engineering. Knowledge gleaned from these types of measurements can be particularly useful in the field of fuel cell engineering as the structure of the double layer greatly affects the charging and discharging of electrodes in both liquid and solid state fuel cell devices. For instance, application of (5.5) can yield the value of the surface charge density once the diffuse layer potential drop of the sample, ϕ_{ssb}, is measured.

The methods and analysis I have presented are particularly useful because of their simplicity. The use of standard consumer AFM's can lead to speedy, versatile, and stable measurements of this type on many different systems. Furthermore, the analysis can yield useful information about the sample surface, the solution itself, or the probe. The consideration of the response of the solution to external biasing in nanoscopic systems is the crux of this work.

6.2 Future Work

Interestingly, neither electrode need be biased to utilize the techniques I have presented in this work. It is still possible to infer the bulk solution potential as well as the diffuse layer potential drop and Stern layer potential drops. Measurements, therefore, can fall into one of two categories; biased or unbiased.

In an unbiased experiment, the scientifically interesting work would be in measuring specific material properties in various material-solution combinations. In the second type of experiment, the response of the system to applied biases would be the output of interest. For this reason, the materials used in the second type of experiment are limited to conductors and possibly some semiconductor materials.

It is likely, but yet unproven, that the effect of applied bias on the bulk potential of the solution is dominated by the geometry of the two electrodes used in a measurement. Therefore, I recommend for future studies the investigation of the effect of the relative size of electrodes on the bulk solution potential response to applied biases. This can be achieved by utilizing a sample design that greatly reduces the active electrode area from the 1 cm^2 used in the work above. For instance, one could devise a sample that is mostly composed of a material similar in nature to the probe, used for the calibration step, enclosing a smaller, active electrode. Figure 6.1(b) shows the design of such a sample. Note the relative sizes of the calibration area and the sample area. Figure 6.1(a) shows a similar sample design but for an unbiased experiment, where the calibration area needn't be as large and the material of interest dominates the overall area of the sample.

The range of applied biases in the studies I performed were limited to between 0 and +400 mV. The model I developed has no apparatus to account for bias polarity, but it is likely that specific ionic responses can have an effect on the measured forces. It would be of scientific interest, therefore to expand these measurements to applied biases of both larger magnitude and difference polarities. This can be done in concert

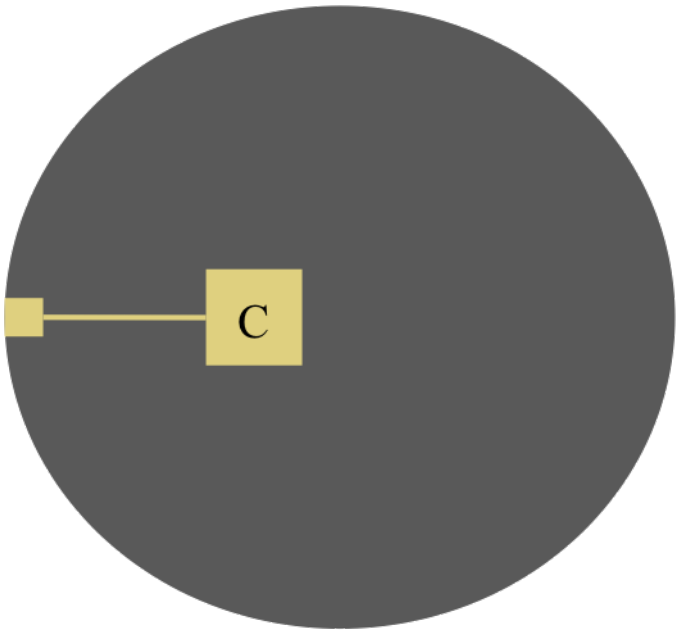

(a)

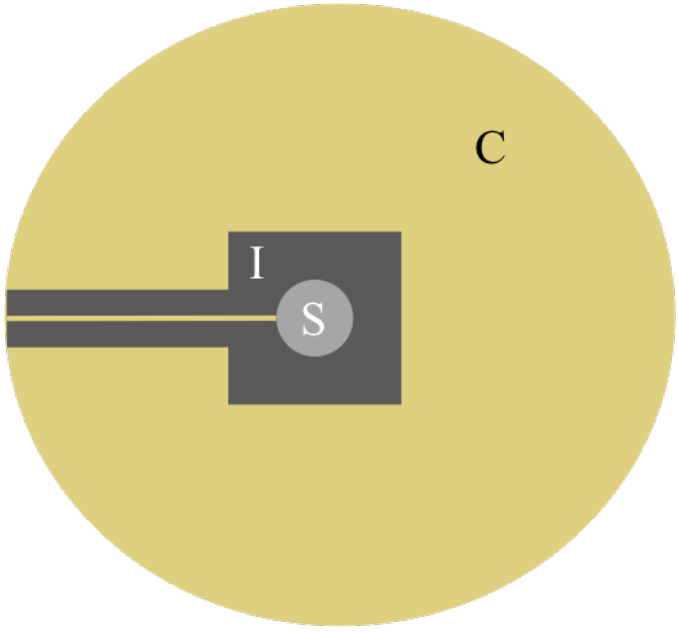

(b)

Figure 6.1: Sample design to be used in the (a) unbiased and (b) biased measurements. The part of the sample marked "C" is the same material as the probe and is used for calibration. The area marked "I" in the second design is an insulating layer and "S" represents the sample surface that will be external biased and subsequently measured.

with a wider selection of cation/anion pairs to examine the specific ionic effects that play a role in the double layer forces at various bias values.

Bibliography

[1] *Dictionary.com unabridged*, (2015).

[2] Frumkin A. and Gorodetzkaja A., *Kapillarelektrische erscheinungen an amalgamen*, Zeitschrift für Physikalische Chemie **136U** (1928), 451.

[3] Toyoko Arai and Masamichi Fujihira, *Effects of electric potentials on surface forces in electrolyte solutions*, Journal of Vacuum Science And Technology B: Microelectronics and Nanometer Structures Processing, Measurement, and Phenomena **14** (1996), no. 2, 1378–1382 1071–1023.

[4] Allen J. Bard, Fu-Ren F. Fan, Juhyoun Kwak, and Ovadia Lev, *Scanning electrochemical microscopy. introduction and principles*, Analytical Chemistry **61** (1989), no. 2, 132–138.

[5] Allen J. Bard and Larry R. Faulkner, *Electrochemical methods: Fundamentals and applications*, Wiley, 2001.

[6] D. Barten, J. M. Kleijn, J. Duval, H. P. v. Leeuwen, J. Lyklema, and M. A. Cohen Stuart, *Double layer of a gold electrode probed by afm force measurements*, Langmuir **19** (2003), no. 4, 1133–1139.

[7] John Bechhoefer, *Feedback for physicists: A tutorial essay on control*, Reviews of Modern Physics **77** (2005), no. 3, 783–836.

[8] Anne M. Becka and Cary J. Miller, *Electrochemistry at ω-hydroxy thiol coated electrodes. 4. comparison of the double layer at ω-hydroxy thiol and alkanethiol monolayer coated au electrodes*, The Journal of Physical Chemistry **97** (1993), no. 23, 6233–6239 0022–3654.

[9] J. O. Bockris, M. A. V Devanthan, and K. Mueller, *On the structure of charged interfaces*, Proc. Roy. Soc. **274** (1963), 55–79.

[10] Matthew A. Brown, Zareen Abbas, Armin Kleibert, Richard G. Green, Alok Goel, Sylvio May, and Todd M. Squires, *Determination of surface potential and*

electrical double-layer structure at the aqueous electrolyte-nanoparticle interface, Physical Review X **6** (2016), no. 1, 011007–.

[11] Hans-Jürgen Butt, *Measuring electrostatic, van der waals, and hydration forces in electrolyte solutions with an atomic force microscope*, Biophysical Journal **60** (1991), no. 6, 1438–1444.

[12] Hans-Jürgen Butt, Brunero Cappella, and Michael Kappl, *Force measurements with the atomic force microscope: Technique, interpretation and applications*, Surface science reports **59** (2005), no. 1, 1–152 0167–5729.

[13] Hans-Jurgen Butt and Michael Kappl, *Surface and interfacial forces*, Wiley-VCH, 2010.

[14] B. Capella and G. Dietler, *Force-distance curves by atomic force microscopy*, Surface Science Reports **34** (1999), 1–104.

[15] Michael D. Carolus, Steven L. Bernasek, and Jeffrey Schwartz, *Measuring the surface roughness of sputtered coatings by microgravimetry*, Langmuir **21** (2005), no. 9, 4236–4239.

[16] David L. Chapman, *A contribution to the theory of electrocapillarity*, Philosophical Magazine **6** (1913), 475–481.

[17] B. E. Conway, J. O'M. Bockris, and I. A. Ammar, *The dielectric constant of the solution in the diffuse and helmholtz double layers at a charged interface in aqueous solution*, Transactions of the Faraday Society **47** (1951), 756–766.

[18] B. Derjaguin and L. Landau, *Theory of stability of strongly charged lyophobic sols and of the adhesion of strongly charged particles in solutions of electrolytes*, Progress in Surface Science **43** (1941), 30–59.

[19] Jaroslaw Drelich, Jun Long, and Anthony Yeung, *Determining surface potential of the bitumen-water interface at nanoscale resolution using atomic force microscopy*, The Canadian Journal of Chemical Engineering **85** (2007), no. 5, 625–634.

[20] William A. Ducker, Tim J. Senden, and Richard M. Pashley, *Measurement of forces in liquids using a force microscope*, Langmuir **8** (1992), no. 7, 1831–1836.

[21] Jérôme Duval, Johannes Lyklema, J. Mieke Kleijn, and Herman P. van Leeuwen, *Amphifunctionally electrified interfaces: Coupling of electronic and ionic surface-charging processes*, Langmuir **17** (2001), no. 24, 7573–7581.

[22] Jonathan Ennis, Stjepan Marčelja, and Roland Kjellander, *Double layer mod-elingeffective surface charge for symmetric electrolytes in the primitive model double layer*, Electrochimica Acta **41** (1996), no. 14, 2115–2124.

[23] Maxim V. Fedorov and Alexei A. Kornyshev, *Towards understanding the structure and capacitance of electrical double layer in ionic liquids*, Electrochimica Acta **53** (2008), no. 23, 6835–6840.

[24] Jan Forsman, *A simple correlation-corrected poisson-boltzmann theory*, The Journal of Physical Chemistry B **108** (2004), no. 26, 9236–9245.

[25] Joëlle Fréchette and T. Kyle Vanderlick, *Double layer forces over large potential ranges as measured in an electrochemical surface forces apparatus*, Langmuir **17** (2001), no. 24, 7620–7627.

[26] Nir Gavish and Keith Promislow, *Dependence of the dielectric constant of electrolyte solutions on ionic concentration*, Physical Review E **94** (2012), 012611.

[27] Matthew A. Gebbie, Markus Valtiner, Xavier Banquy, Eric T. Fox, Wesley A. Henderson, and Jacob N. Israelachvili, *Ionic liquids behave as dilute electrolyte solutions*, Proceedings of the National Academy of Sciences **110** (2013), no. 24, 9674–9679.

[28] Brian Giera, Neil Henson, Edward M. Kober, M. Scott Shell, and Todd M. Squires, *Electric double-layer structure in primitive model electrolytes: Comparing molecular dynamics with local-density approximations*, Langmuir **31** (2015), no. 11, 3553–3562.

[29] Marcel Giesbers, J. Mieke Kleijn, and Martien A. Cohen Stuart, *The electrical double layer on gold probed by electrokinetic and surface force measurements*, Journal of Colloid and Interface Science **248** (2002), no. 1, 88–95.

[30] Louis George Gouy, *On the constitution of the electric charge on the surface of an electrolyte*, J. Phys. Theor. Appl. **9** (1910), no. 1, 457–468.

[31] David C. Grahame, *The electrical double layer and the theory of capillarity*, Chemical Reviews **41** (1947), 441–501.

[32] G. Gramse, A. Dols-Perez, M. A. Edwards, L. Fumagalli, and G. Gomila, *Nanoscale measurement of the dielectric constant of supported lipid bilayers in aqueous solutions with electrostatic force microscopy*, Biophysical Journal **104** (2013), 1257–1261.

[33] G. Gramse, M.A Edwards, L. Fumagalli, and G. Gomila, *Dynamic electrostatic force microscopy in liquid media*, Appl. Phys. Lett. **101** (2012), 213108.

[34] J. B. Hasted, D. M. Rittson, and C. H. Collie, *Dielectric properties of aqueous ionic solutions. parts i and ii*, J. Chem. Phys. **16** (1948), 1–21.

[35] Robert Hayes, Natalia Borisenko, Matthew K. Tam, Patrick C. Howlett, Frank Endres, and Rob Atkin, *Double layer structure of ionic liquids at the au (111) electrode interface: an atomic force microscopy investigation*, The Journal of Physical Chemistry C **115** (2011), no. 14, 6855–6863 1932–7447.

[36] William F. Heinz and Jan H. Hoh, *Relative surface charge density mapping with the atomic force microscope*, Biophysical Journal **76** (1999), no. 1, 528–538.

[37] Andrew C. Hillier, Sunghyun Kim, and Allen J. Bard, *Measurement of double-layer forces at the electrode/electrolyte interface using the atomic force microscope: Potential and anion dependent interactions*, The Journal of Physical Chemistry **100** (1996), no. 48, 18808–18817.

[38] Eric M. V. Hoek, Subir Bhattacharjee, and Menachem Elimelech, *Effect of membrane surface roughness on colloid-membrane dlvo interactions*, Langmuir **19** (2003), no. 11, 4836–4847.

[39] R. Hogg, T. W. Healy, and D. W. Fuerstenau, *Mutual coagulation of colloidal dispersions*, Trans. Faraday Soc. **66** (1965), 1638–1651.

[40] Kai Hu, Fu-Ren F. Fan, Allen J. Bard, and Andrew C. Hillier, *Direct measurement of diffuse double-layer forces at the semiconductor/electrolyte interface using an atomic force microscope*, The Journal of Physical Chemistry B **101** (1997), no. 41, 8298–8303.

[41] Takashi Ishino, Hiroyuki Hieda, Kuniyoshi Tanaka, and Nobuhiro Gemma, *Electrical double-layer forces measured with an atomic force microscope while electrochemically controlling surface potential of the cantilever*, Japanese Journal of Applied Physics **33** (1994), no. 11A, L1552.

[42] Jacob Israelachvili, *Salvation forces and liquid structure, as probed by direct force measurements*, Acc. Chem. Res **20** (1987), 415–421.

[43] Jacob N. Israelachvili and Gayle E. Adams, *Measurement of forces between two mica surfaces in aqueous electrolyte solutions in the range 0-100 nm*, J. Chem. Soc., Faraday Trans. 1 **74** (1978), 975–1001.

[44] Robert Jones, Hubert M. Pollock, Jamie A. S. Cleaver, and Christopher S. Hodges, *Adhesion forces between glass and silicon surfaces in air studied by afm: Effects of relative humidity, particle size, roughness, and surface treatment*, Langmuir **18** (2002), no. 21, 8045–8055.

[45] J. Keldenich and G. Peschel, *Stern potential near gold and chromium surfaces in contact with aqueous and alcoholic ammonium salt solutions*, Cooloid Polymer Sci. **269** (1991), 1064–1070.

[46] Mustafa Sabri Kilic, Martin Z. Bazant, and Armand Ajdari, *Steric effects in the dynamics of electrolytes at large applied voltages. i. double-layer charging*, Physical Review E **75** (2007), no. 2, 021502–.

[47] Lasse Hyldgaard Klausen, Thomas Fuhs, and Mingdong Dong, *Mapping surface charge density of lipid bilayers by quantitative surface conductivity microscopy*, Nature Communications **7** (2016), 12447.

[48] Bharat Kumar and Scott Crittenden, *Stern potential and debye length measurements in dilute ionic solutions with electrostatic force microscopy*, Nanotechnology **24** (2013), 435701.

[49] G. J. la O', B. Yildiz, S. McEuen, and Y. Shao-Horn, *Probing oxygen reduction reaction kinetics of sr-doped lamno3 supported on y2o3-stabilized zro2 : Eis of dense, thin-film microelectrodes*, Journal of the Electrochemical Society **154** (2007), no. 4, B427–B438.

[50] Stanislaw Lamperski, Monika Pluciennik, and Christopher W. Outhwaite, *The planar electric double layer capacitance for the solvent primitive model electrolyte*, Physical Chemistry Chemical Physics **17** (2015), no. 2, 928–932.

[51] E. D. Langlois, G. A. Shaw, J. A. Kramar, J. R. Pratt, and D. C. Hurley, *Spring constant calibration of atomic force microscopy cantilevers with a piezosensor transfer standard*, Review of Scientific Instruments **78** (2007), no. 9, 093705.

[52] Yuncheng Liang, N. Hilal, P. Langston, and V. Starov, *Interaction forces between colloidal particles in liquid: Theory and experiment*, Adv. Colloid and Interface Science **134-135** (2007), 151–166.

[53] Xue Yun Lin, Francois Creuzet, and Herve Arribart, *Atomic force microscopy for local characterization of surface acid-base properties*, The Journal of Physical Chemistry **97** (1993), no. 28, 7272–7276.

[54] F. Javier Montes Ruiz-Cabello, Gregor Trefalt, Plinio Maroni, and Michal Borkovec, *Electric double-layer potentials and surface regulation properties measured by colloidal-probe atomic force microscopy*, Physical Review E **90** (2014), no. 1, 012301–.

[55] A. N. Morozovska, E. A. Eliseev, and S. V. Kalinin, *Electromechanical probing of ionic currents in energy storage materials*, Applied Physics Letters **96** (2010), no. 22, 222906.

[56] Chiara Neto and Vincent S. J. Craig, *Colloid probe characterization: Radius and roughness determination*, Langmuir **17** (2001), no. 7, 2097–2099.

[57] Chiara Neto, Drew R Evans, Elmar Bonaccurso, Hans-Jürgen Butt, and Vincent S J Craig, *Boundary slip in newtonian liquids: a review of experimental studies*, Reports on Progress in Physics **68** (2005), no. 12, 2859.

[58] Hiroyuki Ohshima and Tamotsu Kondo, *On the electrophoretic mobility of biological cells*, Biophysical Chemistry **39** (1991), no. 2, 191–198.

[59] Alexander K. Opitz and Jürgen Fleig, *Investigation of o_2 reduction on pt/ysz by means of thin film microelectrodes: The geometry dependence of the electrode impedance*, Solid State Ionics **181** (2010), no. 15–16, 684 – 693.

[60] Hrishikesh V. Panchawagh, T. L. Sounart, and R. Mahajan, *A model for electrostatic actuation in conducting liquids*, J. Microelectromechanical Systems **18** (2009), 1105–1117.

[61] V. Adrian Parsegian and David Gingell, *On the electrostatic interaction across a salt solution between two bodies bearing unequal charges*, Biophysical Journal **12** (1972), no. 9, 1192–1204.

[62] W. Richard Bowen and Teodora A. Doneva, *Atomic force microscopy studies of membranes: Effect of surface roughness on double-layer interactions and particle adhesion*, Journal of Colloid and Interface Science **229** (2000), no. 2, 544–549.

[63] M. Sastre and J. A. Santaballa, *A note on the meaning of the electroneutrality condition for solutions*, J Chem. Educ. **66** (1989), 403.

[64] Peter J. Scales, Franz Grieser, Thomas W. Healy, Lee R. White, and Derek Y. C. Chan, *Electrokinetics of the silica-solution interface: a flat plate streaming potential study*, Langmuir **8** (1992), no. 3, 965–974.

[65] V. Švorčík, P. Slepička, J. Švorčíková, M. Špírková, J. Zehentner, and V. Hnatowicz, *Characterization of evaporated and sputtered thin au layers on poly(ethylene terephtalate)*, Journal of Applied Polymer Science **99** (2006), no. 4, 1698–1704.

[66] D. Tabor and R. H. S. Winterton, *Surface forces: Direct measurement of normal and retarded van der waals forces*, Nature **219** (1968), no. 5159, 1120–1121.

[67] Emmanuel Trizac, Lydéric Bocquet, and Miguel Aubouy, *Simple approach for charge renormalization in highly charged macroions*, Physical Review Letters **89** (2002), no. 24, 248301.

[68] Ken-Ichi Umeda, Noriyaki Oyabu, Kei Kobayashi, Yoshiki Hirata, Kazumi Matsushige, and Hirofumi Yamada, *High-resolution frequency-modulated atomic force microscopy in liquids using electrostatic excitation method*, Appl. Phys. Expr. **3** (2010), 065205.

[69] E. J. W. Verwey and J. T. G. Overbeek, *Theory of the stability of lyophobic colloids*, Elsevier Publishing Company, Inc., 1948.

[70] Herman von Helmholtz, *Some laws concerning the distribution of electric currents in volume conductors with applications to experiments on animal electricity*, Annalen der Physik und Chemie **165** (1853), no. 6, 211–233.

[71] Peiming Wang and Andrzej Anderko, *Computation of dielectric constants of solvent mixtures and electrolyte solutions*, Liquid Phase Equilibria **186** (2001), 103–122.

[72] Gunther Wittstock, Malte Burchardt, Sascha E. Pust, Yan Shen, and Chuan Zhao, *Scanning electrochemical microscopy for direct imaging of reaction rates*, Angewandte Chemie International Edition **46** (2007), no. 10, 1584–1617.

[73] Cunlu Zhao, Daniel Ebeling, Igor Siretanu, Dirk van den Ende, and Frieder Mugele, *Extracting local surface charges and charge regulation behavior from atomic force microscopy measurements at heterogeneous solid-electrolyte interfaces*, Nanoscale **7** (2015), 16298–16311.

Glossary of Terms

Amplitude Modulation Atomic Force Microscopy	Operational mode of Atomic Force Microscopy in which the cantilever is oscillated and its amplitude is kept constant via a feedback loop.
Atomic Force Microscopy	Surface analysis technique capable of atomic-level resolution that utilizes a mechanical cantilever with an attached probe that is scanned over the surface being measured.
Counter Electrode	Part of a typical three-electrode electrochemical measurement through which a current is expected to flow.
Cyclic Voltammetry	Electrochemical measurement in which a potential is applied to a working electrode and the current through that electrode is measured.
Debye Length	The distance from a surface immersed in a liquid at which the electrostatic potential drops by a factor of e.
Differential Capacitance	The voltage dependent capacitance of a system such as the electrostatic double layer.

Diffuse Layer aka Gouy-Chapman Layer	Part of the electrostatic double layer in which ions are more heavily impacted by thermal motion and thus move more freely in space.
DLVO Theory	Named for Derjaguin, Landau, Verwey, and Overbeek. Theory used to describe the forces between objects in liquid media.
Electrochemical Surface Force Apparatus	Modified version of the Surface Force Apparatus that allows for the electrochemical characterization of surfaces.
Electrostatic Double Layer	Structure of ions that is present at the interface of a solid and liquid.
Electrostatic Force Microscopy	Operational mode of Atomic Force Microscopy in which electrostatic interactions between the probe and sample are measured.
Frequency Modulation Atomic Force Microscopy	Operational mode of Atomic Force Microscopy in which the cantilever is oscillated and its frequency of oscillation is kept constant via a feedback loop.
Gouy-Chapman Layer	See "Diffuse Layer".
Gouy-Chapman Model	Model of the electrostatic double layer in which its structure is that of a single diffuse layer.

Inner Helmholtz Plane	The plane parallel to the solid surface that runs through the centers of adsorbed solvent molecules.
Kelvin Force Microscopy	Operational mode of Atomic Force Microscopy in which the potential difference between the probe and sample can be measured.
Lock-In Amplifier	A device used to measure the characteristics of an input signal by comparing to an internal reference signal.
Outer Helmholtz Plane	The plane parallel to the solid surface that runs through the centers of nearest solvated ions.
Potential of Zero Charge	The potential applied to an electrode at which no charge accumulates at the interface of that electrode and the solution in which it is immersed.
Potential of Zero Force	The potential applied to either the sample or probe in a force measurement experiment that causes the force to go to zero.
Proportional Integral Derivative	A feedback control paradigm in which the error or difference between a set point variable and a process variable and applies a correction based on the proportion, integral, and derivative of that error signal.

Reference Electrode	Part of a typical three-electrode electrochemical measurement which is used as a point of constant potential against which applied biases are measured.
Stern Layer	Part of the electrostatic double layer which encompasses the sheet of rigidly bound ions.
Stern Model aka Gouy-Chapman-Stern Model	Model of the electrostatic double layer in which its structure is that of a rigidly bound layer of ions directly adjacent to a diffuse layer of ions.
Surface Force Apparatus	Surface analysis device used to measure the forces between two surfaces as a function of their separation.
Surface Potential	Ambiguously defined term most often used to represent the potential drop through the diffuse layer of an electrostatic double layer.
Working Electrode	Part of a typical three-electrode electrochemical measurement to which an external bias is applied.